SiC Powder as Source for Single Photon Emission in Quantum Technologies

Anna Stray Rongve

Thesis submitted for the degree of
Master of Science in Material Science and Nanotechnology
60 credits

Department of Chemistry

Faculty of mathematics and natural sciences

University of Oslo

Spring 2022

SiC Powder as Source for Single Photon Emission in Quantum Technologies
http://www.duo.uio.no/
Trykk: Reprosentralen, Universitetet i Oslo

Abstract

Silicon carbide (SiC) is a wide bandgap semiconductor that has become a mature material for power electronic applications, and has recently gained considerable interest as host material for point defects useful in quantum technology. In this thesis, we study the defect emission SiC powder that has been irradiated and annealed to form quantum compatible point defects. Of particular interest are defects that may act as single-photon emitters. The SiC powder includes the 4H, 6H, 3C and 15R polytypes, but a particular emphasis has been put on 6H-SiC, as it was the most abundant polytype in the powder. The emission centres in both ensemble and individual particles have been observed by optical characterization using photo- and cathodoluminescence. While photoluminescence (PL) provides insight into emission from the powder, the resolution of cathodoluminescence (CL) allows for mapping the emission from single particles. Indeed, PL displays a considerable amount of sharp emission lines, as expected from single-photon emitters, and luminescence from both identified and unidentified emission centres was observed. CL revealed a non-uniform emission, both within and between particles.

To support the understanding of the defect emission, numerical simulations based on the Finite Difference Time Domain solver Lumerical were performed. Based on the results from cathodoluminescence spectroscopy and the simulations it seems like the geometry of the SiC particles is to a large extent determining the emission, and not necessarily the defect positioning within the particles. Furthermore, the pyramidal/triangular particles, as opposed to the spherical, cubic, and other geometries, seems to a large extent focus the emission in a specific direction, which can be very useful in quantum repeaters used in lines of quantum communication.

Sammendrag

Silisiumkarbid (SiC), en bredbåndet halvleder, er et etablert materiale innen kraftelektronikk. Nylig er det oppdaget at punktdefekter i SiC kan være nyttig i kvanteteknologi. I denne oppgaven studeres emisjon fra defekter i silisiumkarbidpulver som har blitt bestrålt og varmebehandlet for å danne kvantekompatible punktdefekter. Spesielt er det en interesse for defekter som emitterer enkelfotoner, såkalte 'single-photon emitters'. SiC-pulveret inneholder polytypene 4H, 6H, 3C og 15R, der 6H-SiC er dominerende, og har derfor fått størst fokus. Emisjonssentre i både pulveret som helhet og individuelle partikler er observert med optisk karakterisering med foto- og katodeluminescens. Mens fotoluminescens gir et godt bilde på emisjonen fra pulveret, gjør oppløsningen i katodeluminescens det mulig å kartlegge emisjon fra enkeltpartikler. Faktisk viser fotoluminescens en betydelig mengde skarpe emisjonslinjer, noe som er forventet fra single-photon emitters, og linjer fra både identifiserte og uidentifiserte emisjonssentre ble observert. Katodeluminescens gav inntrykk av en ujevn emisjon både innad i enkeltpartikler og mellom flere partikler.

For å øke forståelsen av defektemisjonen, ble det gjort numeriske beregninger basert på ≪Finite-Difference Time Domain≫ algoritmen, implementert i Lumerical. Basert på resultatene fra katodeluminescensspektroskopi og simuleringene kan det se ut til at geometrien på partiklene i stor grad påvirker emisjonen, og ikke nødvendigvis fordelingen av defekter innad i partiklene. Videre kan det se ut som at pyramideformede partikler, i motsetning til kubiske, sfæriske eller andre geometrier, i større grad fokuserer emisjonen i spesifikke retninger, noe som kan være veldig nyttig i kvanterepeatere brukt i kvantekommunikasjon.

Acknowledgements

First, I want to thank my supervisors, Lasse Vines, Snorre Braathen Kjeldby, Vilde Mari Reinertsen, and Augustinas Galeckas for pointing me in the right direction. Thank you all for letting me ask the stupid questions and for letting me in on your knowledge. I also want to direct a thank you to Marianne Etzelmüller Bathen for her incredible insight into the field of semiconductors and quantum technology. Thank you all for the time you have spent teaching me how to operate instruments, helping me analyze my results and for proofreading my thesis. Thank you the lab-engineers Viktor Bobal for implanting my samples and to Halvor Dolva for your time filling the nitrogen tank at the lab so many times.

I also want to say thank you to my fellow students in the MENA class of 2017 for these past five amazing years. A special thanks go to my partners in crime, Benedicte, Mariel and Magnus for all the fun and frustrating times we have shared.

Without the encouragement and support from my family, a degree and thesis would probably not have happened. Thank you, Ingrid, for being so inspirational with all your knowledge and hard-working skills. And, Lars, thank you for your tremendous support, for pushing me and for believing in me.

Contents

Chapter 1

Introduction to Quantum Technology

A *second quantum revolution* is currently arising. The *first quantum revolution* started a century ago and is noticeable in everyday devices. Transistors, lasers, and the atomic clock promote computers, optical fibre communication and the global positioning system (GPS). Traditional transistor-based devices have for many years achieved increased computational speed with a decrease in component sizes and an increase in the number of chips per device. As predicted by Moore [1], the amount of transistors in integrated circuits has doubled every two years. Technological enhancement through competition drove the transistor size down to 2 nm in 2021 [2].

At a billionth of a meter exists is another world from as we know it. Quantum mechanics have thought us that an object can be at several locations simultaneously and that observing the objects changes them. To predict where things are at a specific time is uncertain, only the *probability* of the states in a system is known.

The world of quantum physics describes the ultrasmall, single particles and photons invisible to the human eye. The second quantum revolution utilizes the phenomena occurring in the nanoscale range. Continuing the development of both hardware and software in the field of quantum technology has the potential of a revolution with the same degree of influence as the first quantum revolution. For example, practical large scale quantum computers can efficiently contribute to enhance the fields of physics and chemistry through numerical calculations of materials, designing new drugs, weather forecasts and solving optimization problems.

Quantum technology (QT) applies the phenomena from quantum physics to practical applications and devices. Algorithms run faster by analyzing many bits, or qubits, at a time, so-called quantum computing. Eavesdroppers leave traces in our transmitted data just by observing it, a phenomenon utilized in quantum cryptography and communication. While sensing beyond the present-day resolution may be available through quantum sensing.

To date, six important quantum principles, which are utilized in QT, have been identified.

- The Heisenberg *uncertainty principle*, $\Delta x \Delta p > \hbar/2$, states that we cannot anticipate a particle's position and momentum simultaneously. Instead, the probability of a particle being in a particular state must be calculated.

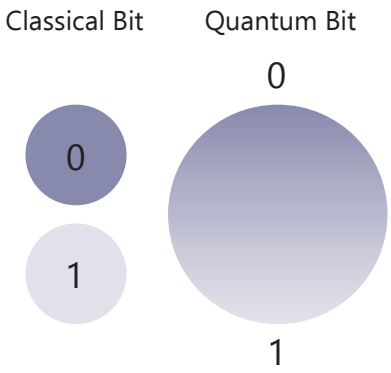

Figure 1.1: Conceptual illustration of a quantum bit (qubit), that can inhibits any superposition of the states 1 and 0, compared to a bit used in classical computations with states ON (1) and OFF (0).

- In quantum systems, energy states are constrained to discrete sets of *quantized energy states* instead of continuous energy bands.

- If quantum states are waves, each state may be described as a sum, a *superposition*, of two or more distinct states. The act of measuring the superposition of two quantum states drives the system into one of the two states, thus destroying the object's quantum nature. For example, the polarization directions of a photon can be superpositions of horizontal (H) and vertical (V) directions. Measuring forces its polarization direction randomly into either H or V.

- Extending the principle of superposition to a pair or collection of particles is called *entanglement*. The particles are then constructed such that each particle's quantum state cannot be characterized independently of the state of the other particle. You may infer the state of the other entangled particle by measuring the state of the other. For example the superposition of two photons (1 and 2) can either be a combination of fully horizontally (H_1H_2) and fully vertically (V_1V_2) polarization or a anti-correlated combination with the particles in different polarizations (H_1V_2 and V_1H_2).

- The wavefunction of a particle can propagate through a potential barrier, and hence the particle can be in a classically forbidden state.

- Quantum *coherence* and *decoherence* are related to superposition and entanglement. The phenomenon is a result of the wave-like features of quantum states. When two waves interact coherently, a superposition of states with a phase connection forms. Decoherence is the result of a loss of coherence. In order to perform quantum computation operations, coherence must be maintained. Long coherence times, the time before the quantum features of qubit leak into the environment, necessitate isolating the system from its surroundings to avoid decoherence. On the other hand, a completely isolated system cannot be manipulated.

Where the logic of a classical transistor-based computer is either ON (1) or OFF (0) (bit), the logic behind the quantum computer is realised on the principles of quantum bits (qubits). The qubit can be ON or OFF, or ON and OFF simultaneously (superposition). An illustration of the two can be seen in Figure 1.1. Several qubit hosts are being explored, including but not limited to photons, individual atoms, nuclei or quantum dots, solid superconducting or semiconducting materials and the spin or charge state of electrons [3].

1.1 Quantum Computation

A quantum computer (QC) is a qubit based device utilizing quantum physics to solve specific classes of problems [3]. A many-fold computational speed-up is expected because of the principle of superposition of each qubit, yielding several more degrees of freedom than simply 1 or 0, and multi-qubit entanglement. Such devices can compute large amounts of data in parallel.

QCs are expected to outperform classical computers in factoring large numbers - relevant in cryptography - and when searching through large amounts of data. However, the maybe most important advantage of the speed-up is expected to be solving problems involving many variables such as governing traffic, predicting weather and the finance market. In addition, QCs should be able to solve complex quantum chemistry problems and accurately simulate many-body quantum systems.

The technology faces several limitations and challenges. Examples are controlling a complex many-qubit system. Quantum states cause decoherence and other quantum noise, which prevent error-free quantum state manipulation. Therefore, several scientists, including DeVencenzo [4] and Ladd *et al* [5] have proposed a set of "rules" for which defines a operational logic-based quantum computer. The system should

1. be scalable
2. have entangleable quibits
3. have a simple initial system to initialize qubit states
4. have coherence times greater than the gate operation time
5. have a set of universal quantum gates
6. have a system which reads the quibit states reliably, for example through photon emission

There are several operational quantum computers available in laboratories and even in the open market. A majority of them are based on superconducting materials. IBM has a 127 qubit computer and is about to release another with 433 qubits in 2022 [6]. Moreover, Google's quantum computer of 53 qubits solved a problem in 2.5 days which would have taken 10,000 years on the best classical supercomputers computer available indicating that quantum supremacy is within reach.

1.2 Quantum Sensing

Sensors are vital and everywhere. Phones, cameras, cars, navigation, chemical and material analysis and characterization rely heavily on sensors. Moreover, precise measurements are crucial for science and commerce for exchanging information, goods and services [7]. By utilizing quantum technology, the resolution of sensors may drastically increase.

Quantum sensors are sensors exploiting quantum properties to detect quantum and classical disturbances. This technology is possible because of the environmental sensitivity of superposition. An operational quantum sensor meets the criteria of 1) discrete and resolvable energy levels, 2) a simple initial system to initialize qubit states which can be identified and coherently manipulated by time-dependent fields, and 3) interaction with physical properties through a coupling parameter [8]. Through quantum entanglement, the precision of the sensors increases and scales as the number

of particles, N, known as the Heisenberg limit. Comparatively, classical sensors are limited by the $\sqrt{N}$.

Quantum sensing is yet the most developed of the mentioned technologies herein. Quantum sensors, such as single electrons, defects, charges or magnets, can measure changes in temperature and electrical fields in close proximity. Navigation from A to B in our everyday life relies on the timing of the atomic clock in satellites. The clock measures time by analyzing the frequency of radiation from atoms. The NV centre in diamond can detect small changes in magnetic fields [9]. Quantum sensors have the potential in improving everyday devices, such as mobiles, medical diagnostics and imaging, enabling high precision navigation. Quantum metrology can give a new standard of time-keeping or electrical measurements with quantum sensors.

1.3 Quantum Communication

The constant threat of cyber attacks on governments, military, businesses and private persons is a concern. There is often news about a new hack exposing sensitive information, such as medical records and credit card information. Encryption protocols protect sensitive data transferred between two counterparts. One of the standard protocols for encryption is the Public Key Distribution (PKD). Traditional PKD uses trapdoor functions which are mathematical functions easily solved in one direction and computationally heavy in the other [10, 11]. To decrypt the message, a separate private key, made by the same trapdoor functions, is sent. As the data and keys are classical bits, 0s and 1s, hackers can easily copy the bits while in transit without leaving any trace. Using a QC, the encryption is even more vulnerable. This motivates the development of a communication system immune to eavesdropping.

Quantum communication is the transmission of entangled quantum states across a long distance, imaginable as flying qubits. Photons, solitary or entangled, are the most common implementation of such qubits. The qubits can be transferred through optical fibres which already are a part of our infrastructure. Its security surpasses the conventional communication with classical bits as the signal cannot be copied without leaving a trace and because the keys unlocking the decryption are in theory only available to those involved in the line of communication. The quantum keys are similar to the classical, consisting of a sequence of random numbers. However, the quantum key is generated remotely through the exchange of photons. Therefore anyone trying to steal the key will leave a trace, giving the receiver or sender time to take action. The same technology has the potential to be used in long-term secure storage, cloud computing, cryptography-related tasks, and in the future, a quantum internet [7].

To date, quantum communication is limited by distances less than 500 km because of the absorption of photons in the optical fibre. A quantum signal cannot pass through conventional repeaters because the signal cannot be copied ('no cloning'). The repeaters can store quantum states, making it possible to break up the transmission distance where loss is insignificant. Quantum repeaters are complex systems, but they are commonly based on trusted nodes, computers connecting the network of QCs or quantum technology, which should fulfil the requirements of preserving entanglement. The nodes decrypt the data into bits before re-encrypting it into qubits again, which essentially makes the node not trustworthy as data can be read out from the node after decryption. Quantum repeaters fully based on quantum technology would be ideal. A quantum communication system based on such nodes is operational between Beijing and Shanghai.

1.4 Quantum Platforms

This section gives an overview of the current status of physically implemented quantum platforms. Several quantum platforms have great potential. However, the need for further development to ensure a scalable and reliable technology is still present and probably will be for years to come.

The **Josephson junctions** is the most used platform for quantum computing and consists of superconducting circuits. The qubits are enabled through Cooper pairs of electrons, which can be controlled electrically without losing quantum coherence. The same is not possible with non-superconducting qubits. The main disadvantage is the operational temperature, often in the mK temperature range, resulting in high operating costs. Short coherence times are also a challenge, making the technology hard to scale [7]. Alternatively, the polarization state of **single photons** can be used for photon-based quantum computing and internal energy levels of an **isolated atom or ion** can be used as qubits, but are difficult to scale. **Quantum dots** (QD) are artificial atoms in semiconductors where their optical and electrical properties can be defined by discrete energy levels. **Point defects** can also have discrete energy levels that can be utilized as a QT platform, and they potentially have the advantage of having coherent spin states susceptible to external manipulation. Using point defects in semiconductors for quantum technology is the motivation for the work presented in this thesis.

Point defects in semiconductors with quantum friendly properties are currently being researched extensively. To date, the nitrogen vacancy (NV) centre in diamond is by far the most studied platform. The centre has a wide range of potential applications in QT, for example, as a sensor detecting the magnetic moment of a single molecule, and is a single photon emitter at room temperature [12]. The silicon vacancy in silicon carbide, a wide bandgap semiconductor, is another defect which has been studied widely, both experimentally and theoretically. However, SiC offers many more defects and colour centres and is likely more scaleable compared to diamond, which should be looked into for further development in the field of quantum technology.

Most studies using SiC as a platform for quantum defects are based on wafers, but it is also possible to use different approaches, such as nanostructures and micron-sized particles (powder). Hence, we here try to identify qubit candidates, desirably in the telecom area, in 6H-SiC in powder form as building blocks for quantum technology and the use of single grains as single-photon sources for quantum communication.

Cathodoluminescence and photoluminescence spectroscopy, two complementary methods, were used to optically characterize the material. To further understand the emission from the SiC grains, numerical simulations of electromagnetic fields through the Finite-Difference Time-Domain (FDTD) method, were used.

Chapter 2 introduces the central theory and background for understanding the material and experimental methods in this work. In Chapter 3, an introduction of the experimental methods is given. The results are presented and discussed in Chapter 4 and concluded in Chapter 5. Lastly, a suggestion for further work is given.

Chapter 2

Theoretical Background

In this chapter important theory for understanding, SiC as a semiconductor and its use within quantum technology is presented. First, a description of the atomic structure of materials, and semiconductors and their electrical band structure is given as a basis for understanding colour centre emission. Thereafter the material in question, SiC, and its many polytypes are presented together with its potential defects meeting the requirements of quantum technology applications. The last section describes the physics behind the Finite-Difference Time-Domain method used to simulate the electromagnetic environment of SiC particles.

2.1 Atomic Structure of Materials

Extensive mathematical models describe the structure and properties of materials. Here we provide an overview considered necessary for the understanding of semiconductor physics in the following section.

Materials are categorized as covalent, metallic or ionic by the nature of their interatomic bonds. The ordering of close-packed atoms in a material is either crystalline or amorphous. Crystalline materials have a long-range periodicity of the atomic stacking throughout the structure. Breaking the periodicity into smaller domains with periodicity defines polycrystalline materials. An amorphous solid lacks the long-range ordering of atoms but can have a local atomic order.

Silicon Carbide is a crystalline material where groups of silicon and carbon atoms, *the basis* of the crystal, are arranged periodically. Repeating the basis of the structure in three dimensions makes up the crystal. This dimensional ordering, called the lattice of the crystal, can be described mathematically by the three lattice vectors, $\mathbf{a}_1$, $\mathbf{a}_2$ and $\mathbf{a}_3$. The translation vector $\mathbf{R}$, describes all lattice points in the crystal and is given by

$$\mathbf{R} = x\mathbf{a}_1 + y\mathbf{a}_2 + z\mathbf{a}_3 \tag{2.1}$$

where x, y, z are integers. The span of the lattice vectors, called the primitive cell, is the smallest unit required to span the whole crystal by repetition while preserving the symmetry of the lattice. A primitive cell with one lattice point is called the primitive unit cell. The unit cell and the length of the lattice vectors are often used to describe the structure of crystalline materials. How atoms

are arranged into close-packed crystals is determined by the bonding forces (the equilibrium of repulsive and attractive forces) and the size of the involved atoms. Silicon carbide, for example, has a hexagonal structure, but other phases of SiC, such as the cubic and rhombohedral, exists. The crystal structure of SiC is elaborated in section 2.3.1.

2.2 Semiconductor Physics

Semiconductors are materials bridging the electrical conductivity gap between metals and insulators. Devices based on semiconducting materials are electronically active, as opposed to wires or insulators. To understand how such materials fulfil the requirements and the principles of quantum technology devices, an introduction to semiconducting materials is given herein.

2.2.1 Electronic Band Structure

The energy states available to electrons of isolated atoms are discrete. By Pauli's repulsion principle, each state can be occupied with one electron. When two atoms are brought close to each other, the energy of their respective state is split and slightly shifted. Decreasing the distance between the atoms increases the splitting.

Supplying more atoms of the same kind at increased distances causes further splitting of the energy levels. Eventually, the discrete levels transform into a set of quasi-continuous energy bands as Heisenberg's uncertainty principle no longer permits a distinction between individual levels. The continuous bands are considered as *allowed* energies for which electrons can occupy. The energy gap between the allowed bands referred to as the bandgap is *forbidden* for electrons to occupy. The bands and bandgap construct the electronic band structure of semiconducting materials. Variations in band structure vary with the elements in a material and the crystal structure.

The valence band (VB) refers to the highest energy band occupied by electrons at 0 K. While the conduction band (CB) is the lowest vacant band (CB) under the same conditions. The prohibited energy range between the conduction- and valence band is the bandgap. Conductivity in semiconductors can, for example, be achieved when electrons are given energy equivalent to or larger than the semiconductors' bandgap energy or by introducing dopants as described in Section 2.2.2. This mechanism leaves electronic states in the bands. A empty, positive, conducting *hole* in the valence band and negative, conducting *electron* in the conduction band. Pairs of electrons and holes are referred to as electron-hole pairs (EHPs)

The bandgap of semiconductors is different from that of insulators, as seen in Figure 2.1. At 0 K the band structure of the two material types is similar, with a filled valence band and empty conduction band. However, optical and thermal excitation of electrons across the bandgap is only considered probable for semiconductors, not insulators, at a reasonable temperature or incident photon energy. Note that wider bandgap materials could be considered semiconductors if the presence of energy levels within the bandgap bridges the valence and conduction band. Because of partly filled or overlapping bands in metals they conduct electrons without exciting electrons across the bandgap.

Bandgaps can be either considered direct or indirect. In a direct bandgap semiconductor, the VB

maximum and the CB minimum are associated with the same wave vector, k. While in an indirect bandgap the values of k are different in the VB maximum and the CB minimum. Resulting in a lower probability to excite electrons from the VB to the CB as more energy and a change in momentum are needed to make the transition. To change the momentum of an electron, an incident phonon is required. Silicon carbide is an indirect bandgap semiconductor.

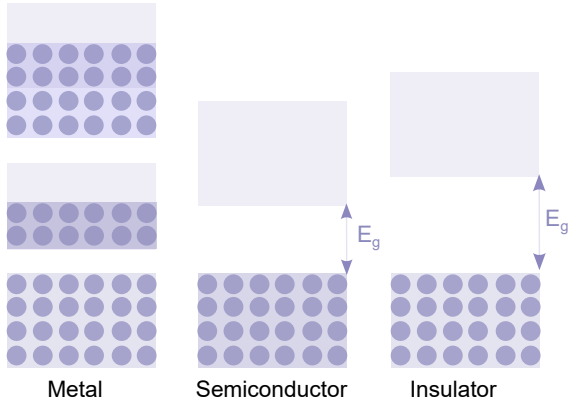

Figure 2.1: Illustration of a simplified two-dimensional band diagram for metals, semiconductors and metals. The blue circles mimic states occupied by electrons. The metal bands can partly overlap(top) and be partly filled (middle). The figure is adapted from Streetman [13].

The Fermi-Dirac distribution describes the likelihood of an electron populating a state at a given temperature, and is as follows

$$f(E) = \frac{1}{\exp(\frac{E-E_F}{k_B T}) + 1}, \tag{2.2}$$

where k_B is Boltzmann constant, T the temperature, E the energy and E_F the Fermi level or chemical potential of the electrons. All energy levels above E_F are empty at $T = 0$ K, whilst those below are occupied by electrons. If $|E - E_F| << k_B T$, $f(E)$ can be approximated by the Boltzmann distribution.

$$f(E) \sim (\frac{E - E_F}{k_B T}). \tag{2.3}$$

The Fermi-level (E_F) is an important quantity when analysing behaviour of semiconductors and is defined as when the probability of an electron occupying an energy state at the E_F is equal to $\frac{1}{2}$ [13]. At 0 K, shown in Figure 2.2a, all energy states $E < E_F$ are occupied with electrons while energy states $E > E_F$ are empty (filled with holes). The probability of a hole occupying a state is 1-$f(E)$.

Increasing the temperature, the probability of an electron occupying a state above the Fermi-level (E_F) increases, illustrated in Figure 2.2b and 2.2c. Consequently, the electronic conduction increases with the increasing concentration of mobile electrons in the CB and wholes in the VB. The concentrations of electrons and holes in a semiconductor can be calculated from the Fermi distribution if the densities of available states in the VB and CB are known. The equilibrium concentration of electrons in the CB is given by

$$n_0 = \int_{E_c}^{\infty} f(E)N(E)dE \tag{2.4}$$

where N(E) is the density of states (DOS) (cm^{-3}) in the energy range dE. The density of states is proportional to the energy of electrons, $E^{\frac{1}{2}}$ [13].

When the E_F is positioned close to the middle of the bandgap is the definition of an *intrinsic* semiconductor. The opposite of an intrinsic semiconductor is *extrinsic* semiconductors. Introducing a foreign atom, for example, nitrogen in SiC, into the structure, is often referred to as *doping*, and causes the Fermi level to decrease or increase depending on the nature of the foreign atom. If the energy level is close to the CB edge, the Fermi level shifts upwards and it shifts downwards if the energy level is closer to the VB edge.

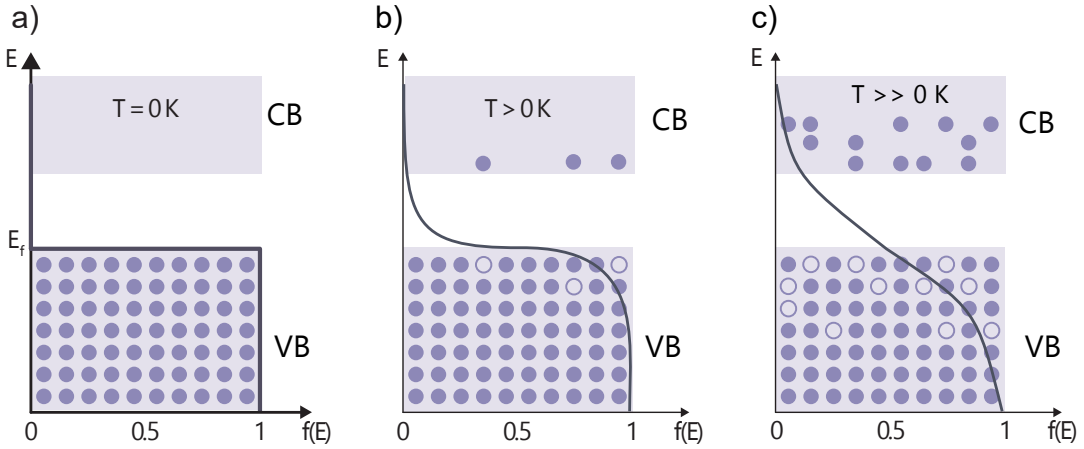

Figure 2.2: Fermi Dirac distribution at a) T = 0 K, b) T > 0 K , c) T >> 0 K. Circled dots represents electrons and empty circles are holes.

2.2.2 Semiconductor Defects

By the principles of thermodynamics, perfect crystals do not exist above 0 K. Hence, intrinsic point defects are always present. An intrinsic defect in a semiconductor is an imperfection in the otherwise perfect crystal lattice. These defects can be single, for example, a missing atom (vacancy) or an atom in the wrong position (substitutional), or cluster together in pairs or groups. Extrinsic defects are the presence of foreign atoms (intentional dopants or unwanted impurities) in the material. Unless the dopant fits into the empty voids (*interstitial*) in the crystal, they rely on the presence of intrinsic defects to fit in the crystal structure to *substitute* a host atom. Extrinsic and intrinsic defects can also combine and form complexes. Intrinsic and extrinsic defects have a profound effect on the electrical and optical properties of the material to the extent where the concentration of dopants becomes too high and eventually limits electron mobility. An illustration of such defects is shown in Figure 2.3.

In this work, we are interested in zero-dimensional point defects. Their properties, such as spin, polarization and single-photon emission have the potential in quantum technology, for example as qubits. Higher-dimensional defects include, but are not limited to, one-dimensional line defects or dislocations, two-dimensional grain boundaries and three-dimensional volume precipitates. The

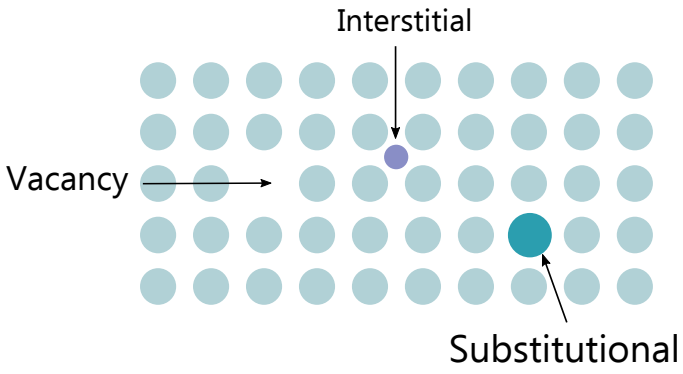

Figure 2.3: Illustration of the vacancy, interstitial and substitutional defects in a crystal lattice. Interstitial defects can either be foreign atoms or a host atom ('self-interstitial')

higher dimensional defects are present in SiC but are not considered in the remaining of this work.

Point defects can introduce discrete energy levels within the bandgap. The position of these energy levels highly influences the electrical and optical properties of the material. We typically distinguish between *shallow* and *deep level* point defects.

Shallow defects introduce energy states close to a band edge (CB or VB within ~ 0.2 eV). The wavefunctions describing the electrons in these defects are highly delocalized around the defect position in the lattice. Therefore, shallow defects are likely ionized thermally. Defects in a positive charge state after ionization are classified as *donors*, while those in a negative charge state as a result of accepting an electron, are referred to as *acceptors*. Such defects are often intentionally introduced and referred to as dopants.

Deep level defects, usually originating from impurities and dangling bonds, are often referred to as defect levels and are typically positioned deeper (read: closer to the middle) in the bandgap. However, these states can also exist closer to the band edges as their electrons are more strongly bound, and the wavefunctions of the electrons are localized at the defect. Hence, the defect is not easily ionized thermally. For this reason, the electrons in these states contribute little to conduction in the material.

Defect Related Luminescence

In quantum technology, we can take advantage of the localized nature of the deep level centres to ensure isolation and coherence. For that reason, deep level defects within SiC will be the focus of this work. When the deep level defect interacts with electrons and holes, it can potentially have a great influence on the electro-optical properties of semiconductors. The levels can act as 'recombination centres', 'traps' or 'generation centres' for the charge carriers which may modify the concentration of conducting electrons (or holes) in semiconductors and devices fabricated thereon. Defect levels within the bandgap are often termed *charge-state transitions* as they signify the transition between charge states q and q $\pm$ 1. The charge state of the defect is dependent on the position of the Fermi level [14] and one defect can have charge state transitions.

The optical transitions of interest in QT do not involve quasi-particles (electrons/holes) moving

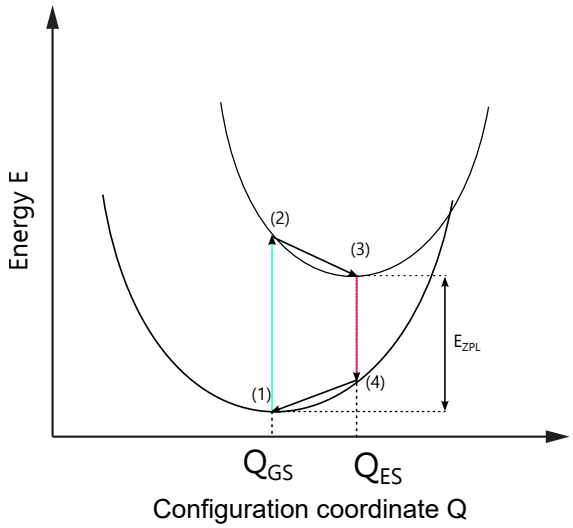

Figure 2.4: Simplified configurational model illustrating the transitions leading to emission. Adapted from [14].

freely within the lattice, as is the case with radiative recombination of electron-hole pairs from e.g., defect states to the valence band. The Frank-Candon principle through a configurational coordinate model describes the transitions of interest where the energy of the system is dependent on the displacement of the nuclei (atoms) next to defects, illustrated in Figure 2.4 [14]. Removing an atom from the lattice creates a defect and the surrounding matrix changes and reaches a new equilibrium where the interatomic distance decreases from that of the lattice constant. The configurational coordinate, Q_{GS}, describes this new equilibrium state in three dimensions. For technical simplifications, the three-dimensional rearranging of atoms described by Q_{GS} is reduced to one dimension.

In position (1) close to the bottom of the lower energy parabola in Figure 2.4, the system is in its ground state. Within 10^{-15} s a photon of energy equal to the energy difference between (1) and (2) is captured, which brings the system into an excited state, illustrated by the higher energy parabola. As the phonon frequencies in the lattice are orders of magnitude slower ($10^{-12} - 10^{-13}\,s^{-1}$) than the photon capture time, the transition is vertical in the figure. The atoms in the solid have not adapted their positions to the new state and the system is therefore in a non-equilibrium excited vibrational state. When the atoms close to the defect rearrange their positions they reach a new equilibrium configuration Q_{ES} given by position (3) in the excited state. The energy difference between positions (2) and (3) is emitted as phonons to the lattice. After $10^{-9} - 10^{-8}$ s the system relaxes back from the excited to the ground electronic state, emitting luminescence of energy equivalent to the energy difference between (3) and (4). The line is here also vertical, by the same argument as the absorption from (1) to (2). The energy difference between (4) and (1) is released as phonons. Then the cycle is repeated.

If $Q_{GS} \approx Q_{ES}$, the system cycles between (1) and (3). Such events produce zero phonon lines (ZPL) with energy equal to the difference in energy between (1) and (3) (E_{ZPL}), as no phonons are emitted to the lattice vibrations. Increasing the distance between the Q_{GS} and Q_{ES} increases the phonon sideband which can be seen as wider features in optical characterization methods e.g., CL. ZPLs are characterized as sharp, narrow lines in the e.g, CL spectra.

Single photon sources

Secure quantum communication schemes that Single-Photon Emitters (SPEs) are useful and sometimes necessary. A single-photon source (SPS) ideally emits one photon at a time on demand and the photons should be indistinguishable. The single-photon light source should have a very high probability of either emitting two or more photons or none at all. SPSs are often characterized by a sharp and distinguishable ZPL.

Fluorescent atomic defects and quantum dots (QDs) in solid-state hosts, e.g. semiconductors, are the most promising single-photon sources. Ideally, they need to have a tunable wavelength (ideally in the telecom range), a high emission efficiency with a defined polarization and they can be excited electrically to be utilized as SPSs. Problems regarding an inhomogeneous distribution of defects within the host cause variability between photons from emitters. One emitter can also cause distinguishability because of homogenous linewidth broadening. Host materials with high refractive index cause problems for extracting the photons from the material.[15]. Therefore, researching new materials and material structures, such as nanowire waveguides to incorporate SPE is of interest. This includes the study of SiC particles as SPS in quantum technology.

2.3 Silicon Carbide

Silicon carbide (SiC) is a wide bandgap, covalent material consisting of equivalent amounts of Si and C oriented in a tetrahedral manner. Strong covalent and partly ionic bonds provide a material almost as hard as diamond, and its bandgap results in excellent thermal and electrical properties. The material possesses properties utilized in high frequency, high power and high-temperature electronics. First and foremost, it was developed for power electronics but has proven to be useful in a variety of other applications, for example, sandpaper and as car components. It is only recently that the interest in SiC in quantum technology applications has increased [16]. The wide bandgap enables the possibility of bandgap active emitters, such as donor-acceptor defects and colour centres. In this section, important properties of several polytypes of SiC will be introduced together with point defects in the material, a key feature for single-photon emission used in QT.

SiC is a synthesized material as there is no evidence of SiC occurring naturally, except in a few meteorites. The Acheson process is a common method to fabricate SiC. In the process, Silica (SiO_2) and Carbon (C) are heated in an electrical resistance furnace resulting in SiC crudes with set chemistry, structure and quality depending on the fabrication conditions.

Typically, a SiC wafer consists of two parts, a bulk SiC substrate fabricated with the seeded sublimation method (SiC does not melt) and an epitaxial layer, which is considered the active layer. The seeded sublimation process is divided into three steps. First the SiC source, for example, SiC crudes, is sublimated in a crucible before being transferred to the inner part of the crucible. There, SiC nucleates into high-quality platelets [17]. The epitaxial layer is typically grown with chemical vapour deposition (CVD) with monosilane and propane as precursors, and hydrogen gas as carrier gas. The SiC platelets are often etched before the CVD to remove damage on the surface. The CVD step often requires $1500 - 1650°$ C. During growth, acceptors or donors can be introduced [17].

The powder studied in this work is produced by crushing and milling the SiC crudes and is hence considered to have high purity.

2.3.1 Crystal Structure and Polytypes

The tetrahedral arrangement of one Si atom and four surrounding C atoms (and vice versa) is the fundamental building block of all SiC-polytypes. The atomic bonds are covalent but have a unique ionic character, with the electron density condensed around the C atoms. Close-packed hexagonal planes of Si-C atom pairs are stacked to form SiC crystals.

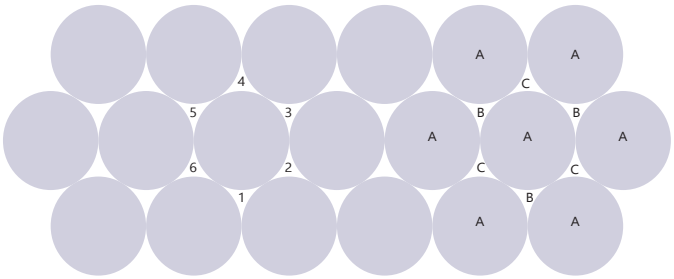

Figure 2.5: The first A - layer of closed packed spheres. Each sphere is surrounded by six voids, where the spheres are the next layers that can be positioned. B- layers are created by placing spheres above the voids labelled with 1, 3 and 5, while a C- layer is stacked above 2, 4 and 6. The c - axis is normal to the paper plane.

SiC tetrahedrons have two configurations. One where a tetrahedron is turned 180° around the c - axis relative to the other. Secondly, two tetrahedrons are mirrored images of each other where the c- axis is parallel to the mirror. The c - axis is the direction normal to the SiC bilayers (the normal to the paper plane in Figure 2.5).

SiC has a hexagonal close-packed arrangement with three types of sites (A, B, C) also shown in Figure 2.5. Stacking the bilayers with specified, repeated tetrahedrons with different arrangements along with the c - axis gives rise to the 250 unique atomic structures, named polytypes, which have to date been identified [18]. 6H, 4H, 3C and 15R, shown in Figure 2.6, are four of the most common polytypes and are all present in the powder.

The names of the polytypes are in Ramsdell notation, where the letter describes the lattice type (H for hexagonal, C for cubic and R for rhombohedral), while the number indicates the number of stacked bilayers of Si-C. Each polytype has its lattice constants, energy band gap, charge carrier mobility, and density of states in the conduction and valence band.

Concerning the immediate neighbours, one Si (or C) atomic layer in the stacking sequence can have a local cubic (k) or hexagonal (h) environment. 3C-SiC has a k-type atomic configuration, and 2H-SiC has only h-type, while 4H and 6H - SiC have both h and k configurations. In some circumstances, it is also possible to distinguish between different types of h-type and k-type layers.

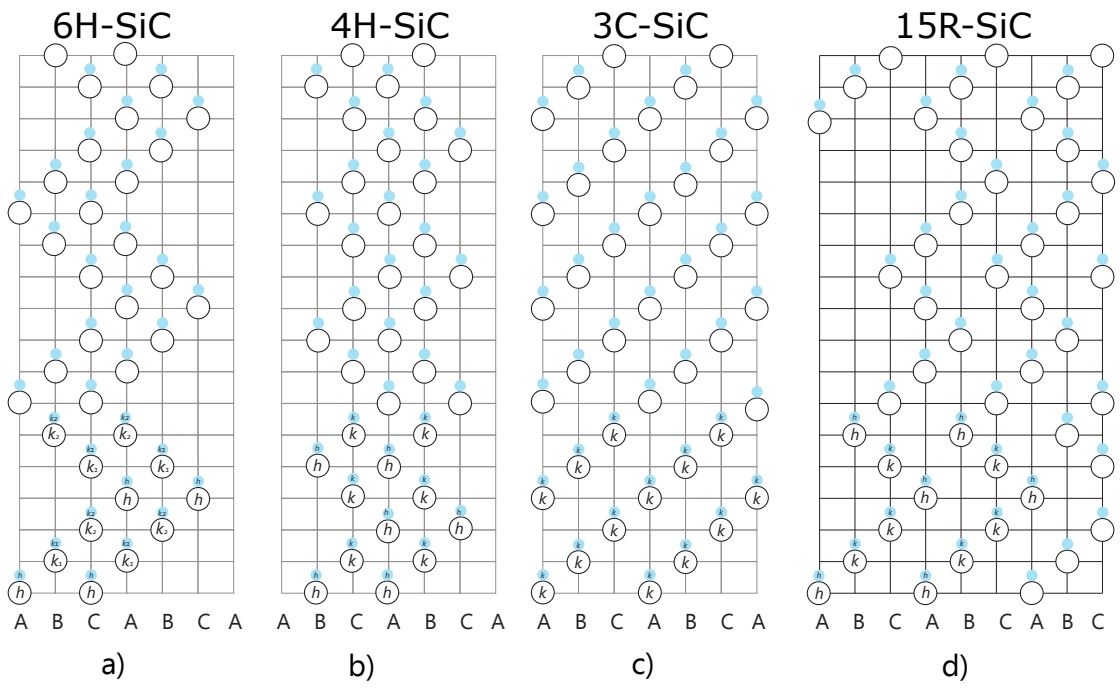

Figure 2.6: Schematic illustration of stacking layers of different polytypes of SiC. a) 6H, b) 4H, c) 3C and d) 15R along with the c - axis. 'k' and 'h' denote atoms having localized cubic and hexagonal crystal symmetry.

These distinctions are due to variances in the kind of more distinct layers. If this is the case, subscripts are assigned the respective letter. The local environment of h- and k atoms is illustrated in Fig. 2.6.

The electronic, indirect bandgap varies from 2.4 to 3.3 eV from the cubic (3C) to the hexagonal (2H) structure. It has been shown that the bandgap is close to linear with the degree of hexagonality of the structure ranging from 3C which has a 0% hexagonality (100 % cubic) and 2H which is 100 % hexagonal. Some structural and electrical properties are summarized in Table 2.1.

Table 2.1: Structural and electrical properties of common polytypes of SiC. 2H is included for completeness. The letter representing the lattice site is illustrated in Fig.2.6. The c-direction is perpendicular to the basal plane of the H polytypes. Ref.[19] and [20].

Polytypes (Ramsdell)	**3C**	**6H**	**15R**	**4H**	**2H**
Stacking order (ABC)	ABC	ABCACB	ABCACBCABACABCB	ABCB	AB
Hexagonality (%)	0	33.3	40	50	100
Experimental bandgap (eV)	2.39	3.02	2.99	3.26	3.33

2.3.2 Point Defects in Silicon Carbide

Production methods of SiC have been developed to the level where the presence of unintentional defects, such as imperfections and stacking faults in polytypes, can to large extent be avoided. Instead, defects intended for QT are intentionally introduced by e.g., ion implantation or during growth. SiC has shown to host many defects in its large bandgap, but not all are quantum technology-friendly.

The complexity of SiC with its many polytypes provides a tremendous number of possibilities where one type of defect can sit in several positions in the lattice as well as slightly different properties in the different polytypes. Some of these defects and configurations are suited for quantum technology, while others are not. One example is the silicon-vacancy (V_{Si}) for its single-photon emission and long-lived and coherent spin ground state. Others are the carbon antisite-vacancy pair ($C_{Si}V_C$), the nitrogen-vacancy, NV-center, (N_CV_{Si}), and the divacancy, VV ($V_{Si}V_C$). Commonly, one charge state, for example, caused by trapping electron(s) (or holes), of a defect is QT compatible. For instance, only the negative charge state of the silicon-vacancy (V_{Si}^-) in 4H-SiC is a bright and has a high-spin ground state and is hence quantum compatible.

Defects such as the carbon vacancy (V_C), are considered a low-spin defect and have no detectable optical transitions.However, the V_C is considered a vital in power electronics as it is lifetime-limiting [21]. Other defects without the necessary properties for quantum technology are the interstitial defects, (Si_i and C_i), and the antisites (Si_C and C_{Si}). However, through implantation and annealing, it is possible to achieve the formation of quantum defects. Impurities in SiC are also candidates for single-photon emitters. Reported ZPLs from the above-mentioned defects, and more, are summarized for the 6H, 4H, 3C and 15R polytypes are in Table 2.2.

Table 2.2: Reported ZPL in energy (E) and wavelength (λ) for 4H, 6H, 3C and 15R - SiC reported in literature (Ref). '—"—' indicates the same as (ref.) as above.

Name	**E (eV)**	**λ (nm)**	**Ref.**
		6H - SiC	
CAV	1.672	741.1	[22]
	1.658	747.6	—"—
	1.650	751.5	—"—
	1.635	757.9	—"—
	1.631	760.1	—"—
	1.621	764.4	—"—
	1.612	768.9	—"—
V_{Si} (V1)	1.433	865	[23, 24, 25]
V_{Si} (V2)	1.398	887	—"—
V_{Si} (V3)	1.367	907	[23, 24]
	1.368	906	[25]
V_CV_{Si} (VV)	1.134	1093	[23]
	1.119	1108	—"—
	1.103	1124	—"—
	1.092	1135	—"—
	1.088	1140	—"—
	$1.089 - 1.135$	$1092 - 1139$	[24]

Name	**E (eV)**	**λ(nm)**	**Ref.**
Ti	2.786 – 2.959	419 – 445	[24]
$Nb_{Si}V_C{}^0$	1.361 – 1.369	906 – 911	—”—
Cr^{4+}	1.156 – 1.182	1049 – 1069.5	—”—
Mo^{5+}	1.106	1121	—”—
W^{5+}	0.996 – 1.002	1237 – 1245	—”—
N_CV_{Si}	0.9710	1278	[23]
	0.934	1328	—”—
	0.922	1345	—”—
V^{4+}	0.898 – 0.948	1308 – 1388	[24]
	0.947	1309	[23]
	0.917	1352	—”—
	0.893	1389	—”—
	4H - SiC		
Si_C (D1)	1.292 – 2.198	564 – 690	[26, 22]
CAV^+	1.911	648.7	[23, 22]
	1.905	651.8	—”—
	1.864	665.1	—”—
	1.855	668.5	—”—
	1.846	671.7	—”—
	1.835	675	—”—
	1.833	676.5	—”—
TS1 (unknown)	1.613	769	[27, 28]
TS2 (unknown)	1.527	812	—”—
TS3 (unknown)	1.525	813.3	—”—
V1’	1.444	858.7	[27]
V1	1.439	861.4	[23, 27, 24]
	1.438	862	—”—, [25]
V2	1.352	917	—”—
V_CV_{Si} (VV)	1.150	1078	[23]
	1.119	1108	—”—
	1.096	1131	—”—
	1.095	1132	—”—
PL6	1.194	1037.9	[29]
PL5	1.190	1141.9	—”—
N_CV_{Si}	1.051	1180	[24, 23]
	1.014	1223	—”—
	0.999	1241	—”—
	0.998	1242	—”—
Ti	2.792 – 2.850	435 – 444	[24]
$Nb_{Si}V_C{}^0$	1.384 – 1.508	822 – 896	—”—
UD3 (unknown)	1.356	914.1	
Cr^{4+}	1.190	1042	—”—

Name	**E (eV)**	**λ(nm)**	**Ref.**
Cr^{4+}	1.159	1070	—"—
Mo^{5+}	1.152	1076	—"—
Mo	1.106	1121	[23]
$V_C V_{Si}{}^0$	1.090 – 1.150	1078 – 1132	[24]
	1.184 – 1.196	1037 – 1047	—"—
W^{5+}	1.059 – 1.059	1170 – 1171	[24]
$N_C V_{Si}{}^-$	0.998 – 1.054	1176 – 1242	—"—
V^{4+}	0.929 – 0.970	1278 – 1334	—"—
	0.969	1279	[23]
	0.929	1335	—"—
	3C - SiC		
V_{Si} (V1)	1.100	1127	[23]
V_{Si} (V2)	1.121	1106	[24]
$V_C V_{Si}$ (VV)	1.121	1106	[24, 30]
	1.367	1127	[23]
$N_C V_{Si}{}^-$	0.861	1440 (calculated)	[24]
	0.845	1468	[23]
Ky5 (1)	1.121	1106	[30]
Ky5 (2)	0.954 – 1.127	1100 – 1300	[31], [32]
	15R - SiC		
V_{Si} (V2)	1.399	886.5	[25]
V_{Si} (V3)	1.372	904	—"—
V_{Si} (V4)	1.352	917	—"—
U_{a1} (UD-4)	1.431	866.4	[33]
U_{b3} (UD-4)	1.377	900.4	—"—
U_{15R} (UD-4)	1.387	893	—"—

2.4 Modelling Computational Electrodynamics

Numerical calculations of electromagnetic fields are of interest for understanding the luminescence pattern from the individual particles studied in this work. The Finite-Difference Time-Domain (FDTD) is one way of implementing the propagation of electromagnetic waves.

The method achieves discretisation of Maxwell's equations in the space-time dimensions. In 1966 Yee proposed a way to write the derivatives in these equations as finite differences to be solved numerically in the time domain [34]. By doing so, electromagnetic interactions, such as propagation, reflection, scattering, diffraction and more, can be numerically calculated. Further, by doing Fourier transforms, it is possible to obtain the frequency solution and, hence the reflected and transmitted light. This section is based on parts of Taflove and Hagness [35] and it introduces the physics behind the FDTD method.

Maxwell's equations are four differential equations used to solve problems within classical electromagnetism, classical optics and electric circuits. Gauss law describes the divergence of the electric displacement field in volume given by equation 2.5

$$\vec{\nabla} \cdot \vec{D} = \rho \tag{2.5}$$

Where ρ is the free charge density inside the volume and the dielectric displacement field $\vec{D}$ s given by

$$\vec{D} = \epsilon_0 \vec{E} + \vec{P} \tag{2.6}$$

ϵ_0 is the permittivity in free space, $\vec{E}$ and $\vec{P}$ are the electric and field and polarization, respectively. Gauss law for magnetism yields a zero divergence of the magnetic flux density $\vec{B}$

$$\vec{\nabla} \cdot \vec{B} = 0 \tag{2.7}$$

The change of magnetic flux density inducing an electric field is given by Faraday's law.

$$\vec{\nabla} \times \vec{E} = -\frac{\partial \vec{B}}{\partial t} \tag{2.8}$$

The last of the four equations is Amperes law,

$$\vec{\nabla} \times \vec{H} = \vec{J} + \frac{\partial \vec{D}}{\partial t} \tag{2.9}$$

where $\vec{J}$ is the free current density and

$$\vec{H} = \frac{1}{\mu_0}\vec{B} - \vec{M} \tag{2.10}$$

μ_0 is the permeability of free space and $\vec{M}$ is the magnetization.

FDTD calculation procedure

The equations are solved in a discrete spatial and temporal grid, called the Yee-cell, shown in Figure 2.7. In each grid of the cell, a field component is solved. The electric components are solved along the edges and the magnetic on faces, half a step away from the electric. There are many such cells in the simulation region. The smaller they are, the more accurate the results become. At $t = 0$ of a simulation both the magnetic and electric fields are usually set to zero,

$$\vec{E}^{-\frac{1}{2}} = 0, \qquad \text{and} \qquad \vec{H}^0 = 0 \tag{2.11}$$

Further, the fields are calculated in the time-step $n + \frac{1}{2}$. Hence, the electric field becomes dependent on the previous time step, plus the curl of the magnetic field given by equation 2.9, at a time n, given by

$$\vec{E}^{n+\frac{1}{2}} = \vec{E}^{n-\frac{1}{2}} + \frac{\Delta t}{\epsilon}\vec{\nabla} \times \vec{H}^n \tag{2.12}$$

Δt is the time interval and ϵ is the permittivity of the material. Thereafter, the magnetic field is calculated at time $n + 1$. The term is dependent on the field in the previous step $\vec{H}^n$ and is proportional to the curl of the electric field, as seen in 2.7, at time $n + \frac{1}{2}$,

$$\vec{H}^{n+1} = \vec{H}^n - \frac{\Delta t}{\mu}\vec{\nabla} \times \vec{E}^{n+\frac{1}{2}} \tag{2.13}$$

μ is the permeability of the material. Continuing in the following pattern

$$\vec{H}^0 \to \vec{E}^{\frac{1}{2}} \to \vec{H}^1 \to \vec{E}^{\frac{3}{2}} \to \vec{H}^2 \to \vec{E}^{\frac{5}{2}} \to \cdots \tag{2.14}$$

until the fields are converged within a set value.

Lastly, the electric field is interpolated to the final time step, because of the time step calculation offset. This is done so both the electric and magnetic fields can be analyzed at the same time step. The electrical field is normalized with the factor $\tilde{E} = \sqrt{\frac{\varepsilon_0}{\mu_0}} E$.

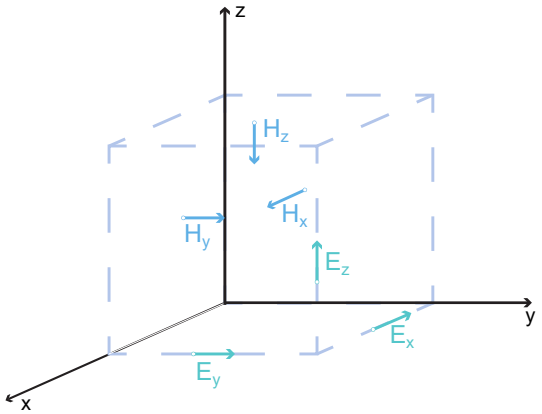

Figure 2.7: Yee cell showing the positions of where the field components are solved.

The time step is defined as: $\Delta t = \frac{\delta x}{2 \cdot c_0}$, where c_0 is the speed of light in free space. As an electromagnetic wave is limited to the speed of light, the minimum time step is $\Delta t = \delta x / c_0$. In two dimensions it changes to $\Delta t = \delta x / (\sqrt{2} c_0)$ as the wave can travel along the diagonal of a plane. In three dimensions it becomes $\Delta t = \delta x / (\sqrt{3} c_0)$. The condition is described by the 'Courant Condition'. Meaning implementing a smaller mesh will increase the simulation time.

$$\Delta t \leq \frac{\Delta x}{\sqrt{n} \cdot c_0}, \qquad \text{n: dimension of simulation.} \tag{2.15}$$

Chapter 3

Methodology

This chapter aims to give insight into methods used to make the samples and to numerically calculate and characterize the silicon carbide particles. Photoluminescence spectroscopy gives an insight into what the powder contains in terms of colour centres. This technique has a low spatial but high spectral resolution. Therefore it will indicate which spectral range to search with cathodoluminescence spectroscopy. The principles of a Secondary Electron Microscopy will be covered as it is used to map the geometries and sizes of the SiC particles. Moreover, the instrument is needed to perform energy dispersive X-ray spectroscopy and cathodoluminescence.

Cathodoluminescence spectroscopy optically characterizes the particles. The interaction between matter, electrons and photons give an incredible, detailed insight into the electronic structure of semiconductors and the detection of defects. By taking advantage of the high resolution, it is possible to gain insight into the high-intensity emission from the particles and better understand the emission profile from specific particles.

To better understand the emission profile from the particles, especially the influence of the shape and sizes of the SiC particles, the Finite-Difference Time-Domain (FDTD) method is used. Implementing simulations together with optical characterization is inspired by Radulaski et al. [36] FDTD simulations yield, among other things, the electromagnetic field as a far-field projection. However, the environment in the simulations is highly idealized and disregards features such as surface roughness and the influence of emission from surrounding particles. Therefore, the simulations are used here to aid the understanding of the emission pattern rather than for direct comparison with cathodoluminescence spectroscopy.

3.1 Sample Preparation

The silicon carbide (SiC) provided by Washington Mills is in powder form, with particle sizes from a few hundred nm and an average of 4 µm. Due to the sample requirement of SEM cathodoluminescence, the powder was distributed on a silicon wafer. The SiC particles stuck to the surface of silicon wafers reasonably well. There is reason to believe that it is due to electrostatic forces. Exposing the SiC particles to a high current and energy electron probe in the secondary electron microscope (SEM), the particles remain stationary. However, observations of particles "running away" from the sample occurred if the electron probe focused on a large chuck of particles. Hence, it was important to evenly distribute the particles such that there were no chunks and one thin layer.

To increase the concentration of intrinsic defects relevant for QT, the samples with powder were both irradiated with protons at different doses and submitted to a series of heat treatments.

Herein is described the sample preparation to meet the requirements above. A summary of the samples studied in this work, together with sample ID for later convenience, is given in Table 3.1.

Sample preparation

The following steps were completed to create the samples for study in this thesis. It should be mentioned that the process is inspired by similar sample preparation in previous work by the research group.

1. **Laser cutting** the silicon 100 x 100 mm wafer into 7 x 7 mm samples. The samples were cut in a MASTER Mini PSG-532 laser cutter from ELAS.

2. The cut silicon samples were **cleaned** in an ultrasonic bath with acetone for 30 minutes to remove any surface contaminants. After cleaning, the samples were rinsed with deionized water and blow-dried with nitrogen gas before being stored in plastic bags. T

3. The SiC micron-sized powder was **distributed** on the Si wafer surface by scraping a thin scalpel dipped in powder across the sample approximately ten times. Other methods were tested, such as sprinkling the powder over the Si surface. However, studying the distribution of the powder by SEM imaging revealed many lumps and thick layers compared to a thin, even layer from the "scalpel" method desired to study individual particles.

4. To investigate the origin (extrinsic or intrinsic defects) of the illumination from the particles **ion irradiation** with protons was done. The proton irradiation was expected to yield an increase in the concentration of intrinsic defects point defects. Ion irradiation is more attractive than a doping method because of the poor diffusivity of dopants [37].

   1×10^{14} cm^{-2} protons with energy of 1.8 MeV were irradiated 8° off-axis with respect to the surface normal at room temperature. The energy was set to ensure the protons go through the SiC particles and to introduce defects in both the silicon and carbon sublattices. Off-axis irradiation is a normal practice for SiC wafers, but as the particles were randomly oriented on the Si wafer, this step was not necessarily needed.

   Proton irradiation is expected to, amongst others, monovacancies and interstitials [38] (4H-SiC). This procedure was performed by the instrument responsible, Viktor Bobal. The instrument used was a Tandem Accelerator from NEC.

5. The samples were subsequently **annealed** at 300° C and 1000° C for 30 minutes with a nitrogen gas flow of 30 ccm. After the completed annealing time, the samples were taken to room temperature and rapidly cooled. The purpose of the heating was to utilize diffusion of the defects created with irradiation to alleviate irradiation damage and reduce the amount of nonradiative channels. The temperature where chosen based on the stability of known quantum defects in SiC. For example, the luminescence from the silicon-vacancy is expected to be observed after irradiation and 300° C anneal, while the divacancy is promoted at higher temperatures such as 1000° C. Post-irradiation annealing was done in an open GSL1100X Birkeland Tube furnace.

Table 3.1: Annealing treatment and irradiation dose of H^+ irradiated SiC-powder samples.

Annealing treatment	**irradiation Dose** (cm^{-2})	**Sample ID**
None	0	0 - RT
1 atm N_2 at 300°C / 30 min	1×10^{14}	1E14 - 300C
1 atm N_2 at 1000°C / 30 min	1×10^{14}	1E14 - 1000C

3.2 Optical Characterization of Defects

The emission of visible light, luminescence, occurs when electrons in a material are excited by an energy source (electrons, laser light, UV lamp) into a higher energy state. Electrons relaxing from a higher to a lower state release energy. The recombination process is either radiative or non-radiative. If the conditions are right, the process *can* result in the emission of a photon. The correlation between energy (E) in eV and wavelength (λ) in nm is given by:

$$E(\lambda) = \frac{hc}{\lambda} = \frac{1240}{\lambda} \tag{3.1}$$

For correct wavelength to energy conversion, the Jacobian transformation together with Equation (3.1) yields

$$I_E = I_\lambda \frac{hc}{E^2} \tag{3.2}$$

where E is the energy, λ is the acquired wavelength, h is Planck's constant and c is the speed of light. I_E and I_λ are the intensity after and before the conversion, respectively [39, 40].

3.2.1 Photoluminescence Spectroscopy

Photoluminescence (PL) is the spontaneous emission from materials under optical excitation. PL spectroscopy utilizes this phenomenon, revealing the optoelectronic properties of semiconductors. The method is non-destructive, contactless and versatile, optimal for optoelectrical characterization of semiconductors. Measurements yield a wavelength versus intensity spectrum.

When a photon with energy $hv \geq E_g$ hits a material, it can be absorbed through the excitation of an electron from the valence band to the conduction band. Subsequently, the excited electron can relax by emitting a photon. The emitted photons can give detailed information about the materials' discrete electronic states. The signal is due to radiative recombination of the electrons, yielding information about band transitions and intrinsic and extrinsic defects.

There are two main factors for managing and adjusting the PL measurements. Optical excitation energy regulates the probing depth in the sample. Tuning the same parameter specific optical transition can be studied. The intensity of the excitation beam is critical for governing the density of excited electrons. The density is essential for understanding recombination processes. Pulsed optical excitation is utilized for analyzing short term events in the material, such as recombination events.

There are many applications for PL spectroscopy. Examples are determinating bandgaps, identifying defects and impurity levels and analyzing radiative recombination processes. Surface and material quality are examined with PL and quantitative PL, respectively.

It is difficult to apply PL to materials dominated by non-radiative recombination mechanisms or materials where the emission efficiency is low as PL relies on radiative events. Another shortcoming of PL is the difficulty in estimating the density of interface and impurity states. When these states have radiative levels, they are readily identified in the PL spectrum, and the size of the associated PL peaks provides a relative measure of their presence in the sample. However, measuring the absolute density of these states is a far more formidable task and typically requires an exhaustive analysis of the excitation intensity dependence of the PL signal.

PL is suitable for high resistivity materials as there is no need for electrical contacts and junctions. Minimal sample preparation is needed because there is no electrical excitation or detection. Hence, the method is convenient for materials with high resistivity or poorly developed contact technology.

The luminescence properties of materials are highly dependent on temperature. Liquid helium temperature is often utilized to obtain high spectral resolution. However, room temperature measurements are, for some purposes, sufficient. Compared to other optical characterization methods, such as reflection and absorption measurements, PL is less strict with beam alignment, surface flatness and sample thickness [41].

A typical, simplified PL set-up is shown in Figure 3.1a together with a imaginary PL spectra in Figure 3.1b. The PL instrumentation used to investigate the optical emission properties of 6H-SiC powder particles at 10 K is herein given. A closed-cycle He refrigerator system (CCS-450 Janis Research, Inc.). Photo-excitation was performed using a 325 nm wavelength of continuous wave (cw) HeCd laser (photon energy 3.81 eV, power density 20 W cm^{-2}). PL signal was collected in a back-scattering geometry by a microscope objective (Mitutoyo, LWD 10X), spectrally filtered (long-pass LP 800-nm filter) and analyzed by an imaging spectrometer (Horiba, iHR320) coupled to an EMCCD camera (Andor, iXon Ultra 888) with a spectral resolution below 0.2 nm.

3.2.2 Scanning Electron Microscopy

The Scanning Electron Microscope (SEM) can characterize the surface of materials and elemental composition. Images are made by detecting signals produced by a focused electron beam scanning over a material surface. The signals originating from the beam-sample interaction can give information about the sample topography and composition, with a resolution of 4 - 10 nm, enabling up to 200 000 times magnification. This section is based on [42, 43] and supports the following section concerning energy dispersive X-ray and cathodoluminescence spectroscopy.

The microscope has two major components, the microscope column and the electronics console. An electron gun, usually a tungsten filament or LaB_6 single crystal, sits on top of the microscope column, as shown in Figure 3.2. When heating the filament/crystal, an electron beam is emitted and accelerated by a voltage of 0.5 - 30 keV from the cathode in the electron gun to the anode. The beam passes condenser lenses to reduce the beam diameter from 10 - 50 µm down to 5 - 10 nm. The aperture narrows the electron beam diameter. A metal plate with a small hole placed between the condenser and objective lens limits wide-angle electrons. The objective lens focuses on the beam.

Magnification, M, is controlled by applying current in the x- and y- scanning coils and is given by $M = \frac{\text{Scanning distance in image}}{\text{Scanning distance on the specimen}}$. The beam is moved in the x and y directions by two-wave

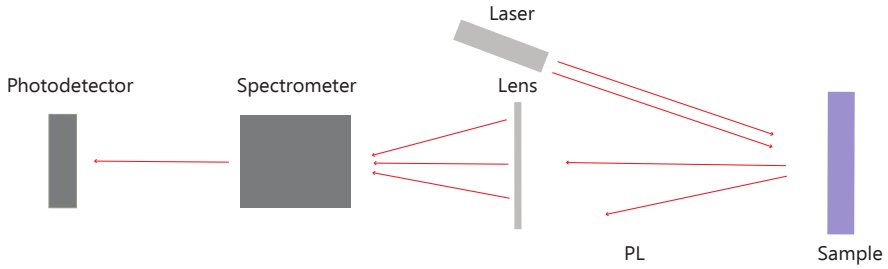

(a)

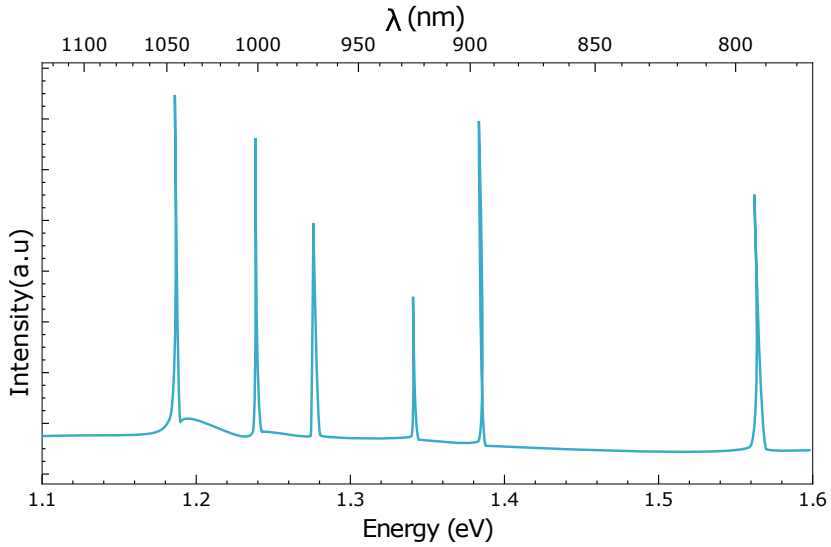

(b)

Figure 3.1: Schematic illustration of an (a) typical set-up for PL measurements (b) imagined PL spectra from an imagined measurement with features at different wavelengths.

generators operating at different frequencies. The resulting electron probe current is in the range of a few tens of pA to a few nA in the instrument used in this work.

In the lower end of the microscope, column sits the specimen chamber, which under use is evacuated to approximately $10^{-3} - 10^{-4}$ Pa using a combination of pre-vacuum and high-vacuum pumps. This measure is necessary to reduce the collision and interaction between molecules and incident electrons. The specimen is mounted on a movable sample stage (x,y,z, tilt and rotation) in the lower part of the chamber. The sample stage can be attached to a cooling system to perform cryogenic measurements.

An SEM operator can control electron - acceleration voltage - determining the penetration depth in the specimen, working distance - the distance between the sample and objective lens, probe current and aperture of the objective lens to control spherical aberration - a problem occurring due to the lens failing to converge all of the ray paths to the same focal point.

The secondary electrons from the specimen (see Figure 3.3b) are detected by a secondary electron detector, and the amplified signal is displayed on an LCD screen, forming an SEM image. The brightness is varied by differences in the amounts of secondary electrons emitted by the sample at different positions. Altering the scan speed yields images for different purposes. Fast scan speeds

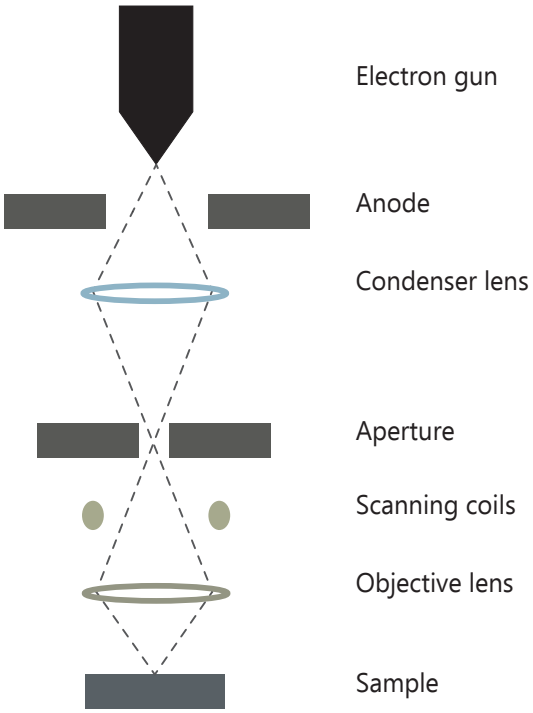

Figure 3.2: Schematic illustration of a Scanning Electron microscope (SEM) with main components.

are used for observation, while slower scan speed is used for acquisition and saving images.

It is important to understand the origin of the contrast in an SEM image. Incident beam electrons entering the specimen scatters and gradually lose their energy. How far down into the specimen electrons scatter is dependent on the incident electron energy, the atomic number of the elements in the specimen and the density of the constituent atoms, where the scattering range is proportional to the first and inverse proportional to the two latter. Figure 3.3b is a schematic illustration of the different signals emitted from the specimen.

Secondary Electrons (SE) are valence electrons from the specimen elements emitted due to inelastic scattering with the incident electrons. The SE are characterized by their low energy, below 50 eV. As a consequence, many SEs are reabsorbed in the sample. However, closer to the surface (up to $\sim$ 20 nm) there is a greater chance of them escaping. Hence, SE gives surface-sensitive information. Emission of SE is stronger from surfaces that are not perpendicular to the incident beam, yielding a higher brightness in the SEM image. Therefore, SE is used to observe the surface topography of a sample surface.

Backscattered Electrons (BSE) possesses higher energy compared to SE and are scattered elastically, shown in Figure 3.3b b). As a result, the BSE signal contains information from further down in the sample ($\sim$ 500 nm with 20kv in SiC). BSE are sensitive to the atomic number of the elements in the specimen. A higher atomic number yields higher intensity of the signal. hence, the BSE signals give information about the composition of a sample, particularly where multiple material phases are present. Figure 3.4 gives an idea of the origin and depth of the different signals discussed herein relative to each other.

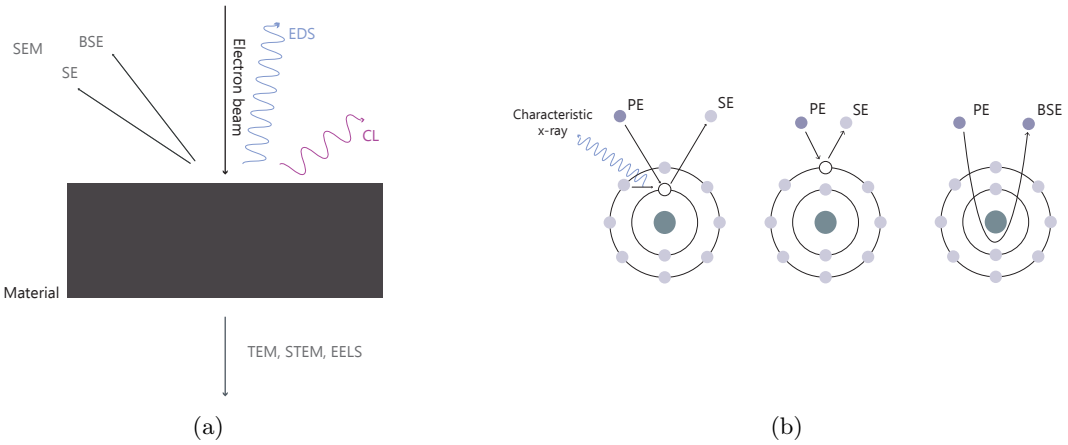

(a) (b)

Figure 3.3: (a) Schematic illustration of different signals produced in a Scanning Electron microscope (SEM). (b) Emission mechanisms of (from the left) characteristic x-rays, backscattered electrons and secondary electrons when incident beam electrons interact with the sample species. Characteristic x-rays are produced when a high energy electron relaxes into the lower, empty state created by the primary electron.

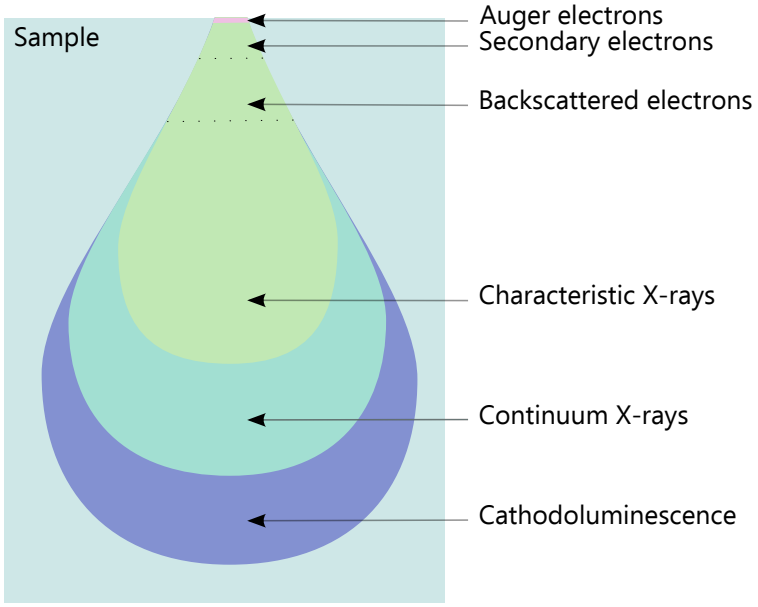

Figure 3.4: Interaction volume showing where the different signals are produced relative to each other in a sample.

The SEM model in the MiNaLab is a JEOL JSM-IT300 with a LaB_6 filament. The microscope can achieve magnification up to 200 000 x with a resolution of 4 - 10 nm. In the specimen chamber, there are detectors for secondary electrons, backscatter electrons, and a ThermoFisher UltraDry electron dispersive X-ray spectroscopy (EDS) for chemical analysis. The e-beam current (10 pA to approx 1 µA) is monitored with a Keithley 6485 PicoAmperimeter. The temperature for low-temperature measurements was monitored with the Gatan Model 1905 Temperature Controller for the Gatan c1002 cold stage operates at 80 K to 473 K with a liquid nitrogen cooling system.

3.2.3 Cathodoluminescence Spectroscopy

In cathodoluminescence (CL), samples are excited by an electron beam rather than light. The physics governing the signal generation is similar in PL and CL. Observable luminescence from CL ranges from the ultraviolet (UV) to the mid-infrared (IR).

Semiconducting materials have a unique energy bandgap separating the empty conduction band and filled valence band. Valence band electrons can interact with incident electrons or secondary electrons, and gain sufficient energy to be excited to a state in the conduction band. After excitation, a recombination event occurs, where one possibility is a recombination of a conduction band electron with a valence band hole. Other possibilities are recombination via defect, for example via donor and acceptor states within the bandgap. Non-radiative recombination is also possible, e.g., in cases where the excited electron can relax by losing energy to phonons in the sample, causing heating of the material. Indirect bandgap materials, such as Silicon carbide, require a simultaneous transfer of energy and momentum from the excited particle in band-to-band transitions. The process can lead to slower recombination rates in the direct bandgap materials, where no momentum transfer is required.

The primary electrons from the electron gun typically have energies on the order of keV. Such electrons lose their energy through collisions with the sample materials. Secondary electrons are generated in the process, with energies up to $\sim$ 50 eV. Through Monte-Carlo simulations, it is possible to simulate the depth distribution for CL signal generation. Figure 3.5 shows an example of the CL signal distribution from simulation in the Casino software. As shown in Figure 3.4, the CL signal originates from deep within the sample, relative to the other signals of interest.

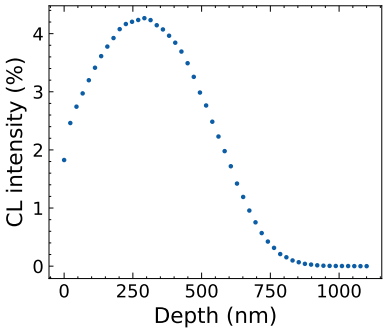

Figure 3.5: CL probing depth in SiC (3.21 g cm^{-1}) from Casino simulations

A common CL setup is shown in Figure 3.6a. The electron beam passes through a hole in a parabolic mirror used to collect the CL signal. A piezoelectric engine permits manual alignment of the mirror so that the electron beam passes through the hole in the mirror and that the excited spot on the material surface is in the focus of the mirror. Emitted photons are reflected from the parabolic mirror and subsequently guided through a filter that can be used to remove the light from wavelength ranges that are not of interest to the specific measurement (less than the bandgap of the detector material). After filtering, the emitted light is sent through a spectrograph and onto a detector where the spectrum is formed. Figure 3.6b shows a schematic CL spectrum.

As phonon scattering and radiative recombination increase with temperature, it is often useful to run the experiment at cryogenic temperatures (in our case 80 K) using liquid nitrogen. This improves the signal to noise ratio.

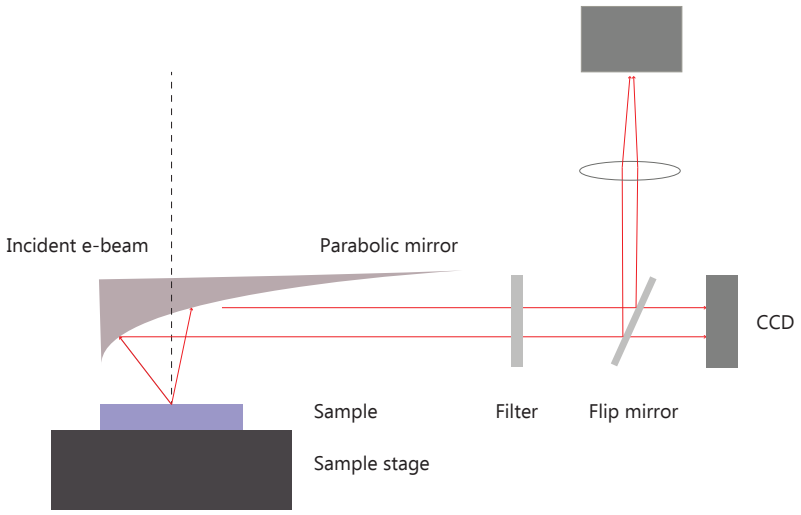

(a)

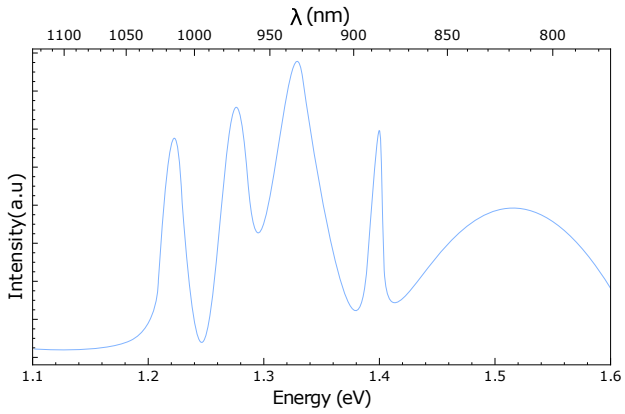

(b)

Figure 3.6: (a) Schematics of a CL setup in a scanning electron microscope. A filter can be utilized to block out parts of the electromagnetic spectra. While the flip mirror is engaged, the light is guided towards the spectrometer for spectral analysis. (b) Schematics of an imagined CL spectrum from an imagined measurement with features at different wavelengths.

CL has a high spatial resolution and sensitivity to the range of fundamental processes in materials, and it is easy to use. Hence it is a great technique for analysing variations in material properties at small scales. The technique is used to characterize and study semiconductors' light emission both in bulk samples and in samples where the light emission varies over microscopic length scales.

Limitations

The limitations in CL spectroscopy measurements are because of:

1. Relative long working distance (WD) (optimal focus usually around WD = 16.7 mm) limits the imaging resolution.

2. The small space between the mirror and sample prevents tilting of the sample during the

measurement, restricting measurements to sample surfaces.

3. CL measurements on high-resistance samples can be difficult since prolonged exposure to the electron beam can cause charging in such materials.

Experimental setup

CL spectroscopy was executed in JEOL JSM-IT300 with the same conditions mentioned in Section 3.2.2 with the addition of a parabolic mirror and optics. The spectrograph used was an Andor Kymera 193i and equipped with UV-Vis and IR detectors. Where convenient we have applied a 500 or 700 nm long-pass filter to enhance features above the filtered wavelengths. Cryogenic measurements at 80 K were done using a liquid nitrogen setup. The acceleration voltage used was 10 keV and the probe currents were in the range of 0.3 - 1.4 nA. For near band-edge emission and wavelengths < 1000 nm, the mentioned probe current sometimes caused saturation on the detector. If so, it was lowered to 0.3 nA. The slit before the spectrograph was for the higher energies set to 320 µm, while for lower energies, 1.0 - 1.4 mm was necessary to observe features. These parameters are valid for the remaining of this work.

3.3 The Finite-Difference Time-Domain method

3.3.1 Simulation Environment

To collect the outputs of the FDTD algorithm, several features are required. A boundary condition defines the simulation area, an electromagnetic source initializes the simulation and a monitor collects the desired data. This section provides an overview of the simulation and discusses the simulation features used in this work. Figure 3.9 summarizes the employed features.

Boundary conditions

The simulation environment is enclosed by a boundary defined by a set of boundary conditions. The Perfectly Matched Layer (PML) boundary is used in this work. This boundary condition absorbs most incident light and reduces reflections by implementing an absorbing material with impedance matching the surrounding materials. It is possible to set different boundaries in different planes. However, to simulate the environment of an isolated particle, which is most appropriate w.r.t. comparisons to CL measurements, the PML boundary was used in all directions.

Mesh

In numerical simulations, there is always a trade-off between simulation accuracy and resource consumption in the form of both memory and time, smaller mesh size increases accuracy, but also memory and time consumption. In three dimensions the memory usage of an FDTD simulation scales with $1/dx^3$ and the time consumption scales with $1/dx^4$, where dx is the size of a mesh cell in the x-direction. The size of the mesh cells has a strong influence on the accuracy of the simulation results as well as computational efficiency. For those reasons, it is important to select the proper size of mesh cells by doing convergence tests to balance accuracy in the results against memory and time consumption..

Within the boundary condition, a uniform mesh is set up by choosing the number of points per wavelength at which the fields are calculated. The size of the mesh cells is captured by the mesh

accuracy parameter. A *graded mesh* offers the possibility to increase the mesh close to structures where a higher density mesh may be needed to accurately capture the variation in the fields. The latter reduces sources of error, such as grid dispersion and the staircasing effect, in a very computationally efficient manner. To check the resolution of the meshed geometrical structures, it can be viewed in the index monitor, shown in 3.7.

Graded meshing offers mainly two new sources of error. The graded mesh area can cause a small gain or loss. This is a result of minor scattering, because of a change in the grid dispersion. The other error is that mesh grading might impact the PML performance resulting in additional reflections. Another issue caused by the size of the mesh cells is the so-called staircasing effect. In a finite mesh, it is not possible to resolve geometrical features to arbitrary resolution. The effect is illustrated in Figure 3.7. By lowering the size of the mesh cells, the inaccuracy is minimized.

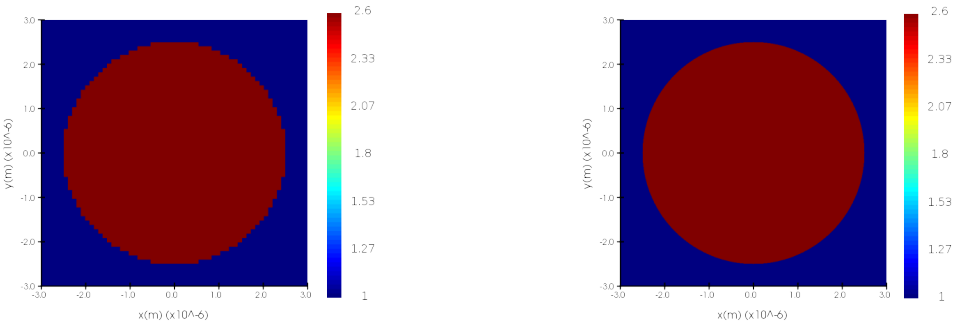

(a) (b)

Figure 3.7: Resolution of a spherical structure with 2 µm in diameter with (a) 0.1 µm and (b) 0.001 µm inner mesh. Data is obtained from a refractive index monitor in the xy-plane.

Monitors

Data, such as the electrical and magnetic fields, is recorded through monitors (as seen in Figure 3.9). Different monitors measure different parameters. The refractive index monitor is used to measure the refractive index of the material (the one used in Figure 3.7), a time monitor measures the electrical field over time, and a frequency-domain power monitor records transmission and reflection through the Poynting - vector.

Materials and structures

The experimentally measured refractive index of a material as a function of wavelength is implemented in the simulation through a multi coefficient material model. The model produces a refractive index function based on tabulated data. As the material in question, 6H-SiC, was not available in the database of the software used, the refractive index was imported from [44] and [45]. The Monte-Carlo Method (MCM) was used to fit the data shown in Figure 3.8, showing the refractive index as a function of wavelength. To compare different polytypes, measured refractive indices from 4H and 3C-SiC were imported from the same sources. Note that data from 15R-SiC was not available.

Various geometrical features, such as cubes, spheres and pyramids, are available in the software, which is easily implemented by setting the position and size (the ones used are shown in Figure 3.9). It is also possible to construct other geometries through scripting.

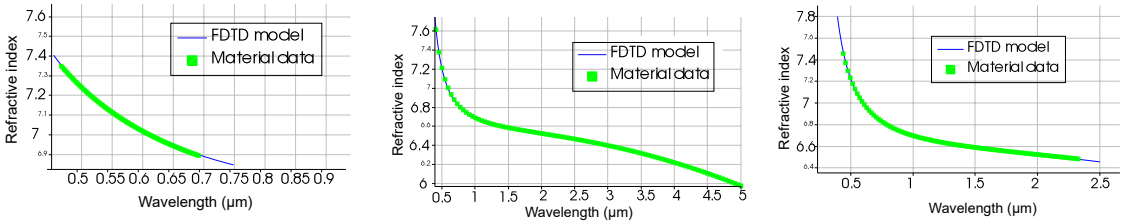

(a) 3C (b) 4H (c) 6H

Figure 3.8: The material fit of three polytypes 3C-, 4H- and 6H-SiC. The y-axis is the real part of the refractive index as a function of wavelength.

Emission sources

In ANSYS Lumerical a selection of sources is provided, such as dipoles, beams, plane waves, total-field scattered field, guided mode source for integrated optical components and an imported source to interface with external photonic design software. A classical simulation tool falls cannot implement quantum mechanical properties, such as single-photon emission. The solution closest to single-photon emitters is a dipole optimized for a short pulse, which emits a single wave packet. The dipole can be set to emit a single wavelength or a span of wavelengths.

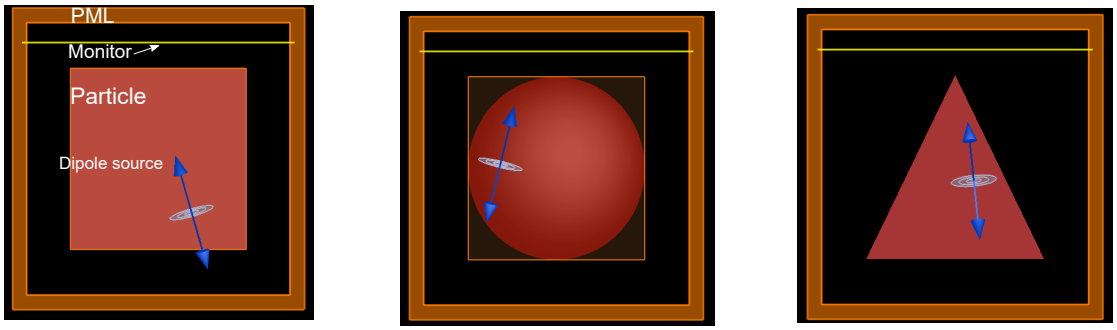

(a) Cube (b) Sphere (c) Pyramid

Figure 3.9: 3D simulation environment of the different particles with the PML boundary condition, the power and field monitor, the dipole source with an angle offset and the particle with shape a) cube, b) sphere and c) pyramid. The images are screenshots from the Lumerical software taken in the XZ plane.

Far field projections

In FDTD the measured EM field is the so-called near-field. However, in comparison to experimental techniques, it is the behaviour in the far-field which is often of primary interest. The fields here are what we regard as "normal" electromagnetic radiation. The near field can be considered as many different fields and a collection of dipoles with a fixed phase relationship. The distinction between the near and far fields is defined by the dominating wavelength and is several wavelengths away

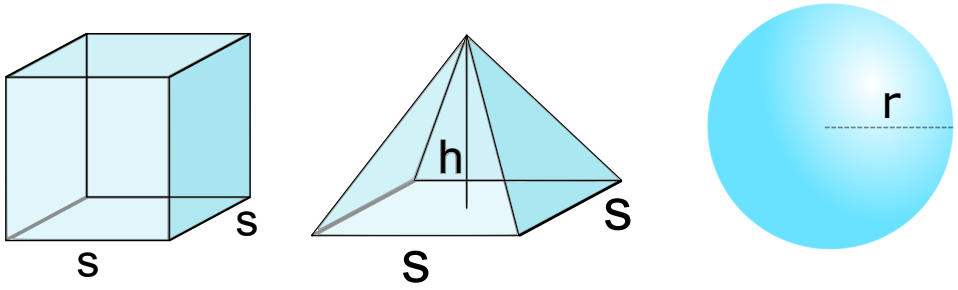

(a) (b) (c)

Figure 3.10: Illustration of the particle geometries (a)cube, (b) pyramid and (c) sphere with the parameters s: side, h: height, and r: radius used to define the size of the simulated particles.

from the near field.

By doing the Fourier transform of a near field with the condition of the field is known everywhere on a plane or closed surface, the far-field can be calculated. In this work, the far-field is set 1 m away from the simulation. The data from the monitor is projected onto a 2D surface as a function of directional unit vectors, ux and uy ranging from -1 to 1. The point (ux, uy) = (0,0) is the centre of the hemisphere where the electromagnetic fields are a result of wave propagation with normal incidence.

3.3.2 FDTD Method Development

The FDTD method was used to simulate wave propagation in the particles to support the experimental results from cathodoluminescence. A framework based on the FDTD algorithm had to be developed before simulating the emission from the SiC particles. This section explains how the simulations were built to imitate emission from the micron-sized particles.

Geometries

We want to resemble the geometry of the particles in the powder. However, as can be seen in Figures 4.1a and 4.2 in section 4.1, the geometry and surface of the particles are complex. We, therefore, chose to simplify the particle geometries to a cube, pyramid and sphere. Figure 3.10 shows how the shape and size of the structures used in the simulations are defined. For the cube, the length of the sides defines the size. The sphere's size is defined by its diameter (2 $\times$ r). The height and length of each side in the bottom plane (s $\times$ s) define the size of the pyramid. The sizes were selected based on the observed size of particles in the SiC powder.

Defects

After irradiation of protons, the SiC particles contain many intrinsic defects, and possibly extrinsic defects as well. Dipole sources were used to mimic an excited defect in the particles. FDTD is a coherent simulation tool, therefore steps need to be taken to create incoherent light, as this is what is expected from the SiC particles. There are several methods to implement incoherent emission, but the most efficient is to run simulations with one dipole at a time. The individual coherent result is then added together incoherently. The electric field (E) of N dipoles from N simulations is then given by

$$|E|^2 = \frac{|E_1|^2 + |E_2|^2 + \cdots + |E_N|^2}{N} \tag{3.3}$$

The positions of the dipole within the particle were randomized using the random number generator provided in the python package, Numpy. A seed was used to produce comparable results. As the SiC particles were randomly oriented on the Si-wafer, the angle of the dipole was oriented randomly in the same manner as the position.

After doing CL measurement it was soon understood that the particles emit more light close to edges, compared to flat surfaces (see section 4.3). To understand this observation, simulations were run with dipoles concentrated in a much smaller area to check the effect on the emission. This is shown in Figure 3.12.

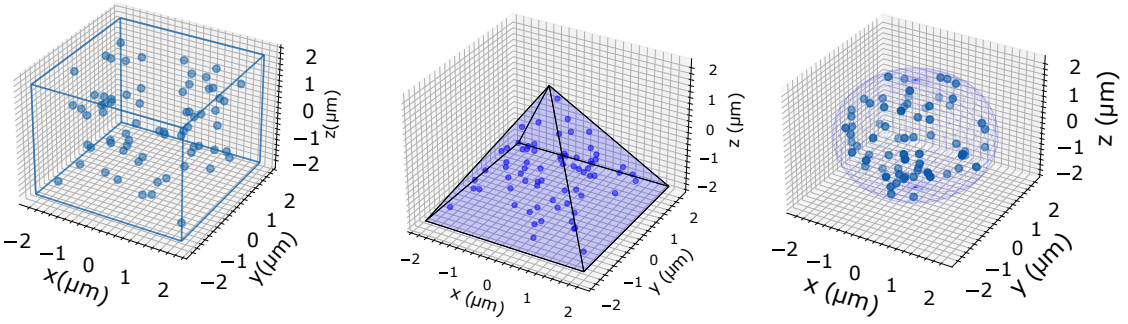

Figure 3.11: Randomized dipoles (blue dots) inside a pyramid, cube and spherical particle

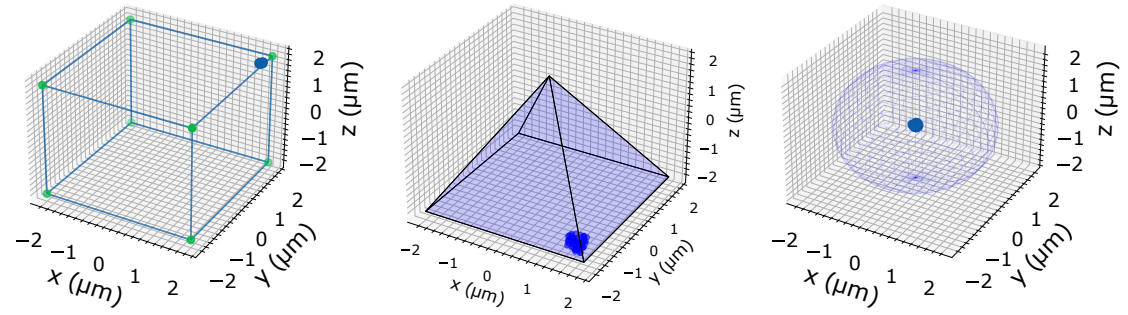

Figure 3.12: Examples of 70 dipoles (blue dots) concentrated within a small region in the different geometries.

Monitors

The results from the simulations in this thesis are obtained from a frequency domain monitor where the electric and magnetic fields are projected to a far-field 1 m from the monitor. This was done to mimic the CL measurements, where the signal is measured in the far field.

Software

The Finite-Difference Time-Domain (FDTD) method was implemented through the ANSYS Lumerical software, versions 2021 R2.5 and 2022 R1.2. The software provides a graphical user interface, a scripting language and objects required for running the simulations. The scripts used in this work are found in Appendix A section 5.3. A combination of the Lumerical scripting language and Python was employed to set up and run the simulation and analyze the results. The code is provided in detail on purpose to make it a bit less burdensome for future students.

3.3.3 Convergence Testing

OOptimized simulation parameters are acquired through convergence testing. Such tests yield the accepted error versus the time and memory requirements. Numerical error in FDTD is mainly because of the size of the mesh cells. Factors such as the boundary condition thickness and size and the size of the monitors also influence the numerical error.

The converged parameters were tested against relevant results such as transmission, yielding a quantitative test, and the far fields, yielding a visual test. The data from both parameters are collected from the same monitor. For simplicity, all convergence tests were done with one dipole source. The simulation region was set up as explained in section 3.3. All the results/figures in this section are from the pyramidal particles. Convergence test results from the two other particles (spherical and cube) are placed in Appendix A section 5.4. Table 3.2 summarizes the results with the related error from all convergence tests done in this work.

Quantifying the level of convergence

The definition of error in convergence testing is not straightforward. However, there are ways to "measure" the error, for example by looking at a change in the results as a convergence step, e.g., the size of the mesh cell. The difference between the result from step i and step $i-1$ for a total of N convergence steps can be quantified as

$$\Delta\sigma(i) = \sqrt{\frac{(\sigma_i - \sigma_{i-1})^2}{\sigma_i^2}} \tag{3.4}$$

where σ_i and σ_{i-1} is the simulation result from one convergence step i and $i-1$. Ideally, $\Delta\sigma(i)$ approaches zero. However, after converging one parameter other errors will dominate and instead, $\Delta\sigma(i)$ approaches some constant.

Lumerical states that by using default settings many of the dominating sources of error disappear. It is quite natural to set the accepted level of error in the simulations equal to or greater than the error expected in physical experiments, such as the cathodoluminescence spectroscopy measurements, which has a resolution of a few nm in optimized conditions (the instrument used in this work - see section 3.2.2). However, a more limiting factor for increased accuracy could be due to memory requirements on the available computers. Hence, there are several factors to take into consideration when deciding the optimal simulation parameters

Boundary condition

The main source of the error caused by the PML is reflections. The signal can re-interfere with the source causing incorrect power normalization or interfering with the scattered fields from the structure. A solution to this problem is to increase the number of layers in the PML. Therefore this parameter, as well as the distance between the structure and the PML, is convergence tested. The mesh accuracy is set to '2' for more efficient tests.

Figure 3.13a shows the far-field results are not influenced by the number of PML layers. There is a change in transmission (Figure 3.13b) between layers 7 - 8 and 8 - 9. However, it is relatively small - approximately 5×10^{-5}. Therefore, the number of PML layers is set to 8 (also recommended by Lumerical).

As expected, the distance from the structure to the PML (Figure 3.13c influences the results, both far fields and transmission. Here, the far-fields are converged after six convergence steps, corresponding to a distance between the PML and the structure of 4.75 - 2 µm = 2.75 µm. Figure 3.13d shows that the transmission is converged with a PML size of 5 and 6 µm (from the origin). This corresponds to a distance of 6 - 2 µm = 3 µm yielding an error of less than 0.05. The distance between the structure and the PML is therefore set to 3 µm.

Monitors

By default, monitors interpolate the fields to certain points, yielding interpolation error. To ensure that the distance and size of the monitor were sufficient both parameters were convergence tested against far fields and transmission. For unknown reasons, the far-field result was empty when running the monitor height test, therefore only the transmission results are available.

Figure 3.14a and 3.14b shows the results from the monitor size test. The far-field is converged between steps 15 and 16, corresponding to a size of 5.29 µm. However, with the influence of memory and computational time, the monitor size is set to the max value to ensure more accurate results. This max value corresponds to the monitor size of 6.2 µm, slightly larger than the inner dimensions of the PML boundary. Doing so also ensures that all data in the simulation region is collected by the monitor.

The result from the monitor height (above the structure) is shown in Figure 3.14c. The transmission does not seem to converge. However, the error increases with increasing height. Therefore the monitor height is set to be as close to the structure as possible, however, at least one mesh point away to have data points to project onto the monitor.

Meshing

To eliminate as much numerical error as possible without introducing new ones, e.g. round off errors due to computing with very small numbers, convergence tests of the mesh were performed. In this work, two separate convergence tests were carried out. Firstly, the mesh accuracy was tested and afterwards the size of the mesh cells within the mesh override region covering the particles and their surfaces was tested.

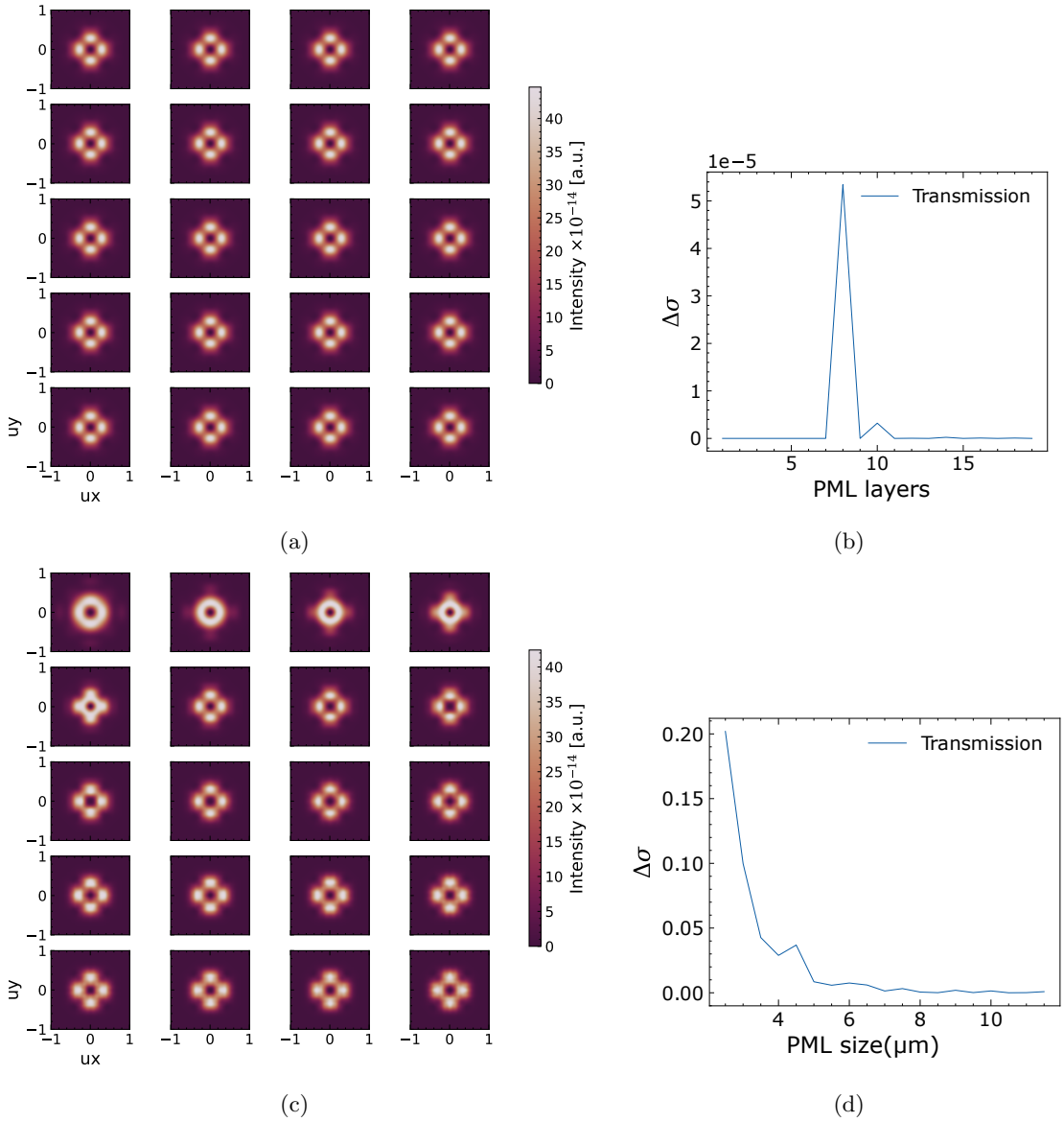

(a) (b)

(c) (d)

Figure 3.13: Convergence tests of a 2 µm pyramid. Far-field (a,c) intensity and transmission (b,d). Run with mesh accuracy 3. (a,b) **number of PML layers** and (b,c) the **distance between the structure and the PML**.

Figure 3.15a shows the results from the mesh override region convergence test. After 16 - 17 steps, corresponding to mesh cells of size 0.018 x 0.018 x 0.018 µm. At *0.018 µm* sized mesh cells, the transmission has an error of approximately 0.25, which is not the best-converged result.

Because of running many simulations, the time consumption of each simulation becomes important. Therefore, for the simulations comparing the number of dipoles and the positioning of many dipoles, a mesh of *0.042 µm* was used. A slightly larger mesh halved the time consumption. The error of the transmission is consequently reduced to 0.1.

The result from the mesh accuracy convergence test is shown in Figure 3.15c and 3.15d for the far-field and transmission respectively. The far-field is considered converged with mesh accuracy 3. However, the transmission error decreases with increasing mesh accuracy. As it is the far-field results which will be studied in the rest of this work, mesh accuracy of *3* is chosen to be sufficient.

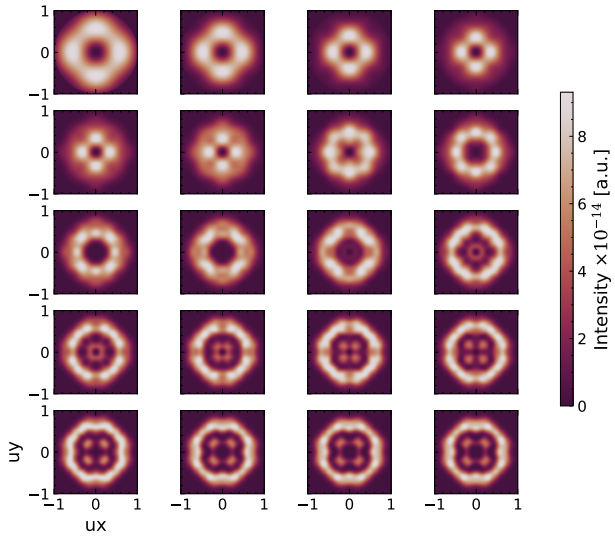

(a)

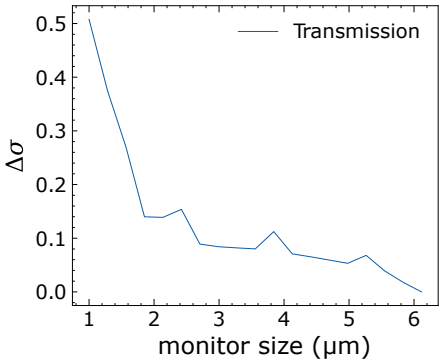

(b)

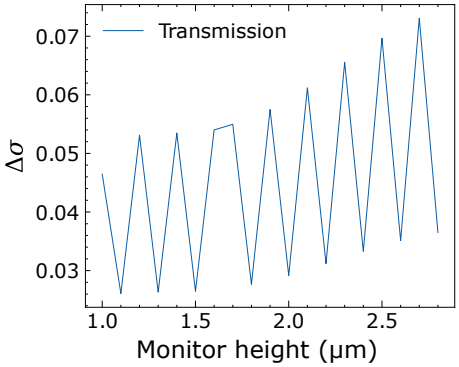

(c)

Figure 3.14: Convergence tests of (a,b) the **monitor size** and (c) **monitor height** of a 2 µm pyramid. Mesh accuracy 3. 6 x 6 x 6 µm sized PML with 8 layers. a) Farfield intensity ($\times 10^{-14}$), (b,c) transmission.

This yields a transmission error of 0.25.

Dipoles

Lastly, we test how many randomly oriented dipoles were sufficient for a converged far-field. The simulations were run with one dipole at a time. Thereafter the fields were summed together and averaged over the total number of dipoles using Equation 3.3. This is done to introduce an incoherent emission environment as described in Section 3.3.2.

The resulting far-field intensity plots from the test of 1-100 dipoles within the pyramid are shown in Figure 3.16. The convergence test from the sphere and cube particles is found in Appendix A, section 5.4. The field changes the most with a few dipoles (1-10). After 30 dipoles, the difference in the field when adding another dipole is significantly less. However, the maximum intensity at this point stabilized. From 30 to 50 dipoles the maximum intensity shifts from ~ 70 to 85×10^{-14}. From 50 - 70 dipoles the difference is $\sim 20 \times 10^{-14}$.

Even though the maximum intensity with 90 and 100 dipoles is both at ($\sim 150 \times 10^{-14}$), the

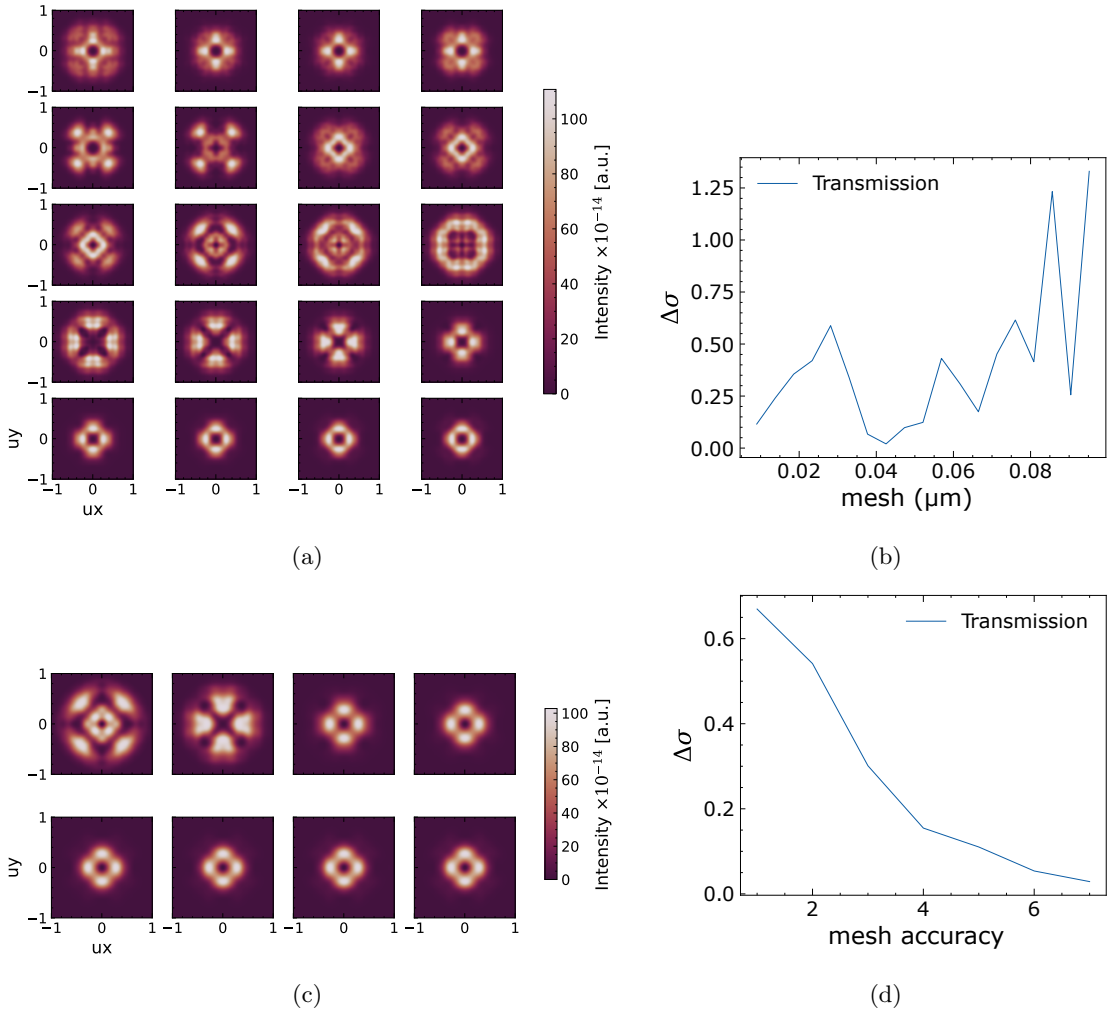

Figure 3.15: Convergence tests of a 4 µm pyramid. Far field intensity ($\times 10^{-14}$). (a) mesh override region of mesh cells of size $0.1 - 0.009$ µm and (b) mesh accuracy 1-8 where the topmost left image has the (a) largest mesh cell (0.1 µm) and (b) lowest mesh accuracy (1). Convergence test of transmission versus c) mesh override region and d) the mesh accuracy.

time-usage of running so many simulations is considered a more negative effect compared to the maximum intensity. Besides, the visual difference is more important, as we will study how the field changes as a function of the dipole positions within the structure.

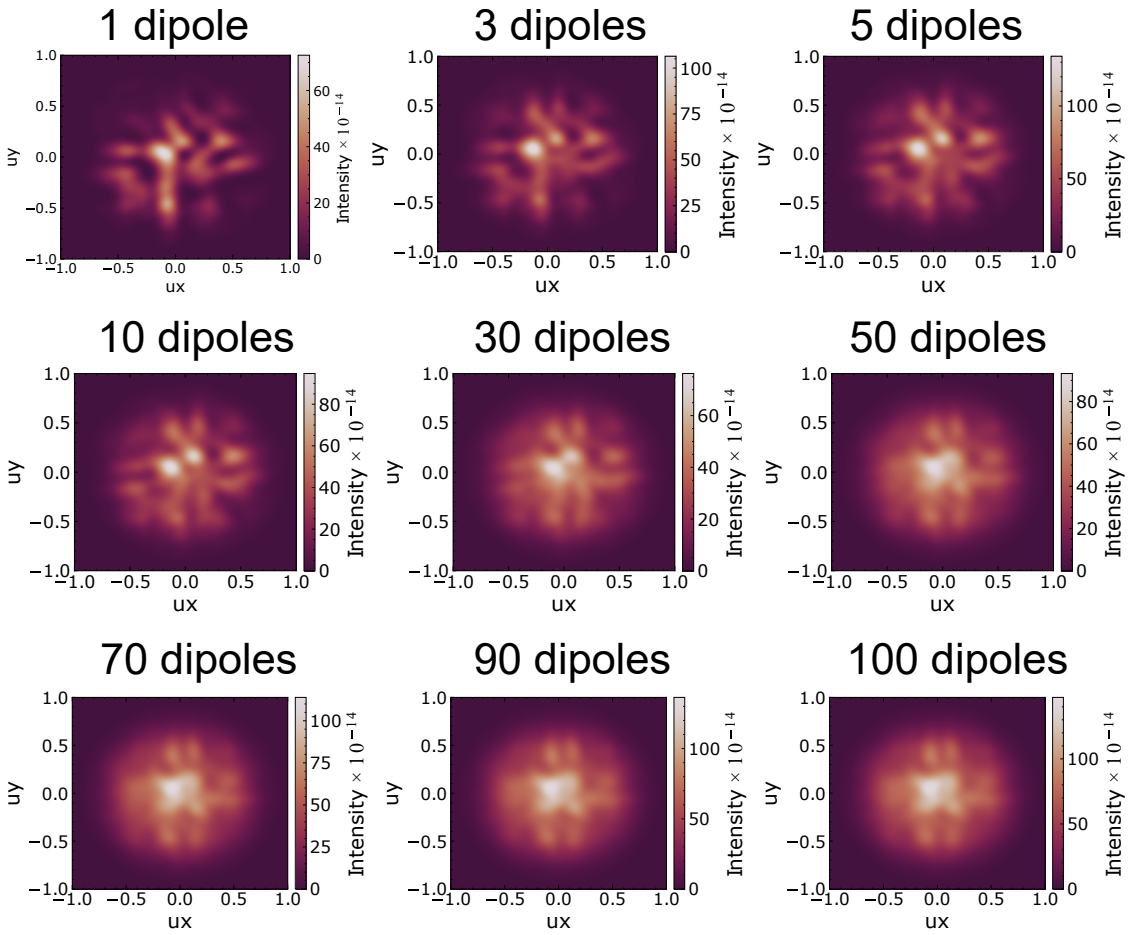

Figure 3.16: Convergence tests of the far-field intensity **number of dipoles** randomized in the structure of a 4 µm pyramid. Mesh accuracy 3. 6 x 6 x 6 µm sized PML with 8 layers.

Table 3.2: Summary of the converged parameters found in the above convergence tests. Also including the parameters from the two other geometries, the spherical particle and the cube/box.

Convergence test	**Result**	$\Delta\sigma_T$
	Pyramid	
PML layers	8	$\sim 5.0 \times 10^{-5}$
PML size(distance from structure)	6 µm	0.15
Monitor size	PML size + 0.2 µm	< 0.01
Mesh accuracy	3	0.25
Mesh	0.018 µm	0.25
Monitor height	1 mesh cell	-
Dipoles	70	-
	Sphere	
PML layers	8	$\sim 1.0 \times 10^{-4}$
PML size(distance from structure)	6.7 µm	0.03
Monitor size	PML size + 0.2 µm	0.10
Mesh accuracy	3	0.03
Mesh	0.07 µm	0.05
Monitor height	1 mesh cell	-
Dipoles	70	-
	Cube/box	
PML layers	8	$\sim 9.0 \times 10^{-6}$
PML size (distance from structure)	6 µm	0.04
Monitor size	PML size + 0.2 µm	< 0.05
Mesh accuracy	3	< 0.01
Mesh	0.043 µm	< 0.01
Monitor height	1 mesh cell	-
Dipoles	70	-

Chapter 4

Results and Discussion

This chapter is devoted to the results obtained in this work. Herein, a detailed study of many particles within two samples is given. The samples were irradiated with 1.8 MeV protons to a dose of 10^{14} cm^{-2} and annealed at 300° C and 1000° C. The chapter will focus on this irradiation dose and present the results in detail, as the Si vacancy related ZPLs in the cathodoluminescence spectra for the samples irradiated with lower doses were challenging to detect. Spectra from the 0E0-RT sample are given in an annealing series for comparison. See table 3.1 for a full overview of the samples and an explanation of the sample notation.

For convenience, a labelling system for the luminescence peaks is introduced. It follows the alphabet where the highest energy feature in cathodoluminescence (CL) starts with *A*. Lines or features near each other (tens of nm) are grouped by the same letter but are separated by a number. As features in photoluminescence (PL) are significantly sharper than CL, CL and PL labels are separated. The marking of ZPLs from the PL ZPLs starts with the letter *J*. The reader should be aware that this labelling system is independent of the "common" naming of emission centres often used in literature, such as the CAV defect in 4H-SiC, referred to as A and B lines, and the silicon-vacancy in SiC which is commonly named V-lines. CL and PL peaks are labelled by their highest intensity position. As extensive analysis of the peaks, such as Gaussian peak fitting, is out of the scope of this work, a feature is considered a peak if it stands out from the background. Hence, some labelled peaks could originate from a phonon sideband, noise or interference pattern.

Firstly an overview of the powder is given as an introduction. An initial assessment is given using SEM images and CL spectra of the band edges. We then discuss the samples in terms of the composition of elements using EDS and defect-related ZPLs before and after irradiation using PL. Thereafter, the luminescence from the individual particles is examined using CL to better understand the present colour centres and how the emission is influenced by factors such as annealing temperature, irradiation dose and particle geometry. Lastly, we compare the findings to numerical calculations to provide a theoretical perspective of the emission from the SiC particles.

Sample preparation, measurements and labelling of peaks in the samples studied with photoluminescence spectroscopy were performed by Dr Augustinas Galeckas.

4.1 Introduction to the Silicon Carbide Particles

This section presents an overview of the powder through Secondary Electron Diffraction (SED) images. The composition of the elements in the SiC powder and Si wafer were validated using Energy-Dispersive X-Ray Spectroscopy (EDS). Lastly, obtained CL spectra from CL spectroscopy measurements in the energy range of $\sim 1.5 - 4.3$ eV (300-800 nm) from four selected particles in the 1E14-300C and 1E14-1000C samples, are presented. These spectra are selected to show how the 4H, 6H, 3C and 15R-SiC polytypes were identified in this work.

Figure 4.1a illustrates the distribution of the powder, observed as bright shapes, on the otherwise darker silicon wafer. Figure 4.1b illustrates the presence of smaller particles, seen as brighter flakes and dots, present on top of a larger particle and the silicon substrate. The average size of the particles is measured to ~ 4 µm but ranges from hundreds of nm to ~ 10 µm. Particles of familiar geometrical shapes are shown in Figure 4.2. Figure 4.2a represents a round shape, whereas Figure 4.2b and 4.2c are considered as pyramidal (tip pointing out of the paper plane) and cubic/rectangle, respectively. However, most particles have a more arbitrary shape.

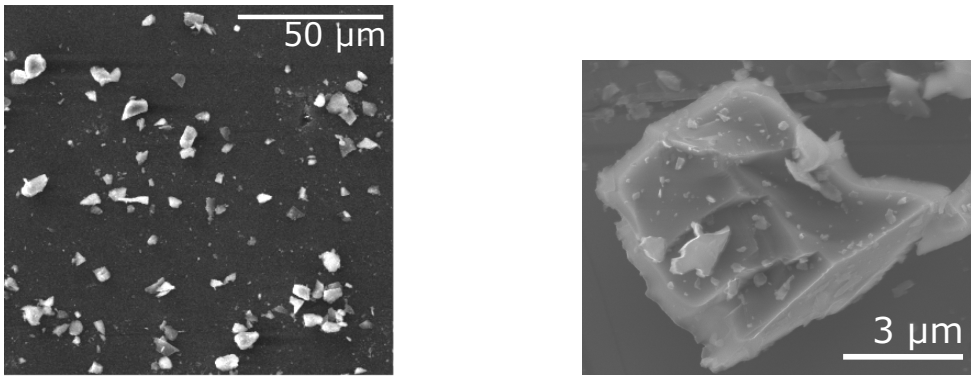

(a) (b)

Figure 4.1: SED micrograph of (a) evenly distributed SiC powder in a Si substrate and (b) SiC particle with 'dust'. Obtained with (a) 23 kV and (b) 10 kV. Probe current measurements were unfortunately not done.

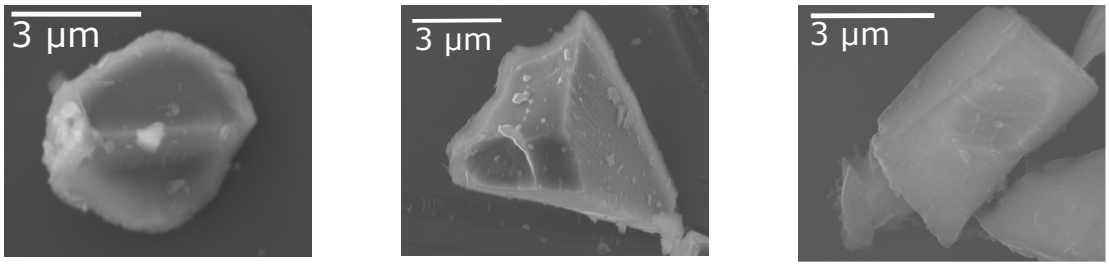

(a) Spherical/rounded (b) Pyramid/triangle (c) Cubic

Figure 4.2: SED micrograph of individual SiC grains with a variety of distinct shapes. Obtained with (a,b) 10 kV and (c) 23 kV acceleration voltage. Probe current measurements were herein not done

The EDS analysis presented in Figure 4.3 shows the elemental analysis of position (1), a brighter particle, and position (2), the surface of which the particle is on top. Figure 4.3a shows an SEM micrograph with the analyzed positions marked. The obtained atom percentage from each element

acquired from the two positions is given in the table in Figure 4.3b. The EDS spectrum revealing the counted x-rays as a function of energy (keV) is shown in Figure 4.3c. Each peak originates from the K-shell in one element within the sample, and an algorithm suggests the origin of each peak by labelling the respective peak.

The analysis confirms the presence of Si and C with approximately 50% of each element within the particle. The surroundings of the particle only reveal the Si substrate. Based on the theoretical atomic configuration of SiC and Si, we anticipated this distribution. The error in the quantification is an order of magnitude higher than desired. However, a short acquisition time may have affected the results. Note also that quantifying lighter elements with EDS is challenging. Lighter elements produce longer wavelengths which are more prone to be absorbed again in the surrounding material. Following the conversation with the instrument responsible, it became clear that there is always a presence of carbon $(3-5\%)$ in the EDS spectra. In the region close to the C peak, see in Figure 4.3c, there is substantial noise. The Si + Si Sum peak seen in Figure 4.3c position 2 is likely due to the sensor measuring two X-rays from Si simultaneously. The sensor ideally measures one photon at a time. The result is satisfactory to demonstrate the elements in the powder.

a)

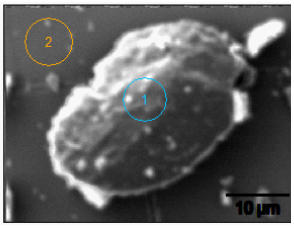

b)

Element (Line type)	Atom %
Position 1	
C (K)	49.2 ± 1.3
Si (K)	50.8 ± 0.9
Position 2	
O (K)	1.4 ± 0.4
Si (K)	98.6 ± 1.6

c)

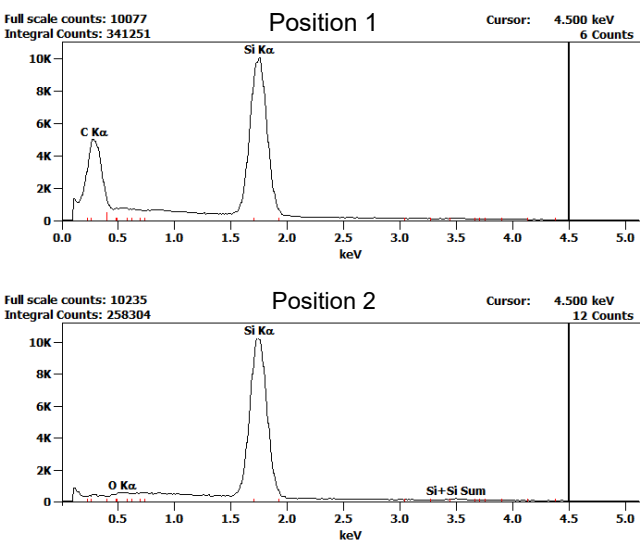

Figure 4.3: Results from EDS measurements. (a) SEM micrograph with marked areas where the EDS measurements were done, on a particle (position 1) and from the substrate (position 2). (b) Table with elements found with atomic % from each atomic element with the given atomic % error. (c) EDS spectrum from area (top) 1 and (bottom) 2 in (a) . The EDS results were obtained with 5 keV, 30 % downtime and a working distance of 8.5 mm.

Polytypes

In [46], Vásquez and Bathen et al. studied the same type of powder as investigated herein and established that one particle contains only one polytype. Moreover, they present a method, verified with Raman spectroscopy, to analyze the polytype of the studied SiC-particle. Plotting band edge emission intensity as a function of energy, rather than the wavelength, the polytype is identified by comparing the band edge energy to known experimental values. Polytype identification is also possible by studying the sharp emission peaks in cathodoluminescence, often referred to as Zero Phonon Lines (ZPL), of the silicon vacancy. The positions of these emission peaks are well

established for the 3C, 4H, 6H and 15R polytypes in the literature. The ZPLs from amongst others, the silicon-vacancy, are listed in Table 2.2.

Figure 4.4a shows a CL spectrum, intensity as a function of energy, from each of the selected polytype particles, shown in the SEM micrograph in Figure 4.4b. The excitonic energy gaps and the position of the maximum intensity of the respective peak are labelled for the respective polytype. Note that the intensity of each spectrum is shifted to where the maximum intensity of each spectrum aligns.

Each polytype is identified by the bandgap emission from the respective particle as the sharp intensity increase close to the labelled excitonic energy gap. The width of the peak is believed to originate from the phonon interaction required for band-to-band recombination in an indirect semiconductor. Moreover, the relative energy of the band-edge emission is compared between spectra. Through the analysis, particles of the 3C-, 6H-, 15R- and 4H-SiC polytypes were identified with their respective peak positions at 2.0, 2.6, 2.7 and 3.0 eV as in [46].

Information from the manufacturer states that the powder is 80% 6H-SiC polytype. The remaining 20% is expected to be mainly the polytypes 3C, 15R and 4H. Therefore throughout this thesis, 6H-SiC is the discussed polytype unless otherwise specified.

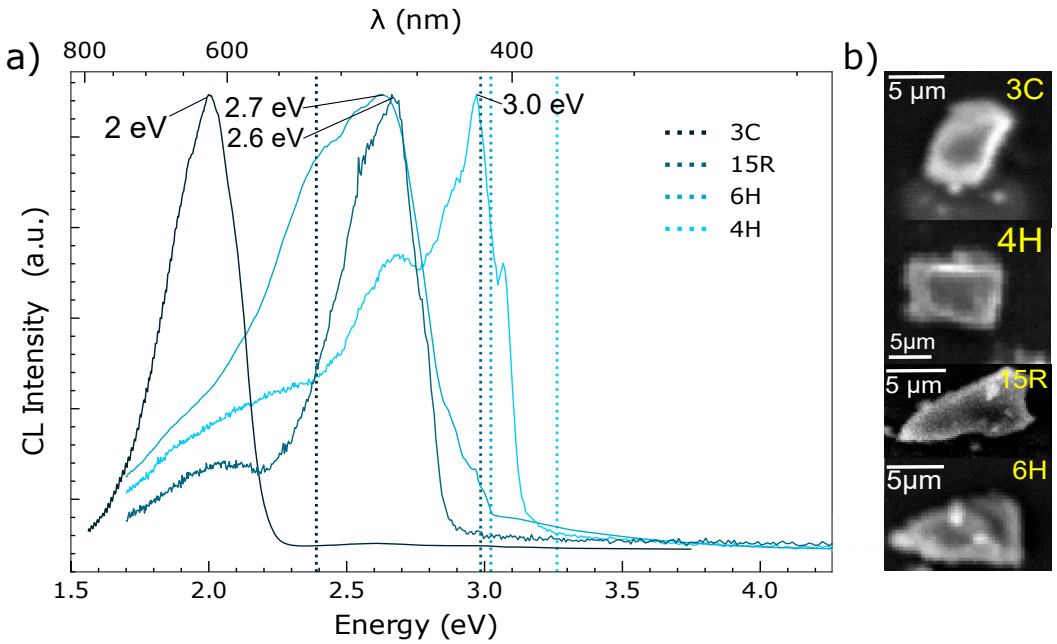

Figure 4.4: (a) CL spectra measured with a 10 keV electron beam at 80 K from particles in the SEM micrographs in (b). The intensities in the spectra are shifted in intensity to enhance the band-edge CL from the polytypes relative to each other. The bandgap energy from the respective polytype is marked with vertical lines. The energy of the maximum intensity of each spectrum is also provided.

4.2 Photoluminescence Spectroscopy

Studying samples with photoluminescence spectroscopy gives an overview of the present colour centres in the SiC *powder*. As the PL setup operates at lower temperatures, sharper features are also displayed. One sample was examined 'as received', and the other was irradiated with 8×10^{13} cm^{-2} 1.8 MeV protons and subsequently annealed at 300° C for 30 min in air. The particles with an average of 4 µm in size were excited with a laser of energy of 3.815 eV (324.9 nm) at 10 K. Note that the beam size and collection area were large compared to the particles. Therefore many particles were measured simultaneously, and the measurements were considered powder measurements.

We will discuss the sharp emission lines and intensities in the as-received and irradiated samples in the range of $\sim 1.1 - 1.45$ eV (850-1100 nm), shown in Figure 4.5a and 4.5b, respectively. To enhance the sharp peaks both spectra are background-subtracted. The inset in the figures shows the original spectrum. In the spectra, several sharp peaks are observed against a relatively flat background. Such peaks, in the energy range below the bandgap, are often related to zero phonon lines (ZPLs) potentially originating from transitions from two-level systems relevant in quantum technology. Hence, highly relevant for the present work. For simplicity, we herein refer to the sharp peaks as ZPLs. Keep in mind that observed ZPL *can* originate from PSBs.

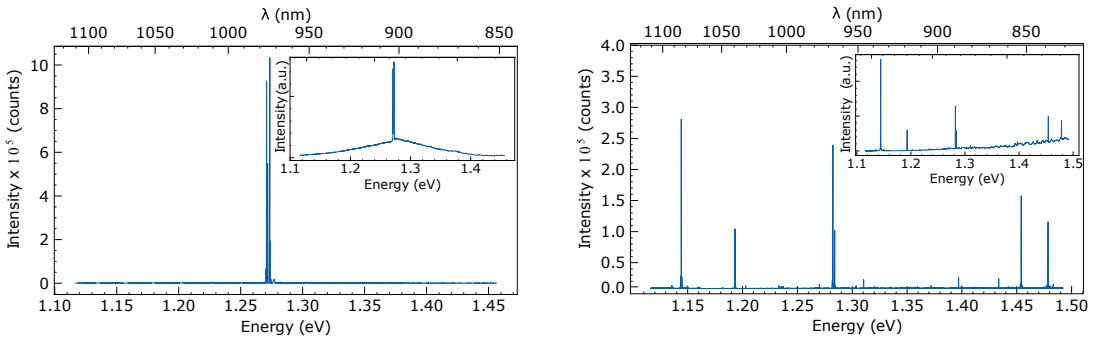

(a) (b)

Figure 4.5: PL spectra of (a) as-received and (b) irradiated SiC powder. The baseline is subtracted, and the insert shows the raw spectra.

Four polytypes with several equivalent lattice sites result in spectra with about 50 distinct ZPLs. In the event of two photons reaching the detector simultaneously, a ZPL can appear at the double wavelength of a single photon. The discussion is therefore limited to the most pronounced ZPLs, with a threshold for being considered set to an intensity of 5×10^4 counts. Defects exhibiting an emission above this threshold are marked with a (*) in Table 4.1. The ZPLs below this threshold are considered beyond the scope of this work. Discussions of the silicon-vacancy are included because of its many ZPLs from the different polytypes. Here it should be noted that bright colour centres relevant for quantum technology should ideally have emission intensities surpassing 1×10^6 counts/s [15].

Considering first the as-received sample, Figure 4.6 displays high-resolution PL spectra of as-received (left panels) and irradiated (right panels) samples divided into wavelength regions of ~ 60 nm. In some energy regions, it was difficult to distinguish emission lines from noise in the as-received sample, making it difficult to identify lines.

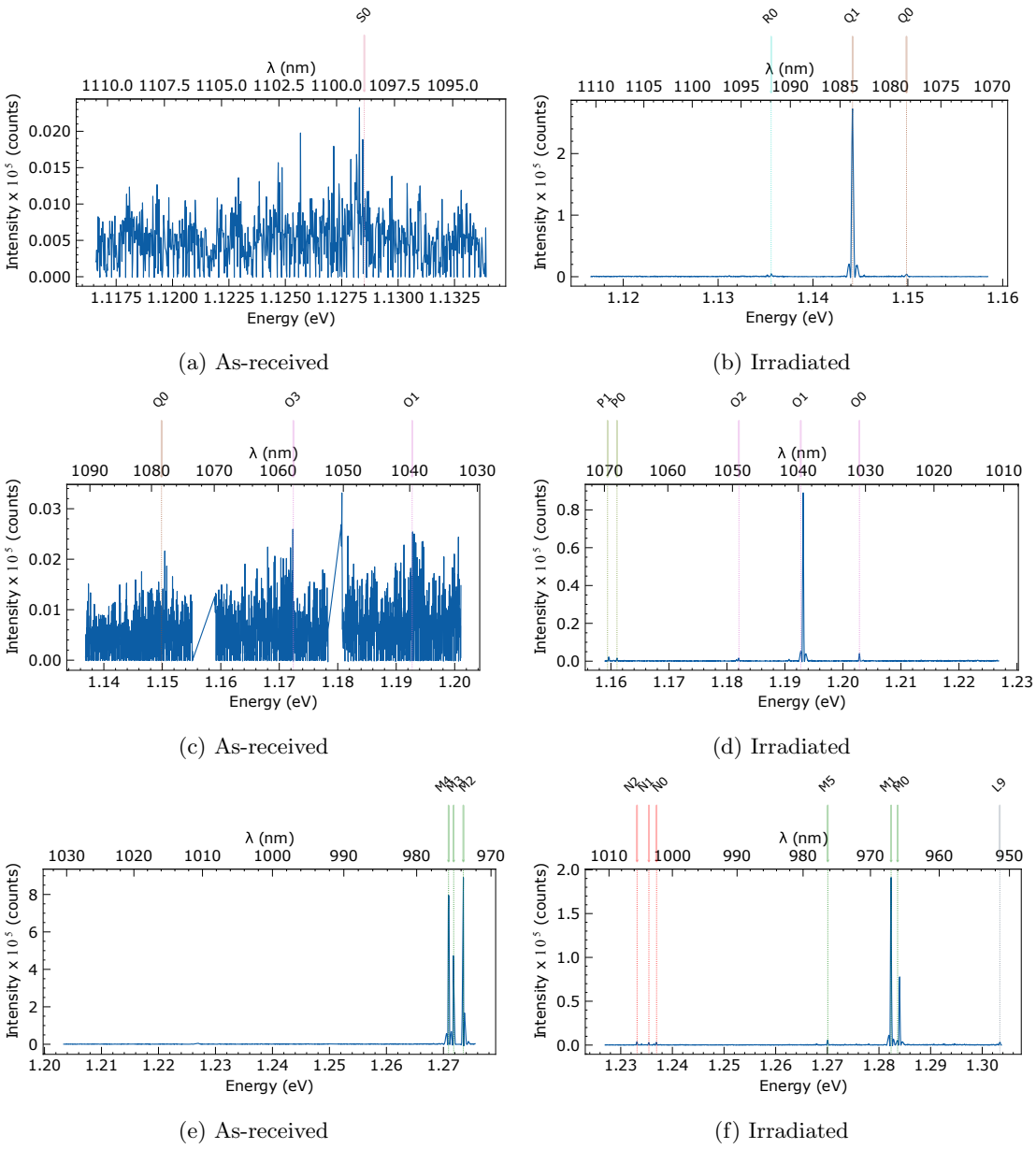

(a) As-received (b) Irradiated

(c) As-received (d) Irradiated

(e) As-received (f) Irradiated

Figure 4.6: PL spectra from the (left column) as-received and (right column) irradiated powder (Figure 4.5b and 4.5a in more detail). All the peaks considered to originate from colour centres marked with vertical dashed lines with respective IDs are explained in the opening of this chapter. (continues)

The highest intensity ZPLs in the as-received sample are the prominent lines in Figure 4.5a. The same features can be seen in Figure 4.6e, labelled as M4 at 1.271 eV (975.7 nm), M3 at 1.272 eV (975.0 nm) and M2 at 1.274 eV (973.7 nm). These emission centres are, to date, not identified and are therefore of interest. Due to the sharp nature of the ZPLs, these centres should be investigated for possible single-photon emission behaviour. Impurities, for example from the raw materials used to produce the SiC powder or in the process of making the powder, may be suspected for high-intensity ZPLs in a non-irradiated SiC sample, and are thus potential candidates for the origin of the M2, M3 and M4 - ZPLs.

The known and well-established silicon-vacancy (V_{Si}) is in the as-received sample present from 4H and possibly 15R (labelled as K and J lines in Figure 4.6g and 4.6i). The J4-line at 1.44 eV (861.1

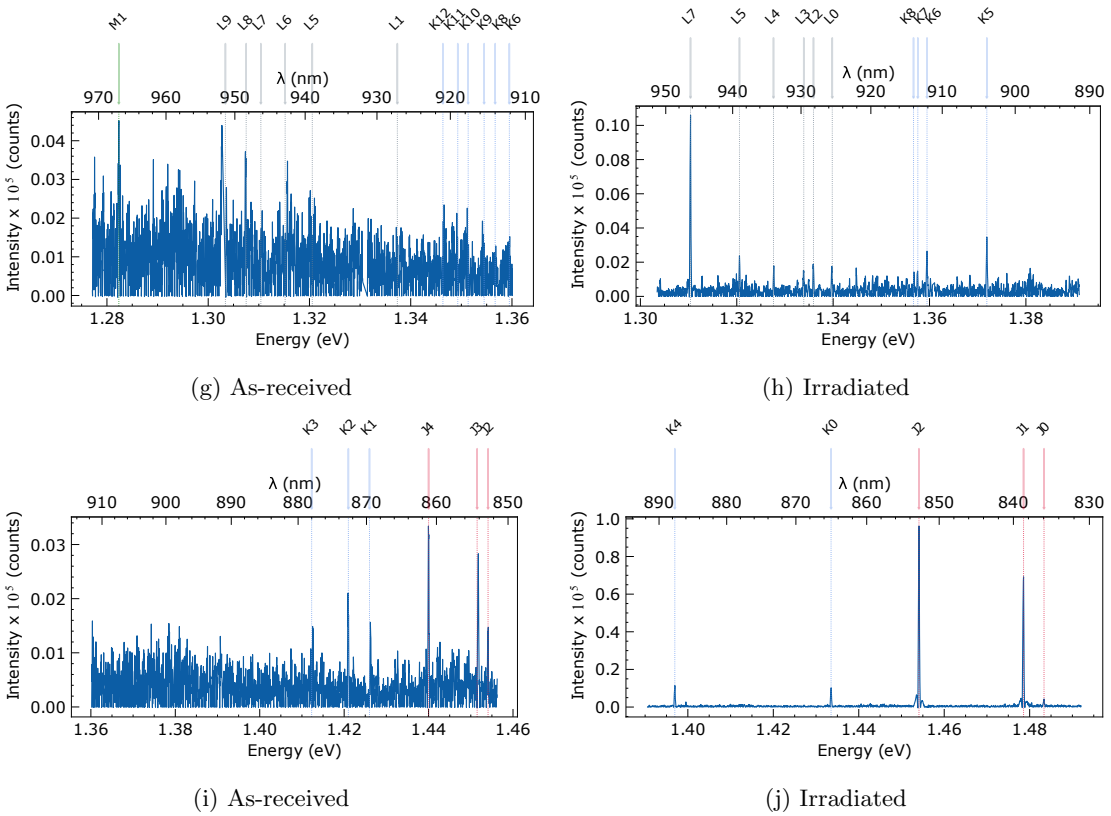

(g) As-received (h) Irradiated

(i) As-received (j) Irradiated

Figure 4.6: (continued) PL spectra from the (left column) as-received and (right column) irradiated powder (Figure 4.5b and 4.5a in more detail). All the peaks considered to originate from colour centres marked with vertical dashed lines with respective IDs are explained in the opening of this chapter.

nm) is in good agreement with the V1 ZPL at 1.439 eV (861.4 nm) in 4H-SiC. The K10-line at 1.351 eV (917.6 nm) is close to the V2 centre in 4H-SiC and the V4 centre in 15R-SiC, both located at 1.352 eV (917 nm). Observing the silicon-vacancy in the as-received material is not common, at least not in wafers. Intrinsic defects may arise from the conditions during the mechanical crushing of crudes to powder.

After proton irradiation of dose 8×10^{13} cm^{-2} and annealing at 300° C, the number of visible ZPLs increases and the overall intensity of the peaks decrease. This observation is most evident in Figure 4.5b, but can also be seen in the right panels in Figure 4.6. Even though several new lines appear after irradiation and annealing, the emission from certain defects was observed quenched. The irradiation is expected to mainly form intrinsic defects, even though migration and subsequent complex formation with extrinsic defects cannot be excluded. Thus, as a first approximation, the difference in ZPLs in the PL spectra between the as-received and irradiated samples should be intrinsic defects. The overall decrease in intensity in the irradiated and annealed sample could be explained by the higher concentration of intrinsic defects possibly increasing non-radiative channels.

Of all the M-lines, only the M1 line at 1.282 eV (973.7 nm) is observed in both samples (irradiated in Figure 4.6f and as-received in Figure 4.6g). The intensity of the M1 peak increases from $\sim 0.045 \times 10^5$ to $\sim 2 \times 10^5$ counts after the irradiation and annealing. The M0 and M5 lines in Figure 4.6f appear after the sample treatment procedure and are not observed in the as-received sample. The emission from the lower energy M2, M3 and M4-lines is quenched after the proton

irradiation, clearly seen by the difference in Figures 4.6e and 4.6f.

The observations of the M-lines could indicate that these originate from two different defect centres. The origin of the M0, M1 and M5 lines, within increased intensity after the sample treatment, could be intrinsic as the irradiation and annealing are expected to increase the number of intrinsic defects. As the M2, M3 and M4 are not observed in the irradiated and annealed sample, the previously stated argument, regarding the extrinsic origin of these lines, is strengthened. The quenched emission of the M2-4 lines could also be because of increased recombination from the higher concentration of intrinsic defects in the irradiated sample. As a consequence, the emission efficiency of the M2-4 lines could then decrease. However, then the emission efficiency, and therefore the ZPL intensity, of other defects would also decrease, which is not observed. A maybe more likely explanation is if the M2-M4 lines were to be precursors for other defects. Precursors are defects which have migrated and reacted with other defects and thereby dissociated or evolved into a different kind of defect. However, as the SiC particles were annealed at 300° C, a relativity low temperature, the formation of defect complexes is, to a large extent, not expected.

The origin of neither the M0, M1 and M5 lines, nor the M2, M3 and M4 lines are identified by comparison with known features in literature. The observations in this work regarding intensity increase and decrease from groups of lines could indicate the groups [M0, M1 and M5] and [M2, M3 and M4] originate from one emission centre each, which coincidentally overlaps in the same energy range. Both groups could also originate from an already known defect (intrinsic or extrinsic), but sit in the lattice of a different polytype which would alter the energy of the ZPLs.

In the irradiated sample, the K0 and K4 lines appear at 1.433 eV (865.0 nm) and 1.397 eV (887.6 nm), respectively, as seen in Figure 4.6j. These are in good agreement with the V1 (865 nm) and V2 (887 nm) ZPLs from V_{Si} in the 6H-SiC polytype. The V3 line from V_{Si} is expected to be observed between 1.134-1.367 eV ($906 - 907$ nm). One of the two lines between K5 and K6 in Figure 4.6h, almost indistinguishable from noise, could identify as the last V_{Si} ZPL in 6H-SiC. Higher-resolution PL measurements in the energy range of the V_{Si} from the 6H-polytype are needed to potentially clarify the presence of the ZPL in the powder. Luminescence from K4 in the irradiated sample, seen in Figure 4.6j, could fit with the 1.399 eV (886.5 nm) line (V2 in 15R), but V2 from 6H-SiC is in better agreement. The K5 and K10 lines in Figure 4.6h and 4.6g, respectively, are in good agreement with the known V3 and V4 in 15R, but K10 is also matched with the ZPLs from 4H (see Table 4.1). V_{Si} luminescence from 3C (1.100 - 1.121 eV) is out of the energy range of the PL measurements in this work.

The Q1 - line at 1.149 eV (1078 nm) in Figure 4.6b, one of the higher intensity ZPLs in the irradiated sample, has a yet unidentified origin. The energy (wavelength) is not far from the neutral divacancy, $V_C V_{Si}^0$, in 4H-SiC, reported at 1.090-1.150 eV ($1078 - 1132$ nm). At 1.193 eV (1039.6 nm) a high-intensity line, labelled O1, emerges in the irradiated sample, seen in Figure 4.6d. We have indicated that the O1 line might originate from the PL5, PL6 or the divacancy in 4H. However, the agreement is not perfect.

In the higher energy range in Figure 4.6j, the J1 and J2 lines appear at 1.478 eV (838.6 nm) and 1.351 eV (852.8 nm), respectively. The former is only observed in the irradiated sample. The $Nb_{Si}V_C^0$, reported in the range of $1.384 - 1.508$ eV ($882 - 896$ nm), covers both J1 and J2 lines. However, even though the concentration of Nb is decent, the probability of V_C migration is low

below $\sim 1600^\circ$ C. A more certain identification of the Q1, O1, J1 and J2 lines would require further work. Other lines in agreement with reported ZPLs in literature (listed in Table 2.2) are mentioned in Table 4.1.

Table 4.1: Summary of observed PL ZPLs in the *as-received* and proton *irradiated* samples in order of descending energies (ascending wavelengths). The respective sample is marked (check mark) if the color line is found therein. The labeling system is explained in the introduction to the chapter. The respective ZPL reported in literature are found listed in Table 2.2.

ID	**E (meV)**	**λ (nm)**	*As-received*	*Irradiated*	**Ref.**
S0	1128.5	1098.8	✓		
R0	1135.6	1091.9		✓	$V_C V_{Si}^0$(6H-SiC) (1093 nm)
Q1*	1144.2	1083.8		✓	
Q0	1149.9	1078.4	✓	✓	$V_C V_{Si}$ (4H-SiC)
P1	1159.4	1069.5		✓	Cr^{4+} (4H-SiC)
P0	1161.1	1068.0		✓	Cr^{4+} (4H-SiC)
O3	1172.4	1057.7	✓		
O2	1182.1	1049.0		✓	Cr^{4+} (6H-SiC)
O1*	1192.7	1039.6	✓	✓	PL5, PL6 (4H-SiC - 1041.9, 1037.9 nm) or $V_C V_{Si}^0$ (4H-SiC - 1037-1047 nm)
O0	1202.8	1030.9		✓	
N3	1223.5	1013.5		✓	
N2	1233.2	1005.5		✓	
N1	1235.6	1003.7		✓	
N0	1236.9	1002.5		✓	
M5*	1270.1	976.3		✓	
M4*	1270.9	975.7	✓		
M3*	1271.8	975.0	✓		
M2*	1273.5	973.7	✓		
M1*	1282.4	967.0	✓	✓	
M0*	1283.6	966.0		✓	
L9	1303.4	951.4	✓	✓	
L8	1307.5	948.4	✓		
L7	1310.4	946.3	✓	✓	
L6	1315.2	942.8	✓		
L5	1320.6	939.0	✓	✓	
L4	1327.6	934.0		✓	
L3	1333.9	929.6		✓	
L1	1337.4	927.2	✓		
L0	1339.8	925.5		✓	

ID	E (meV)	λ (nm)	*As-received*	*Irradiated*	Ref.
K12	1346.4	921.0	✓		
K11	1349.3	919.0	✓		
K10	1351.4	917.6	✓		V2 (4H-SiC), V4 (15R-SiC)
K9	1354.5	915.5	✓		UD3 unknown (4H-SiC)
K8	1356.7	914.0	✓	✓	
K7	1357.6	913.4		✓	
K6	1359.5	912.1	✓	✓	
K5	1371.9	903.9		✓	V3 (15R-SiC)
K4	1397.0	887.6		✓	V2 (6H-SiC), V2 *(15R-SiC 886.5 nm)*
K3	1412.3	878.0	✓		
K2	1421.0	872.6	✓		
K1	1426.0	869.6	✓		
K0	1433.5	865.0		✓	V1 (6H-SiC)
J4	1440.0	861.1	✓		V1 (4H-SiC)
J3	1451.5	854.3	✓		
J2*	1454.1	852.8	✓	✓	
J1*	1478.6	838.6		✓	
J0	1483.4	835.9		✓	

4.3 Cathodoluminescence Spectroscopy

Here we present the results from CL spectroscopy from individual 6H-SiC particles from the three samples in Table 3.1. The specifications of the samples are in Table 3.1. Several spectra with a wide selection of luminescence features in the range of $\sim 0.7 - 3$ eV (400-1700 nm) revealed several features from a variety of defects. With the 1E14-300C and 1E14-1000C samples we try to map the present features in the given energy (wavelength) range and understand their origin and how the particle geometries affect the luminescence.

To detect CL in the near-infrared (NIR) wavelength region, instrument optics were swapped from UV to IR. Unfortunately, the latter has a much lower signal-to-noise ratio. Spectra obtained with IR optics were background subtracted (subtracted spectra measured in the following section with zero probing currents) to enhance the features. In Appendix B, section 5.5, three examples of background subtraction are provided. In the spectra where we want to enhance particular features an offset is added to the intensity.

First, we present an overview of the present CL features in specific particles and compare them with the PL results in the UV region. Thereafter the same is done for the IR region, but not compared to PL as the energy (wavelength) is beyond that of the PL measurements in this work. Next, a study of the different samples is given by comparing features in the annealed and irradiated samples. Then we look further into the behaviour of selected defects, including the silicon-vacancy, in different particle geometries and positions within a single particle to understand how the geometry affects the emission. Lastly, we compare the luminescence from CL to numerical electrodynamics simulations

to see if this can give a better insight into the understanding of the emission pattern in the physical particles.

4.3.1 Overview and Comparison with PL

Studying samples with cathodoluminescence spectroscopy can reveal optically active colour centres in *individual particles*, or even the distribution within a particle. We here give an overview of the many luminescence peaks and will go into more detail. The spectra in this section are selected based on their distinct features from specific particles. Other studied particles exhibit the same characteristics but with different intensities, and are therefore excluded in the following presentation. To compare with PL, the sample studied herein is the 1E14-300C. The sample studied with PL was annealed in air and 1E14-300C in nitrogen gas flow.

The selected spectra are in Figures 4.7 - 4.12 below, starting in the higher energy range. Table 4.2 summarizes the observed ZPLs arranged after the previously mentioned labelling system where the decreasing energy CL peaks are labelled A0-H0 (PL peaks are labelled from J-S). The table includes a column with the peaks discovered in PL. Emission centres published in the literature are found in Table 2.2.

The number of peaks in CL is significantly less than in the PL spectra, described in section 4.2. The reduced number of distinct ZPLs is related to the higher temperature when measuring, 80 K for CL while 10 K for PL in this work, resulting in more contributions from phonon-assisted transitions, widening each peak. This also results in overlapping of the phonon sidebands, which eventually can hide lower intensity peaks. The only feature observed with strong ZPLs in this work in CL is the silicon-vacancy.

Starting in the $1.4 - 2.4$ eV ($500 - 900$ nm) range, two spectra are presented in Figure 4.7. Therein, three main features are labelled as A0 at 2.208 eV (561.6 nm), A2 at 2.030 eV (610.8 nm) and A5 at 1.910 eV (649.2 nm) are observed. The A5 peak could fit with the CAV (antisite) defect in 4H-SiC which has ZPL in the range of 1.832- 1.911 eV (648.5 - 676.4 nm). However, the particles are confirmed to be 6H-SiC through band-edge measurements. Other candidates are the D and D*-centers and HS2 hole trap in 6H-SiC which exhibits PL at 2.10 - 2.14 eV (580 - 590 nm) and 1.89-1.91 eV (649 - 656 nm), respectively [47] Notice that Wei, Tarekegne and Ou in ref. [47] point out that there is still a disagreement amongst several scientists regarding energies (wavelengths) and the origin of the D-centers.

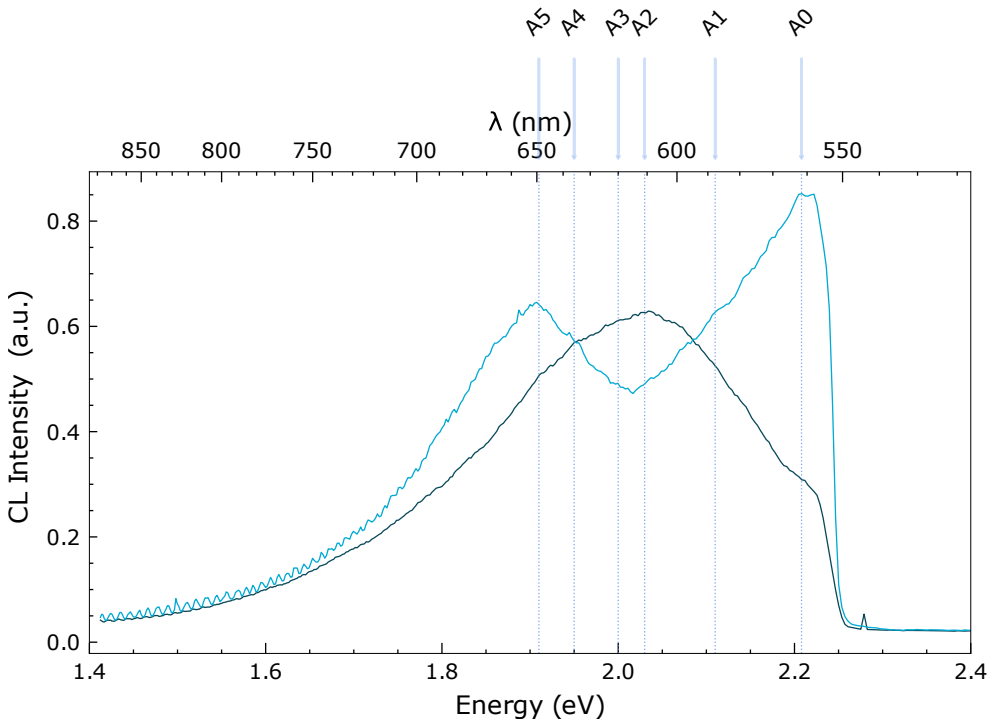

Figure 4.7: Labelled CL spectra from *two individual* particles in the **1E14-300C** sample was measured with a 10 keV at 80 K. The relative intensities of the individual contributions to the spectrum are shifted to highlight the present features The sudden decrease in intensity at 2.3 eV is caused by an applied 500 nm filter.

The higher intensity, light blue spectrum in Figure 4.8a exhibits narrow emission lines labelled B3, B4 and B5, and an interference pattern throughout the spectra. The labelled lines are attributed to the V_{Si} in 6H-SiC. The signal peaks at 1.433 eV (865.1 nm), 1.397 eV (887.6 nm) and 1.369 eV (905.8 nm) and are in good agreement with the reported V1 (865 nm) and V2 (887 nm) centres in 6H-SiC. V3 in the same polytype is reported at 1.368 eV (906-907 nm) (see Table 2.2). The B5 peak, assigned to the V_{Si} V3 centre, was observed at slightly lower energy than the reported value, which might be because of a partially overlapping phonon-assisted sideband from B3 and or B4, assigned to the V2 and V1 peak, respectively. Before comparing to PL results, the B6, B7, and C0 lines seem to be from the interference pattern present throughout the whole energy range. However, they align surprisingly well with lines identified in PL (K6, K11 and L4 lines in Table 4.1). It could be a coincidence or an actual signal. C2 and C4 are also such peaks, they are believed to originate from sole interference as the lines were not observed in the PL spectra.

The B0 (1.543 eV), B1 (1.494 eV) and B2 (1.442 eV) lines in the lower, black spectrum Figure 4.8a are features not identified in the literature to date. These were only observed in the 1E14 - 300C sample and very few particles. Their origin could therefore be extrinsic, as they diminish in the higher annealed sample. However, B0, B1 and B2 features were in this work not observed in the 0E0-RT (as-received) sample. Hence, an intrinsic origin should not be excluded. Note that the intensity from the silicon vacancy here is lower than the B-features and only the PSB is visible. The B2 line, however, is approximately 1 nm off the 858.7 nm ZPL V_{Si} line in 4H, which simply could be because of a shift in calibration. The peak is also a bit wider on the top, compared to e.g the ZPL in the other spectrum in the same figure. This observation could indicate that the B2 feature has two overlapping contributions. In this case, the polytype verification is uncertain as we

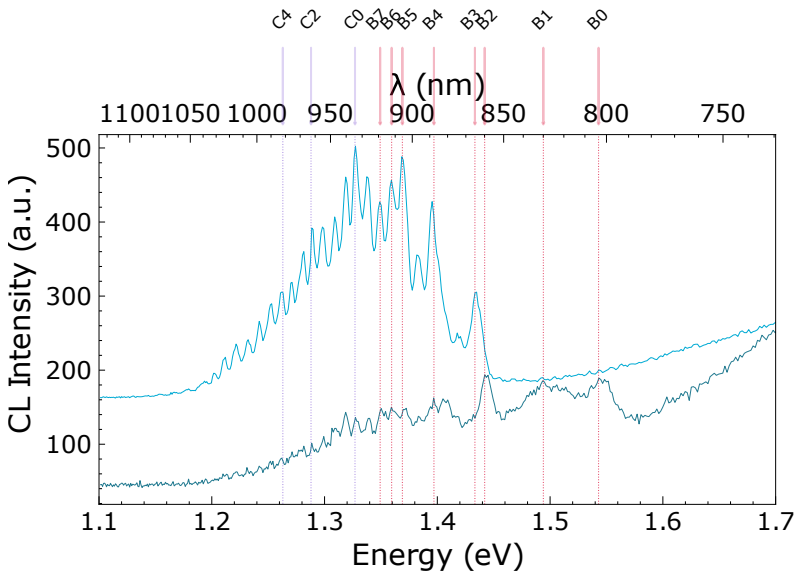

(a)

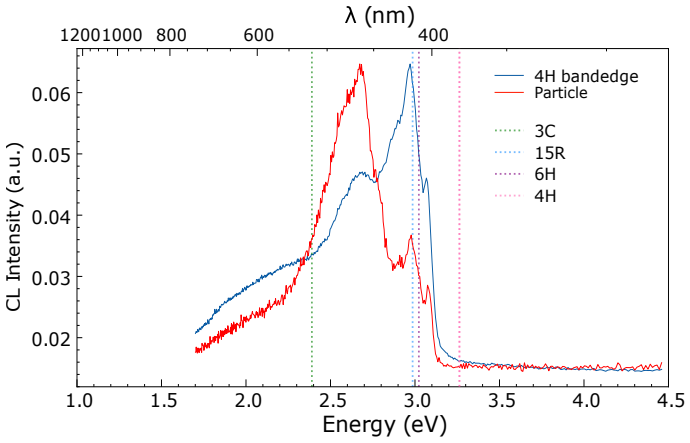

(b)

Figure 4.8: (a) Labelled CL spectra from *two individual* particles and (b) band edge measurment from the darker-coloured lower intensity spectrum in (a). Spectra in (a,b) are from the **1E14-300C** sample and was measured with a 10 keV at 80 K. An offset is added to the intensities in each spectrum to (a) highlight the present features and (b) align the band-edges for comparison.

only have CL band edge measurement from a small portion of the particle, as it overlaps with a 6H-SiC particle. Therefore the band-edge spectrum is given in Figure 4.8b where the CL spectra from the particle in question is in red. A spectrum from a confirmed 4H particle is presented as a reference. In the higher energy range of the spectra from the particle, the band edge is in agreement with the referenced 4H polytype. However, the position of the maximum intensity aligns with the 6H-polytype.

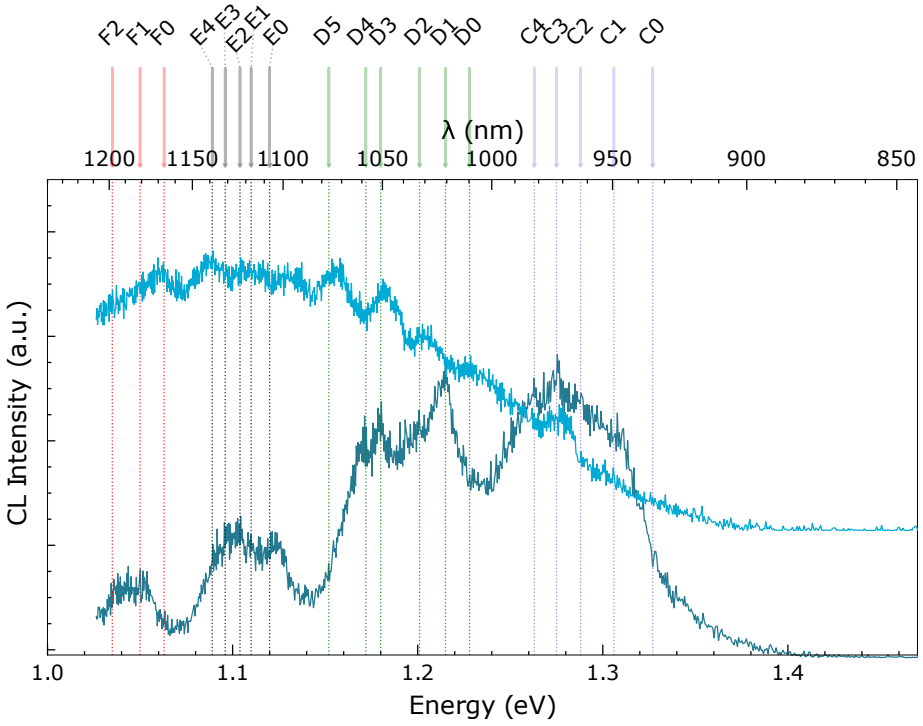

Figure 4.9: Background subtracted and labelled CL spectra from *two individual* particles in the **1E14-300C** sample was measured with a 10 keV at 80 K. The relative intensities of the individual contributions to the spectrum are shifted to highlight the present features.

In the lower energy range ($1.0 - 1.4$ eV), the signal-to-noise ratio becomes worse due to the different instrument optics. However, after background subtraction, the spectra reveal several emission centres. Figure 4.9 shows the spectra from two representative particles in this range. The darker bottom spectra have four wider bands, labelled C, D, E, and F, with individual higher intensity peaks. The top blue spectra have overall higher intensity in the lower energy range with several smaller, features in the range of $\sim 1.01 - 1.2$ eV (1040-1200 nm).

C3, seen in Figure 4.9, is the most prominent peak and possibly has the same origin as the M2 line at 1.273 eV (973.7 nm) in the PL spectra (see table 4.1). There is some contribution from the higher energy lines (C1-C2) as the peak "starts" at lower energy than the C3 line. In the other spectra (Figure 4.9, higher light blue line), the increased background around the C1-C3 peak indicates a broader feature. The origin of emission centres in this range is in literature not identified. Among the D-lines, D1, D3, and D4 stand out in the darker blue spectra in Figure 4.9, and in the light blue spectra, D5 and D3 stand out. The D3 line is indicated in Table 4.2 to possibly originate from the Cr^{3+} in the 6H polytype. The energy of the peak labelled D3 is 0.06 eV (1.8 nm) of the reported value for the extrinsic defect.

Further into the lower energy range, in Figure 4.9 we enter out of the PL scope in this work. Several of the E-lines are near the reported divacancy (VV) in 6H-SiC and 4H-SiC. Another possible candidate is the V2 colour centre in V_{Si} from 3C-SiC. The VV centre in 6H-SiC is most probable as the polytype of the particle is identified through band edge analysis as 6H-SiC. The lowest intensity F-lines are in somewhat agreement with NV centre ($N_C V_{Si}$) in 4H-SiC, but this is also improbable with the confirmed polytype.

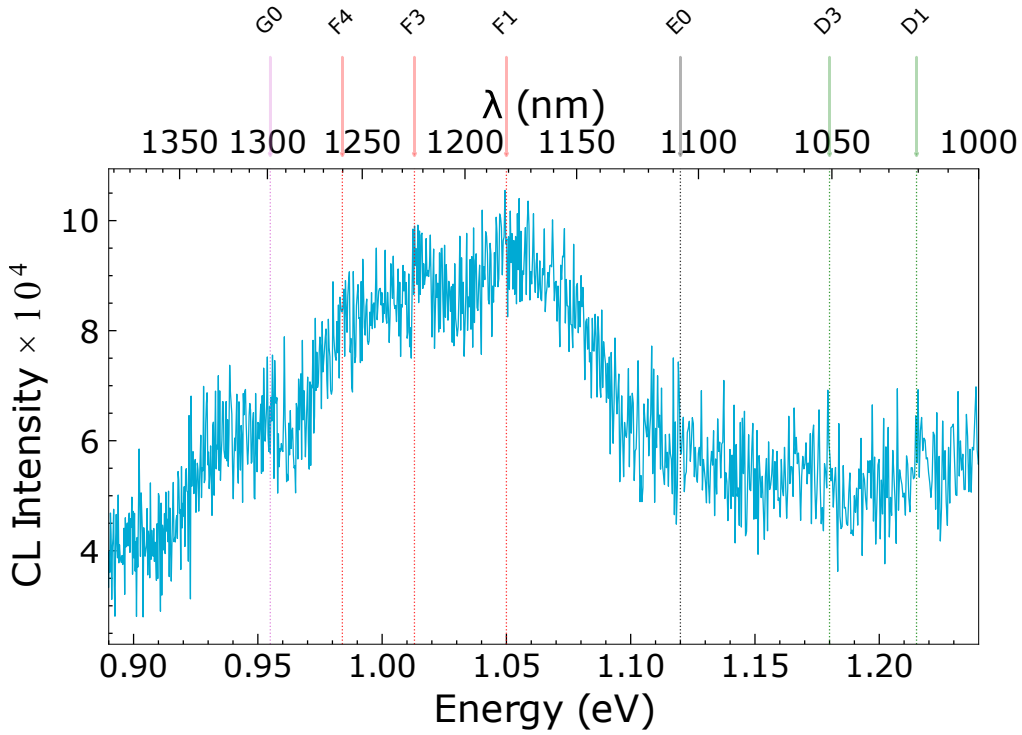

Figure 4.10: CL spectra in the IR region. All spectra are from the **1E14-300C** sample measured with a 10 keV at 80 K.

Spectra in the 0.9 - 1.3 eV (1000 - 1400 nm) range from two particles are shown in the Figures 4.10 and 4.11. The spectrum in 4.10 has a prominent feature centred around 1.05 eV marked with the F1 line, followed by two smaller features, labelled F3 and F4. The F1 line is in somewhat agreement with the N_CV_{Si} in 4H-SiC. There is reason to believe the two latter are part of the phonon sideband from the F1 peak. The rest of the features are not very distinct but are labelled as they agree with emission centres seen in other spectra.

The spectra in Figure 4.11 have significantly higher intensity compared to the spectra from the same energy range in Figure 4.10. Features in the lower energy range of the spectra, such as the G1 labelled peak, stand out, with less prominent features at higher energies. The G0-G1, and possibly F3-F4 are in the same energy range as the NV (N_CV_{Si}) centre in 6H. The present D-lines are in best agreement with the VV centre in 4H-SiC.

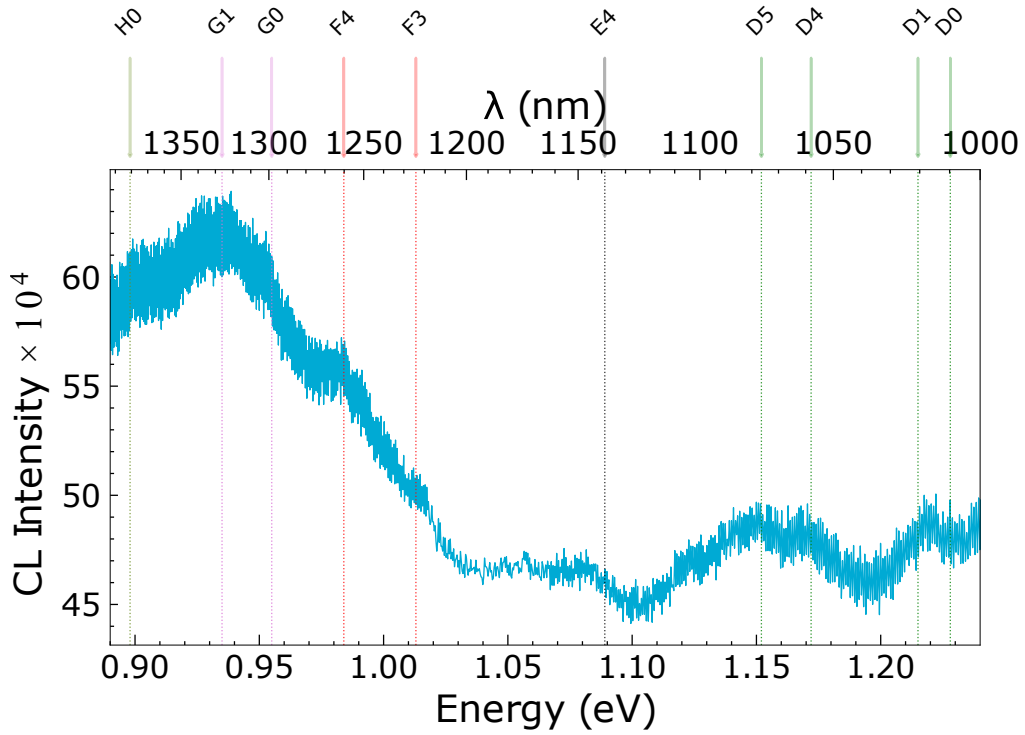

Figure 4.11: CL spectra in the IR region. All spectra are from the **1E14-300C** sample measured with a 10 keV at 80 K.

To explore an even lower energy range, we pushed the instrument beyond its optimized energy range. At 0.77 eV (1600 nm), the quantum efficiency of the sensor is reduced by $\sim 30 - 40\%$. The grating used is also out of its normal working range. Along with the operating temperature at 80 K, these factors made observations of emission centres increasingly difficult. Therefore, features in the two spectra in Figure 4.12 are not labelled. There is a tendency for a peak around 0.80- 0.85 eV (1500 nm) and 0.775 eV (1600 nm) in the two respective spectra, however, the origin of these features is uncertain and further work removing noise should be considered before any conclusions are to be drawn.

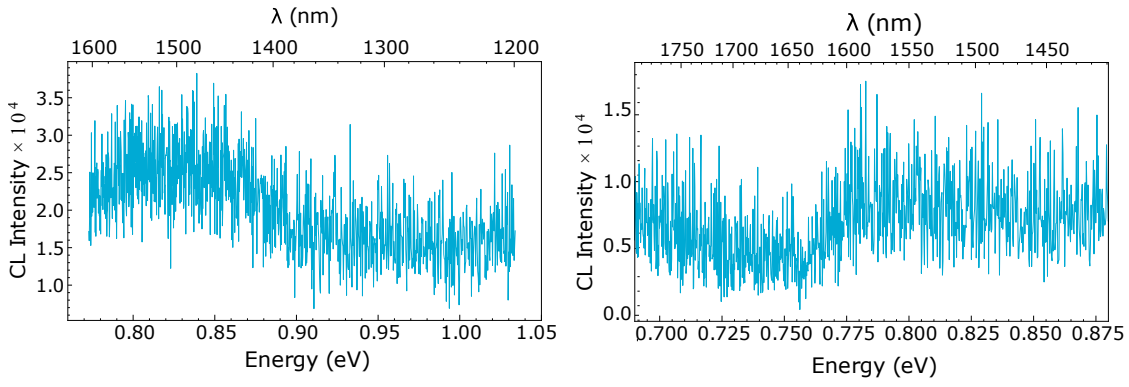

(a) (b)

Figure 4.12: CL spectra in the IR region. All spectra are from the **1E14-300C** sample measured with a 10 keV at 80 K.

Table 4.2: Summary of observed CL ZPLs in the 1E14-300C sample in order of ascending energies (descending wavelengths). The respective ID is marked (checkmark) if the emission line is found in PL as well. The labelling system is explained in the introduction to the chapter. The respective ZPLs reported in the literature are found listed in Table 2.2. Centres above the horizontal line, are out of range of the PL spectroscopy results in this work and are discussed and compared against reported centres in the literature.

ID	**E (meV)**	**λ(nm)**	*PL*	**Ref.**
H0	898.0	1380.8		
G1	935.0	1326.2		$N_C V_{Si}$ (6H-SiC)
G0	955.0	1298.4		
F5	967.0	1282.3		$N_C V_{Si}$ (6H-SiC)
F4	984.0	1260.2		
F3	1013.0	1224.1		$N_C V_{Si}$ (4H-SiC)
F2	1035.0	1198.1		
F1	1050.0	1181.0		$N_C V_{Si}$ (4H-SiC)
F0	1063.0	1166.5		
E4	1089.0	1138.7		VV (6H-SiC), or PL5, or PL6 (4H-SiC)
E3	1096.0	1131.4		VV (6H-SiC), or VV (4H-SiC)
E2	1104.0	1123.2		VV (6H-SiC)
E1	1110.0	1117.1		
E0	1120.0	1107.1		VV (6H-SiC), or V2 (3C-SiC), or VV (3C-SiC)
D5	1152.0	1076.4	✓(1078.4 nm)	VV (4H-SiC), Mo^{5+} (4H-SiC)
D4	1172.0	1058.0	✓(1057.7 nm)	
D3	1180.0	1050.8	✓(1049.0 nm)	Cr^{3+} (6H-SiC)
D2	1201.0	1032.5	✓(1030.9 nm)	
D1	1215.0	1020.6		
D0	1228.0	1009.8		
C4	1263.0	981.8		
C3	1275.0	972.5	✓(973.7 nm)	
C2	1288.0	962.7		
C1	1306.0	949.5	✓(948.4 nm)	
C0	1327.0	934.4	✓(934.0 nm)	
B7	1349.3	919.0	✓(919.0 nm)	
B6	1359.5	912.1	✓(912.1 nm)	UD3 unknown (4H-SiC)
B5	1369.0	905.8	✓(903.9 nm)	V3 (6H-SiC), possibly, but less probable V3 (15R-SiC)
B4	1397.0	887.6	✓(887.6 nm)	V2 (6H-SiC), possibly, but less probable V2 (15R-SiC)
B3	1433.3	865.1	✓(865.0 nm)	V1 (6H-SiC)
B2	1442.0	859.9		V1'(4H-SiC)
B1	1494.0	830.0		
B0	1543.0	803.6		
A5	1910.0	649.2		$CAV^{(+)}$ (4H-SiC)
A4	1950.0	635.9		
A3	2000.0	620.0		

A2	2030.0	610.8	
A1	2110.0	587.7	
A0	2208.0	561.6	D1 (4H-SiC)

4.3.2 Annealing Series

Here the effect of higher annealing temperatures will be presented and discussed. Thus, the emission centres presented in Section 4.3.1 are compared to centres observed in the 1E14-1000C sample as well as the as-received sample will be analyzed. For the as-received sample, only a few features were discovered, and spectra from this sample are therefore only presented in Figure 4.15. However, previous measurements on the same material (as-received) executed by Dr. Marianne Etzelmüller Bathen have revealed features of interest in the $\sim$ 1.28 eV (970 nm) region. These results are provided in Figure 4.16 for completeness in the discussion.

Temperature series focused on the $\sim$ 2.0 eV (610 nm) peak and the silicon-vacancy, are shown in Figure 4.13 and 4.14, respectively. In both spectra, the average intensity in the 300° C annealed sample is 6 - 10 times greater than the average intensity in the 1000° C annealed sample which indicates out-annealing of defects. The discovery is in agreement with the findings in [48]. Even though the average emission intensity from the 300° C annealed sample surpasses the average emission intensity from particles in the 1000° C annealed sample, there was a predominance of particles with the $\sim$ 2.0 eV (610 nm) emission centre in the latter sample. The average emission from the 300° C sample is dominated by the emission from *a single* particle. The $\sim$ 2.0 eV emission centre was discovered in other particles in the 300° C sample as well, but with a significantly lower intensity.

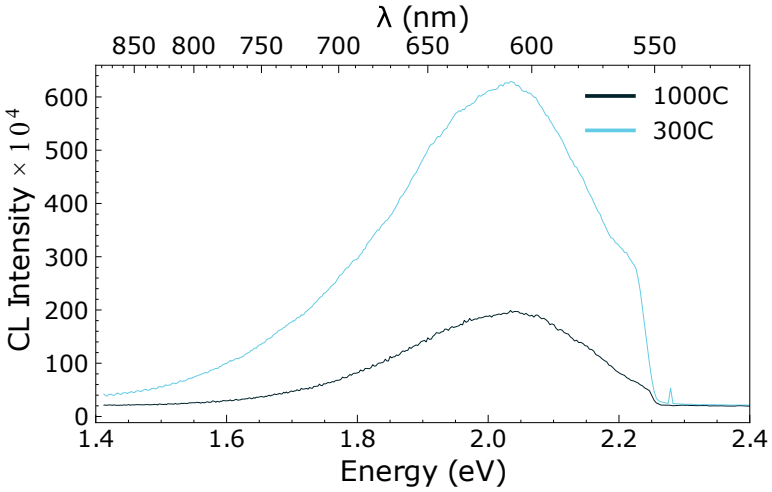

Figure 4.13: Average CL spectra from the many particles found in the 1E14-300C and 1E14 - 1000C sample focused on the $\sim$ 2.0 eV feature. The sudden cut-off in higher energy range is caused by the applied filter (500 nm longpass). Measured with 10 keV at 80 K

Measuring the V_{Si} in the 1E14-1000C sample was anticipated because of a high presence in the 1E14-300C sample. The colour centre becomes mobile at $400 - 700\,^{\circ}$ C (in donor doped material), hence making complexes with other defects [37, 49] or the out annealing the V_{Si} likely explains the significantly lower intensity compared to the emission intensity from the V_{Si} in the 1E14-300C

sample. Fast cooling of the samples during sample preparation steps may have restricted the diffusion of defects. The ZPLs V1 and V2 from the silicon-vacancy in the 1E14-1000C sample are narrower and have a relatively high intensity compared to the PSB and V3, shown in the insert in Figure 4.14. The phenomena could be a result of annealing reducing structural damage, which again reduces the induced non-radioactive channels [37] and hence enhance the signal from specific defects.

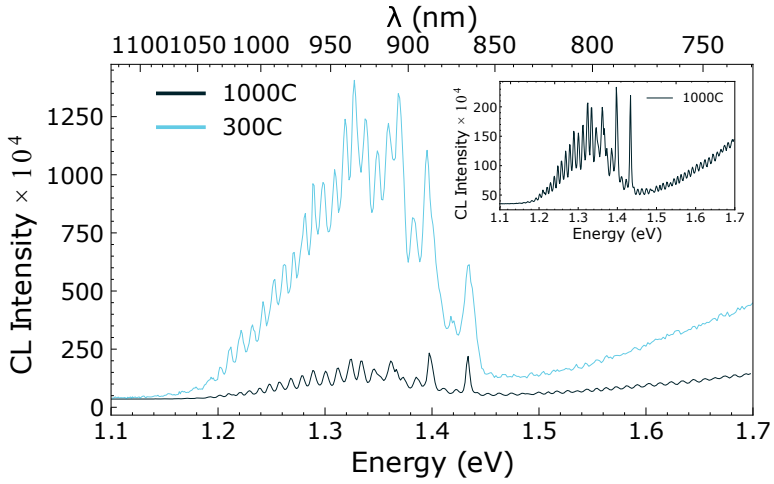

Figure 4.14: CL spectra from the maximum intensity particles found in the 1E14-300C and 1E14 - 1000C samples. The insert is the same as the 1000° C spectra, included to show the sharper lines. Measured with 10 keV at 80 K

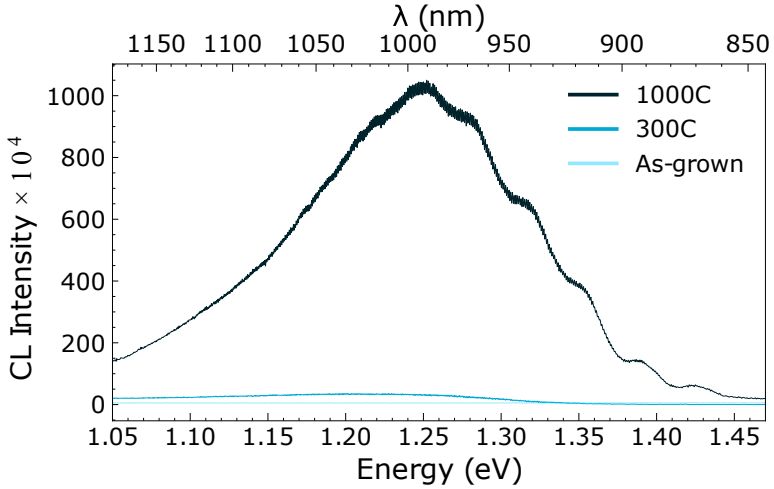

Figure 4.15: Background subtracted CL spectra from the maximum intensity particle found in the as-received, 1E14-300C, and 1E14 - 1000C samples. Masured with 10 keV at 80 K

CL spectra in the NIR range (850 - 1150 nm) from the as-received sample together with the 1E14-300C and 1E14-1000C, are shown in Figure 4.15. Here the intensity from the 1E14-1000C sample dominates, followed by the 1E14-300C and as-received sample. There is approximately a 20 times difference in intensity between the 1000° C annealed sample, and the 300° C annealed

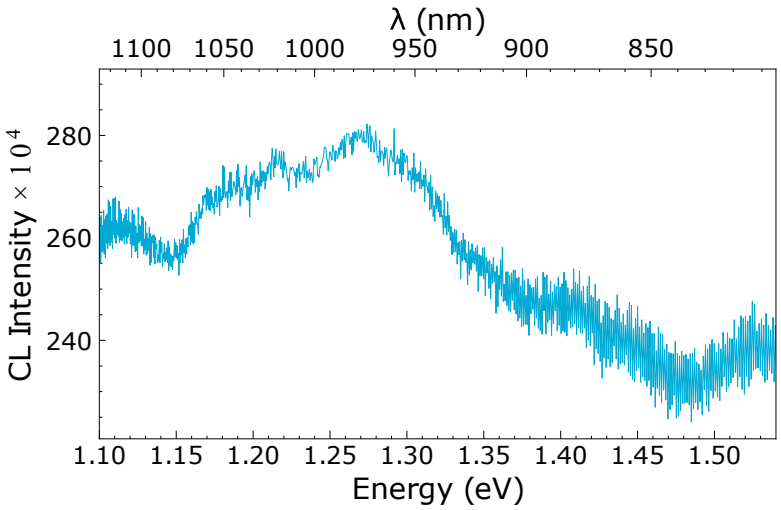

Figure 4.16: CL spectra in the IR region from the **as-received** sample measured with 10 keV at 80 K.

and as-received samples, comparing the maximum intensity point in each spectrum. In this energy range, the intensity from the as-received sample is more or less indistinguishable from zero.

The CL from the 1E14-1000C sample consists of a larger, wide peak centred at ~ 1.25 eV (990 nm), with several smaller features hidden in the PSBs of the respective peak. Starting from the higher energy range, the three first peaks are in good agreement with the V1, V2, and V3 lines from the 6H-SiC silicon-vacancy. The fourth and fifth peaks at ~ 1.32 eV (940 nm) and ~ 1.28 (970 nm) are of unknown origin. The ~ 1.32 eV (940 nm) could be a PSB from the silicon-vacancy, but the ~ 1.28 (970 nm) feature has been discovered in an as-received sample by Dr. Marianne Etzelmüller Bathen, shown in Figure 4.16. It was not found in any particles in the 1E14-300C sample but appeared after the 1000° C anneal. These findings suggest that it is of extrinsic origin. This feature is in the same energy range as the M-lines discovered in PL, see section 4.2 and table 4.1.

Figures 4.17 and 4.18 show representative spectra from the 1E14-1000C sample in the range of $\sim 0.8 - 1.25$ eV (1000-1600 nm). In section 4.3.1, we found very few color centres below ~ 1.03 eV (1200 nm) in the 1E14-300C sample. Even though the spectra in the range of $\sim 0.8 - 1.25$ eV (1000-1400 nm) shown in Figure 4.10 and 4.11, revealed some features, the same were not discovered in the 1000° C annealed sample. This makes it difficult to compare the two samples in question. The signal to noise ratio in the spectra in Figure 4.12a and 4.12b, also from the 1E14-300C sample, is as mentioned so bad that distinguishing features from noise is rather difficult. We will therefore proceed with discussing features appearing after the 1000° C anneal without a direct comparison with the 300° C annealed sample. Herein we again label the features in the spectra which are distinct from the background.

As can be seen in the Figures 4.17, 4.18a, and 4.18b, a series of features were observed in the 1E14-1000C sample. In Figure 4.17, the two spectra decrease in intensity moving into lower energies. The topmost spectra consist of a wide peak centred around ~ 1.15 eV (1180 nm) with narrower peaks at D0, D2, D3 and D5. Note that the labelled D0-5 peaks could be caused by interference related effects in the instrument. As for the other labelled lines, E1, E4, F0, F2 and F5, are included

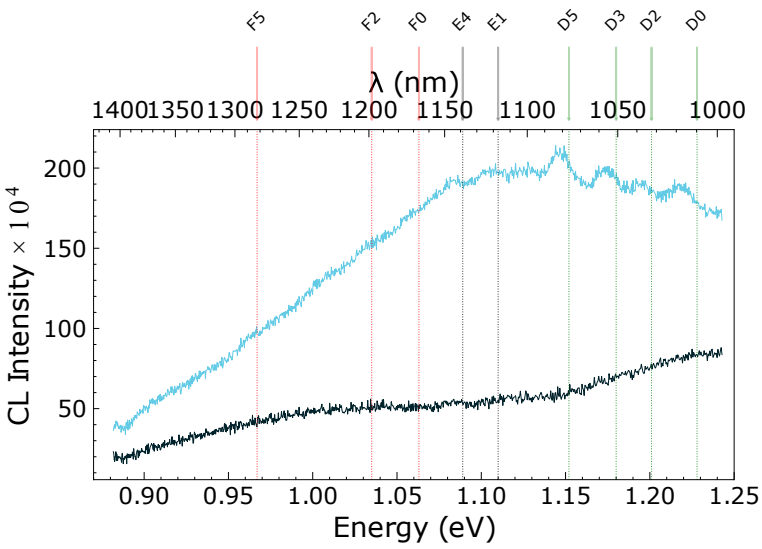

Figure 4.17: Background subtracted CL spectra in the IR region from the **1E14-1000C** sample measured with 10 keV at 80 K.

because of irregularities in the wider peak which are consistent with emission centres found in other particles. The bottom spectra can seem to have two larger peaks, the first centred below 1.25 eV (1000 nm) and the other around ~ 1.025 eV (1200 nm).

The three spectra shown in Figures 4.18a reveal a ZPL, labelled F5, at 0.967 eV (1282.3 nm). In the lower energy end of this spectra, it seems like there is a sudden increase in intensity, which could arise from another ZPL. The topmost, light blue spectra herein have a wider feature ranging from the higher energy part of the spectra and decrease after the first ZPL. This seems to have smaller features, but they are difficult to distinguish from noise. The two other spectra are rather flat without any specific features. The middle (blue) spectra certainly have the most prominent ZPL, and there might appear to be a PSB after the ZPL.

Features in the last spectra, found in Figure 4.18b, are somewhat similar to the two other spectra. Here we observe the ZPL labelled F5 in the two lower (black and blue) spectra, along with the steep increase in intensity at the lower energy end of the spectra. The F5 labelled feature is in the range of the NV centre in 6H-SiC with an energy of 0.971 eV (1278 nm). The top, light blue spectra have a wider peak in the lower energy range, centred around the D1 line. There is also a feature centred around the E2 line, this could however be the PSB of the D1 labelled feature. In the middle spectra the same high energy, wide peak is present, but with a lower intensity than the upper spectra. Except for the ZPLs, the bottom spectra have a flat structure throughout the energy range.

Considering now the $\sim 0.75 - 1.05$ eV (1200-1600 nm) range, shown in Figure 4.19, one can observe two different features. In the top (light blue) spectra, parts of a wider peak are observed, which is centred around ~ 1.05 eV (1200 nm). It could be the same feature seen in the topmost, light blue spectra in Figure 4.18a. Between $\sim 0.85 - 0.90$, eV there is an increase in intensity, again indicating emission, labelled H1. The peak is followed by an intensity decrease throughout the rest of the spectra. The same H1 feature is significantly prominent in the bottom (black) spectra. Up until ~ 0.9 eV (1400 nm), the signal is relatively flat and characterized by noise. The sudden rise in

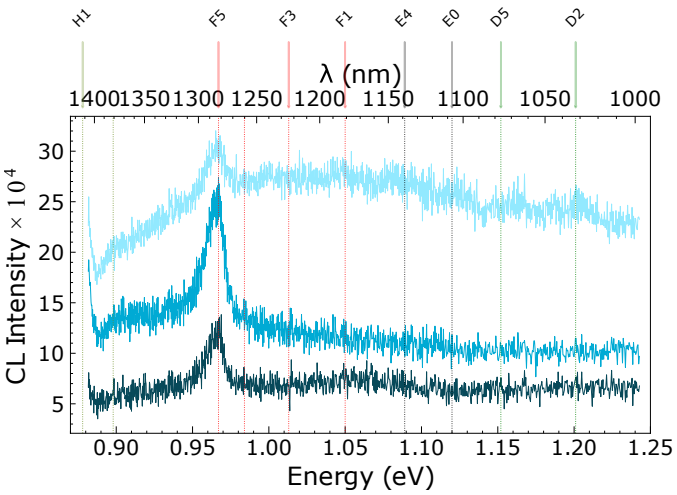

(a)

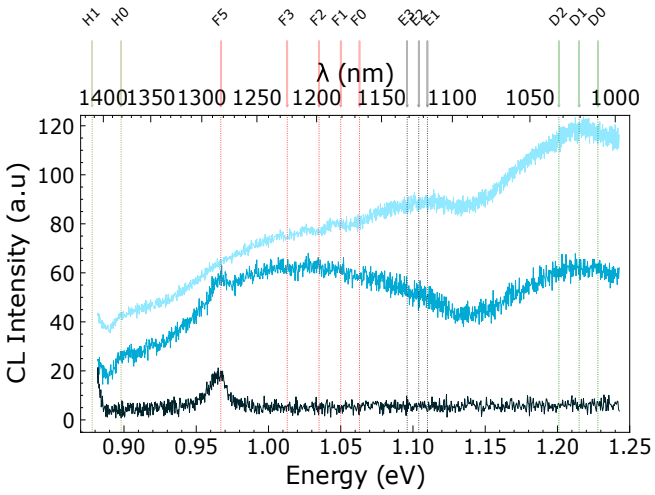

(b)

Figure 4.18: Background subtracted CL spectra in the IR region from the **1E14-1000C** sample measured with 10 keV at 80 K. In (c) the intensity of each spectra is shifted ~ 10 intensity counts relative to each other to enhance the F5 labelled feature.

intensity resembles nothing seen in the powder so far. As this feature was found in several particles in close proximity with varying intensity, artefacts as the origin are excluded.

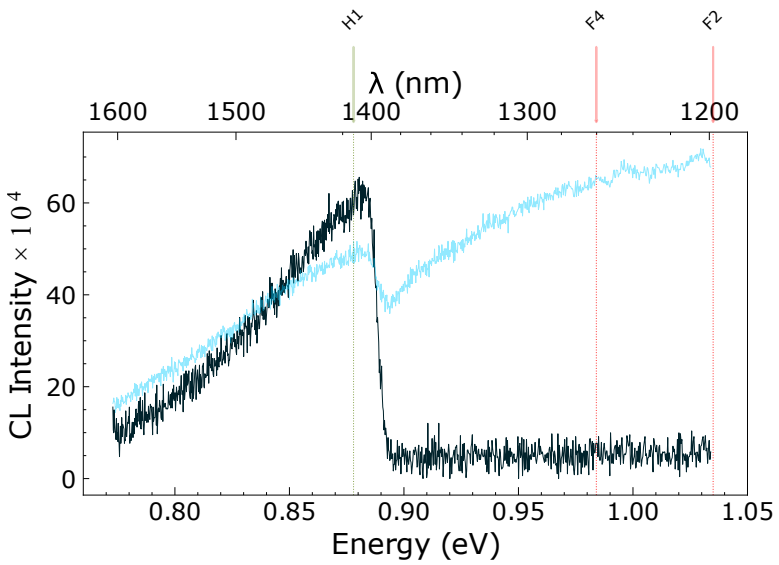

Figure 4.19: Background subtracted CL spectra in the IR region from the **1E14-1000C** sample measured with 10 keV at 80 K.

4.3.3 Emission from Individual Particles

Throughout the CL study of the particles, we have discovered that the luminescence from individual and within sole particles differs. This section is therefore devoted to the study of CL from individual particles. As this section is not about identifying particular colour centres, we refer to the colour centres with their names as given in the literature or energy (wavelength) if they are unidentified. We start discussing how the particle geometry affects the emission from the silicon-vacancy before looking at other emission centres. Note that we here give a sole discussion of based on the shape/geometry of the particles. Therefore spectra from both the *1E14-300C* and *1E14-1000C* samples are included to have a better basis with several particles for the discussions. The sample in question is both mentioned in the presentation and the caption of the relevant figure. Some of the CL spectra, especially in the lower energy range, are background subtracted. If so, it is indicated in the caption of the figure.

The Silicon Vacancy

Cathodoluminescence from the silicon-vacancy (V_{Si}) was in this work observed in most particles and samples. In some particles, the ZPLs from V1, V2 and V3 dominate, while in others, the PSB overlaps the ZPLs, as shown in Figure 4.20 and 4.22. Here, we try to understand if the geometry of the SiC particle affects the emission through effects such as waveguiding.

In Figure 4.20a three CL spectra from the *1E14-300C* sample obtained from a large area in the particles in Figure 4.20b are presented. The particles are labelled P1, P2 and P3. Looking into the geometry of the particles, the P1 particle has an "arrowhead" shape. P2 appears to be more spherical while P3 could be more of a pyramidal shape, with the tip of the pyramid pointing out of the sheet plane. As seen in the respective spectra, the P1 arrowhead particle exhibit the strongest CL with distinct ZPLs from the V_{Si}, while the spectrum from the spherical P2 particle (deep blue spectrum) is relatively flat. The emission from the pyramidal P3 particle seems to be dominated by the V_{Si} PSB, which can be seen as a "bump" in the black spectra in Figure 4.20a.

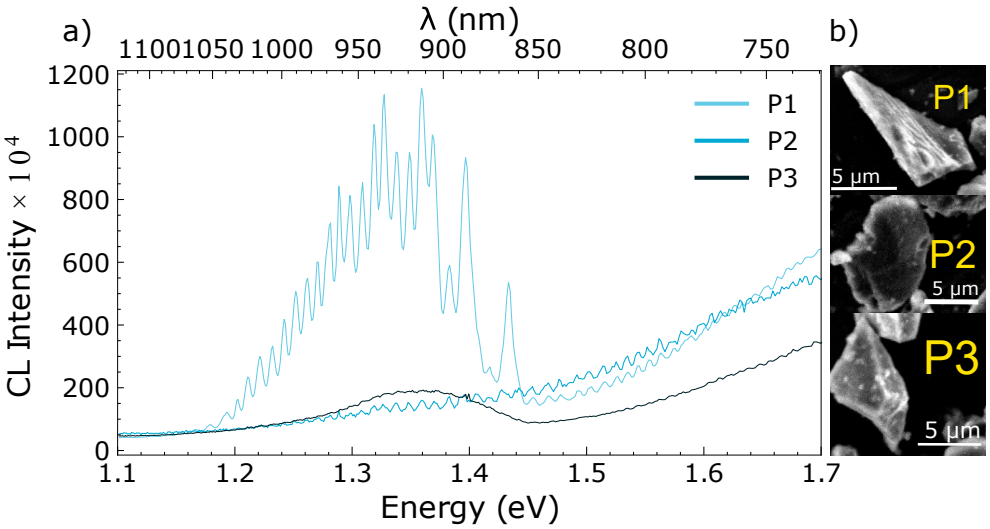

Figure 4.20: (a) CL spectra in the visible region with a focus on the V1, V2 and V3 centres from three particles marked (P1-P3) in SEM micrograph in (b). All spectra and maps of the **1E14-300C** sample were measured with a 10 keV at 80 K.

Further high-resolution spectroscopy of the P1 particle in Figure 4.20, indicates a tendency of higher intensity CL emission from edges and ridges within a single particle. This observation is shown in Figure 4.21a, where the CL spectra with decreasing intensity from positions (1) - (6) within the P1 particle are given. The labelled positions are shown in the SEM micrograph in Figure 4.21b. It is not straightforward to distinguish flat surfaces against angled surfaces in SEM images, as the contrast depends on the orientation of the surface relative to the detector. More secondary electrons will escape from edges than surfaces, giving a higher contrast. There appears to be an elevation in the middle of the particle (between positions (1) and (2)). The CL intensity from the two positions, especially position (1), is significantly stronger compared to the other positions. A considerable signal appears from position (3), which seems to originate from a surface area by the uniform, dark colour contrast in proximity, rather than an elevated ridge which is believed to be the case between positions (1) and (2). The CL spectra from positions (4) and (6) are obtained from the narrow tip of the particle in the top left corner of the SEM micrograph. The emission intensities from these positions are relatively low compared to other positions. Positions (5) can seem to be an immersion in the particle by the dark contrast compared to the interpreted elevation between positions (1) and (2). The CL intensity from (5) is the second-lowest observed within the P1 particle.

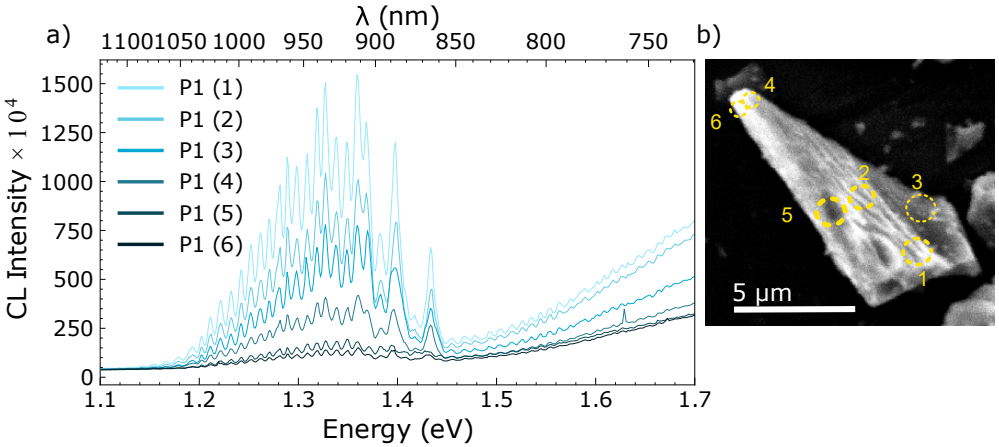

Figure 4.21: (a) CL spectra with decreasing intensity from position (1) to position (6) in the visible region from six positions in a single particle marked in the SEM micrograph in (b). Same particle as P1 in Figure 4.20. All spectra of the **1E14-300C** sample are measured with 10 keV at 80 K.

In Figure 4.22a particles in the *1E14-1000C* sample clearly emitting in the range of the the V_{Si} are studied. Also here the particles are labelled P1, P2 and P3, but they are not the same as the particles in Figure 4.20. Determining the geometry of the particles in the 1E14-1000C sample is influenced by the resolution of the SEM micrograph, as seen in Figure 4.22b. However, P3 could be considered as more spherical with pointy ends, compared to the two others (P1 and P2), which are arrowhead/triangle shaped. P2 could also be two particles on top of each other indicated by the contrast between the high contrast triangle on top of a darker, oddly shaped particle. The average emission intensity from the V_{Si} is significantly higher and has clear ZPLs in the arrowhead-shaped particles P1 and P2, compared to the rounded/spherical P3 particle. This observation is in agreement with the V_{Si} higher intensity emission from arrowhead/triangle particles and lower emission intensity in spherical/rounded particles in the 1E14-300C sample in Figure 4.20. Hence it can be so that the triangle-shaped particles exhibit stronger luminescence compared to other geometries. The effect on the emission of the particle geometry will be studied more in Section 4.4 using numerical simulations of electromagnetic waves.

Possible explanations for the different emission intensities within the particles include i) a strong variation in defect concentration, ii) waveguiding where the light leaves the particle in specific regions and or iii), a predominance of non-radiative recombination caused as a result of thin particles with a lot more surface and less room for defects in "bulk". In case ii) this would mean that the shape of the particle influences the emission. For example, the ridge discussed in P1 in Figure 4.21 can guide the light through internal reflection to specific areas of the particle. This can lead to areas with higher CL intensity. The emission from particles classified as more spherical is conceivable to be uniformly spread in many directions, whilst the triangle particles have a more directional emission. The non-uniform CL intensity from different samples from individual particles can also be because of inhomogeneous proton irradiation.

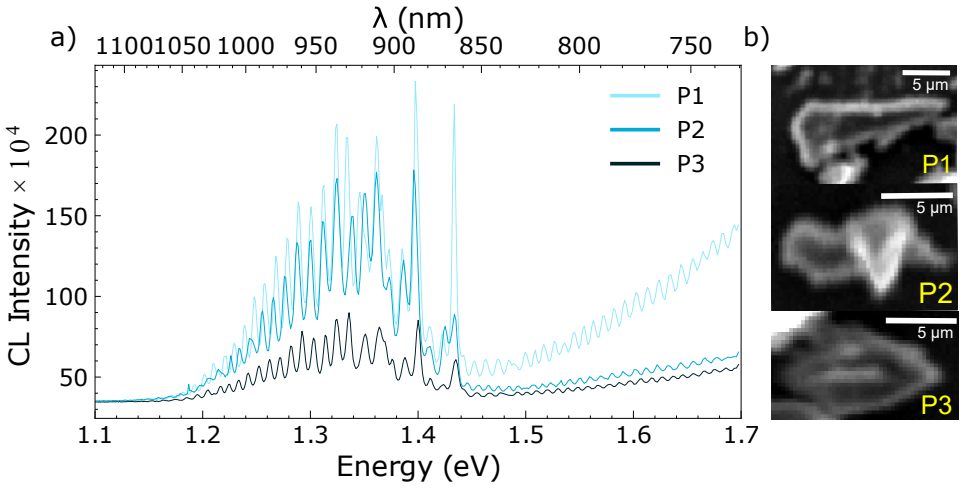

Figure 4.22: (a) CL spectra in the visible region from large areas in the three particles marked in the SEM micrograph in (b). All spectra and maps of the **1E14-1000C** sample were measured with a 10 keV at 80 K

Other defects

CL spectra from the *1E14-300C* sample in the energy range of 1.4 - 2.4 eV (550-850 nm) from large areas of five particles are shown in Figure 4.23a and with the respective SEM micrograph in 4.23b. The five particles are again labelled independently P1-5. The spectra are focused on the ~ 2.0 (~ 610 nm) and ~ 1.9 (~ 660 nm) features. The resolution in the SEM micrograph in Figure 4.23b is not sufficient to accurately determine the geometries of the particles, especially for the P1 and P4 particles. However, a careful study of the P3 particle could indicate a triangled geometry by the shape of the white area. While P2 and P5 could be rectangles/squares. The CL intensity decreases from P1-5. Among the P2, P3 and P5 particles, the emission intensity from P2 is the highest with decreasing intensity from the P3 and P5. However, as the particle geometries here are uncertain, no conclusions are drawn.

The length of the P5 is ~ 2.5 µm, compared to a ~ 5 µm length of the other particles P1-4. As pointed out, the emission intensity from P5 is lower than in most of the particles in question. The size could hence affect the emission, but emission in a smaller, possibly thinner particle, could be dominated by non-radiative emission from a predominance of surface defects, compared to defects in "bulk".

High-resolution CL spectroscopy results from the already presented P4 particle in Figure 4.23 is shown in Figure 4.24 to further understand the emission within the SiC particles. The CL intensity in Figure 4.24a decreases from position (1) - (4) marked in the SEM micrograph in Figure 4.24b. Positions (1), (2) and (3) are understood as corners, while position (4) is somewhat in the centre of the P4 particle. Position (1) stands out with the relatively high emission intensity, especially in the higher energy range of the spectra. The emission from the remaining three positions, (2), (3) and (4) are relatively similar with the exception of the ~ 1.9 eV (~ 650 nm) feature originating position (2). Even though the intensity from the corners in positions (1-3) is slightly higher than in the centre, position (4), it is not possible to rule out the presence of other geometrical features of the particle, such as elevations or cavities, because of the resolution SEM micrograph. The intensities

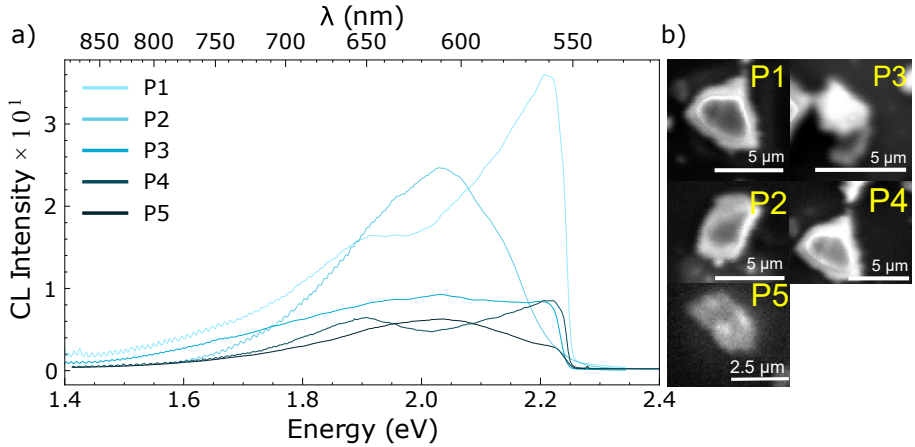

s

Figure 4.23: (a) CL spectra in the UV-VIS region with focus on the unfamiliar 2 eV signal from several particles marked in (b). All spectra and maps of the **1E14-300C** sample measured with 10 keV at 80 K. The sudden decrease in intensity at ~ 2.21 eV (550 nm) is because of the use of a 500 nm filter before the spectrograph.

from the (2) and (3) labelled corners are also significantly low and similar to position (4). Hence, we will suggest further measurements of the emission from differently shaped particles.

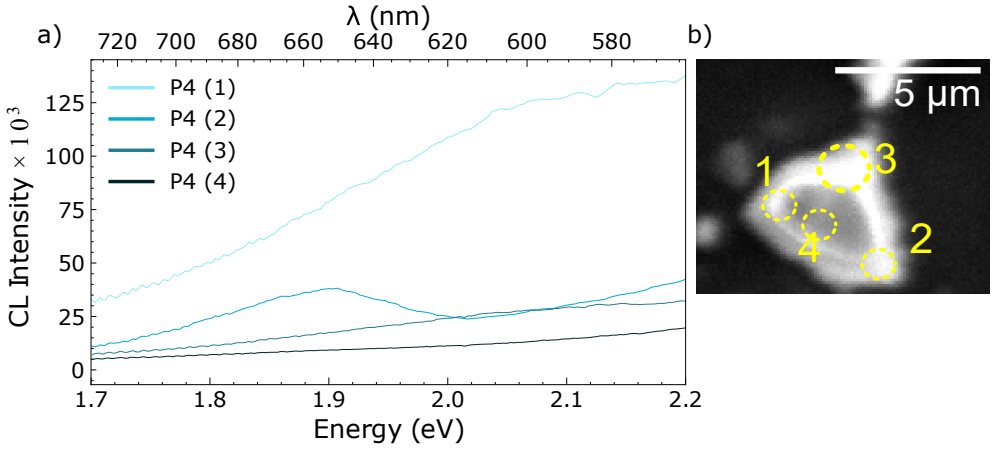

Figure 4.24: (a) CL spectra in the UV-VIS region of a single particle shown in the SEM micrograph in (b). All spectra are of the P4 particle also studied in Figure 4.23 from the **1E14-300C** sample measured with 10 keV at 80 K.

Emission from three particles in the *1E14-1000C* sample in the energy range of 1.4 - 2.4 eV (550-850 nm) is presented in Figure 4.25. The particles, shown in the SEM micrograph in Figure 4.25b, are labelled P1, P2 and P3. P1 is interpreted as a triangle/arrowhead, and the P2 particle reassembles a triangle with a slightly rounded tip. The geometry of the P3 particle is less clear as it might appear as if it consists of two bright contrast particles on top of each other. The P2 particle is approximately 2.5 µm shorter than P1. The CL intensity from the particles decreases from the maximum intensity emitted from the arrowhead-shaped P1 particle to the less certain shaped P3 particle. This observation strengthens the previous findings regarding a higher intensity emission from arrowheaded/triangled particles, previously discussed in relation to Figures 4.20 and 4.22.

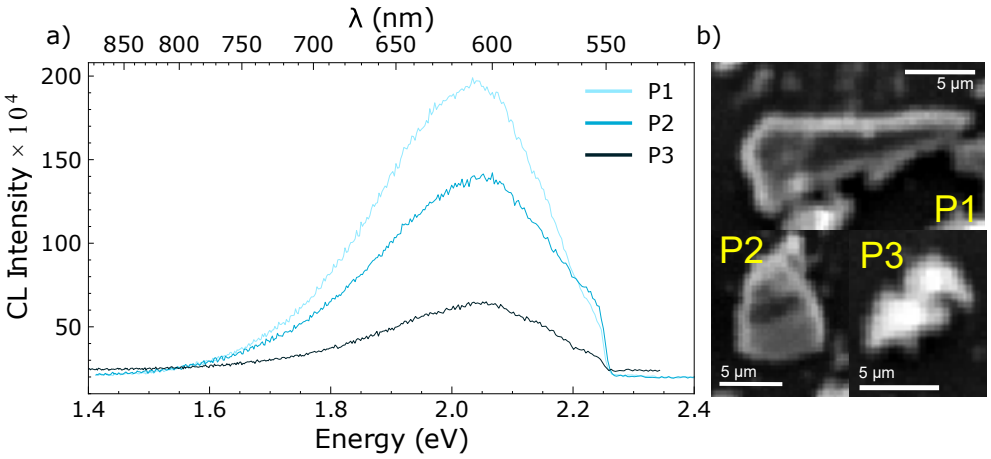

Figure 4.25: (a) CL spectra in the UV-VIS region from several particles marked in the SEM micrograph in (b). All spectra and maps of the **1E14-1000C** sample measured with 10 keV at 80 K. A 500 nm longpass filter has been used.

In the lower energy range (1.0 - 1.5 eV), CL spectra from differently shaped particles revealed variable emission intensity. However, as the observations in this range were quite similar to the already discussed particle emission, the spectra are presented in Appendix B.

4.4 FDTD Simulations

To investigate how luminescence from SiC particles is influenced by particle shape and the distribution of defects within the structure, numerical calculations of electromagnetic fields were conducted by implementing the FDTD algorithm. Here an analysis of the near to far fields calculated 1 m away from the simulation region is presented. Thereafter an analysis of particle geometries and positioning of defects is given. The simulation results are not meant to be *directly* compared to the CL results. It should be interpreted as supplementary information for the understanding of the luminescence from the SiC particles. Note that the fields are normalized (see section 2.4).

The far-field emission from 70 dipole sources with randomized phases distributed evenly or concentrated at specific points within structures of different geometries will be presented. The simulated polytype is 6H-SiC, as this is the most common polytype in the SiC powder studied in this work. The dipole sources are used to mimic the excited defects studied with CL spectroscopy. Three different geometries have been considered: a cube, a pyramid and a sphere with a size of 4 µm

(the size definition is given in Section 3.3.2 under "Geometries"). The emission wavelength from the dipole source was set to 870 nm. It could be useful to analyze the emission from different dipole emission wavelengths to understand the behaviour of different colour centres within the SiC particles. However, as the difference in refractive index over a long span of wavelengths is very small, (see Figure 3.8), we will not analyze the emission from different dipole emission wavelengths.

For quantum technology applications, ideal emission sources are single-photon emitters. In the simulations, classical dipole sources optimized for short pulse emitting a single wave packet are used to mimic the defect emission in the SiC particles.

4.4.1 Near to Far-field

To understand the far-field projections, a near to far-field analysis of a 4 µm sized pyramid is provided in Figure 4.26. The difference between the near field obtained directly from the monitor above the structure (see section 3.3.2), and the far-field, obtained from different sizes of a hemisphere above the structure, is analysed. Only one dipole was used in this simulation, as the purpose is the differences in the fields.

In the near field in Figure 4.26 the intensities can be directly related to certain points in the

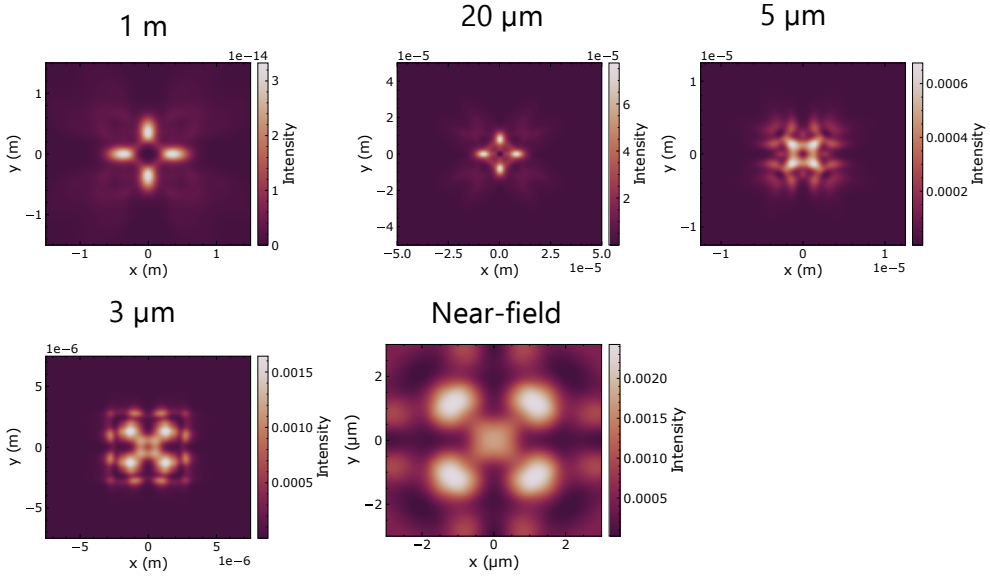

Figure 4.26: Near to far field analysis of a 4 µm pyramidal structure simulated with one dipole with the field intensity from the near-field, 3 µm, 5 µm, 20 µm and 1 m away from the simulation region.

structure. The four, high-intensity points surrounding a lower intensity point correspond to the four edges of the pyramid (the "lines" connecting the bottom corners to the tip of the pyramid). The lower intensity point in the centre of the field corresponds to the tip of the pyramid.

In the far-field projection to a 3 µm size hemisphere, the intensity pattern is quite similar to the near-field, as the same four bright points surround a lower intensity point in the centre of the hemisphere. Hence it is here still possible to recognise the structure. However increasing the size of the hemisphere further, especially above 5 µm, the high-intensity points rotate $\sim 45°$ (clock- or anticlockwise yields the same field).

As implementing the particles in lines of quantum communication is considered a potential application, the far-field projection is of greater interest as it reveals the directionality of the emission rather than wherein the particle the light exits. Hence, we continue the analysis of the simulations by studying the emission in the far-field.

4.4.2 Positioning of the Defect

The far-fields from the **pyramidal** structure with different positioning of the dipoles can be seen in Figure 4.27. Here, the dipoles are (a) spread randomly throughout the structure, (b) located in the bottom corner, (c) close to the tip, (d) close to a surface and (e) in the centre of the pyramid. The results are presented in pairs, where the left figure shows the far-field intensity projected onto a hemisphere from a monitor in the z-plane, and the right figure illustrates the shape of the pyramid and the dipole positioning (blue dots) in the structure.

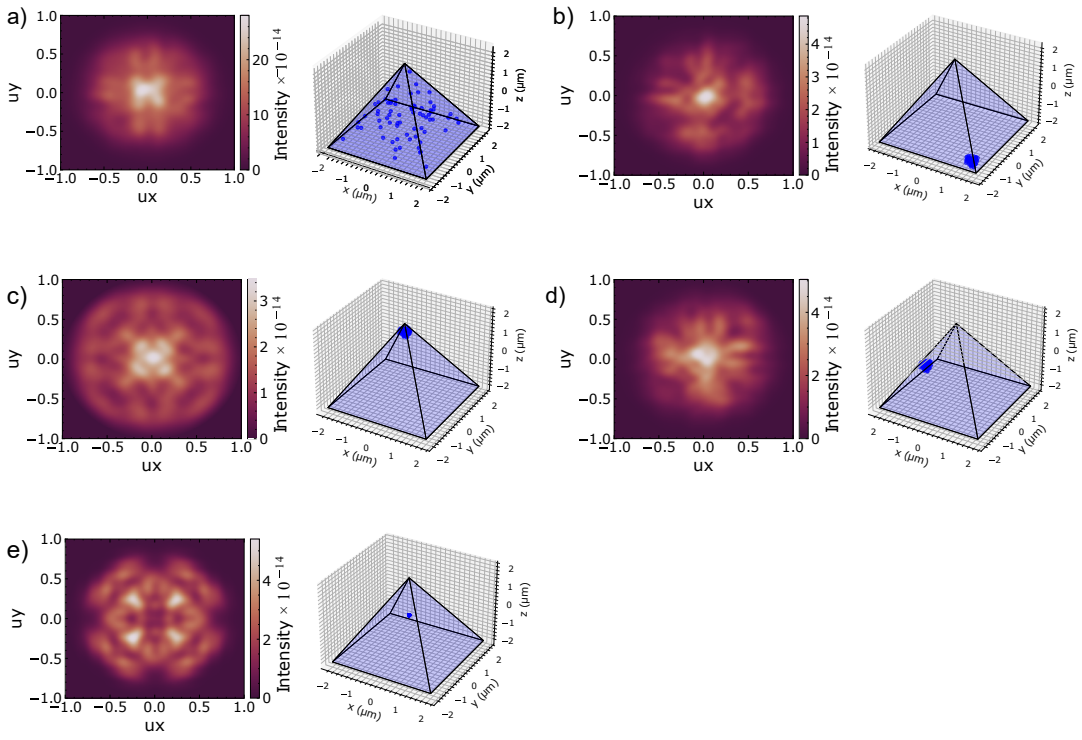

Figure 4.27: Far-field intensity from a pyramid of 4 µm with 70 dipoles positioned randomly (a) throughout the whole structure, (b) at a bottom corner, (c) at the top, (d) in the center.

In the Figure, 4.27a-d, the highest far-field emission intensity is located in the centre of the figure, with a decreasing intensity towards the edges. Hence, the geometry of the particle concentrates the emission in one direction (here the z-direction) which is desirable for e.g. quantum communication.

The maximum far-field intensity in Figure 4.27 varies from $\sim 3.5 - 30 \times 10^{-14}$ and are in all panels but Figure 4.27e centred in the middle of the hemispherical detectors. The emission from randomly distributed dipoles, shown in Figure 4.27a, clearly exhibits the highest maximum intensity of 30×10^{-14}. When the dipoles are positioned close to the tip of the pyramid, as seen in Figure 4.27c,

the maximum intensity is the lowest in the results herein. This could be because of destructive interference, but as the other dipole configurations have the same setup it is likely caused by different factors.

Figure 4.27e stands out by the four-fold symmetry of the electromagnetic field and the maximum intensity is located in the four bright areas close to the centre of the figure. The points could be related to the four edges (the line connecting the bottom corners with the tip) of the pyramid as. However, because of the transformation of the far-field, this cannot be said with certainty.

The darker areas surrounding the brighter, higher intensity areas in the far-field intensity plot indicate that less light is emitted in the xy plane (outward direction). The smaller and brighter the intensity area is, the more light is emitted in the z (upward) direction.

In the field from the dipole concentrated at the tip of the pyramid, in Figure 4.27c, it seems like there is more emission from the surfaces as the area where the emission exits the pyramid is larger. The field from the spread-out dipoles, in Figure 4.27a, seems to exit the pyramid in closer proximity to the top of the pyramid, as the intensity is spread out on a smaller area. The spread of the emission could be analyzed more quantitatively by doing for example Gaussian fitting but is put out of the scope of the present work.

Moving the dipoles out of the centre of the structure, as in Figure 4.27b and 4.27d, breaks the symmetry of the field. In Figure 4.27b, where the dipoles are positioned in the bottom corner, the emission in the field is shifted slightly towards the bottom right corner of the plot, indicating that more light exits the structure from the sides of the pyramid. However, the smaller, highest intensity area in the centre of the figure, seems more concentrated compared to the rest of the plots. When the dipoles are placed at one of the surfaces, as in Figure 4.27d, the field is shifted slightly towards the left (towards the uy axis). The same also applies to the maximum intensity point in the centre of the figure, which is here more spread out towards the left of the field, compared to Figure 4.27b.

The electromagnetic fields from the **cubic** structure with different positioning of the 70 dipoles, can be seen in the far-field view in Figure 4.28. These results are presented in the same manner as described for the pyramid structure. Here we have positioned the dipoles in (a) spread out randomly, (b) in the centre, (c) in a corner, and (d) at the top surface of the cube.

The maximum intensity from the four different orientations ranges from $\sim 2\times10^{-14}$ to $\sim 4.5\times10^{-14}$. The light seems to exit the structure from the top surface to the greatest extent, indicated by bright areas in the proximity to the centre of the fields. The emission is spread out over a relatively large area, almost reaching the edges of the plot. Indicating that this structure spreads the light into wider angles and to a large extent from the side walls.

In Figure 4.28a the dipoles are spread randomly through the cube. The resulting far-field has a relatively uniform intensity distribution, with a slightly higher intensity area in the centre of the field. This indicates that the emission is exiting all surfaces of the cube quite evenly. A slightly higher emission intensity from the centre of the field could be because the monitor is positioned closer to the top surface than the side walls.

The symmetry of the field is also here affected by the position of the dipoles. The non-symmetric

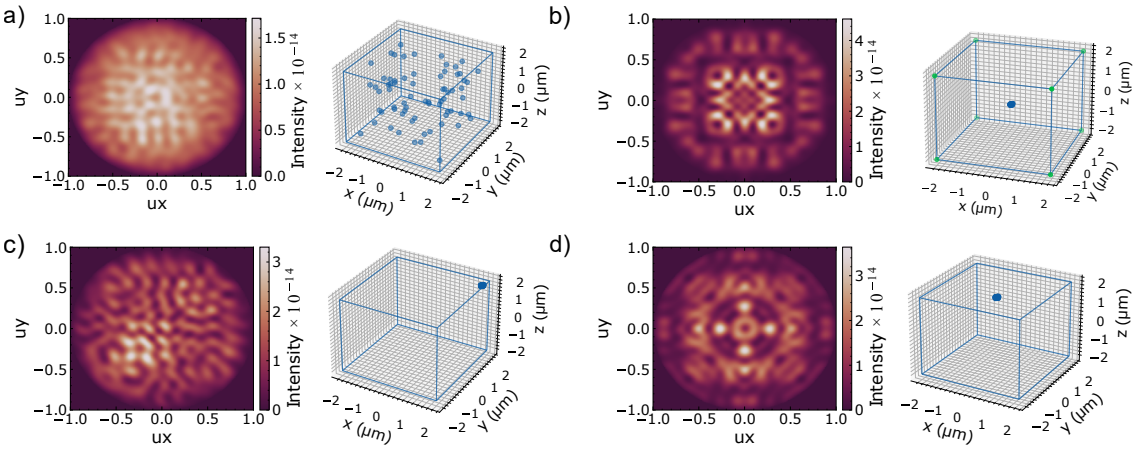

Figure 4.28: Far-field intensity from a cube of 4 µm with 70 dipoles positioned randomly (a) throughout the whole structure, (b) the centre, (c) in a corner and (d) just below the top surface.

positioning of the dipoles leads to a non-symmetric emission in the far-field, which is the case in Figures 4.28a and 4.28c. The resulting field when placing the dipoles in the corner (c) is similar to the one in (a), but the highest intensity area is shifted towards the opposite corner (bottom left).

Positioning the dipoles in the centre of the cube, such as in Figure 4.28b and 4.28d, the far-fields appear symmetric, with the emission concentrated towards the centre of the field. More so when the dipoles are positioned at the centre rather than close to the top surface. The maximum intensity emission from the dipoles in the centre of the cube is slightly higher ($\sim 4.5 \times 10^{-14}$) compared to when the dipoles are placed close to the top surface ($\sim 3.5 \times 10^{-14}$).

When positioning the dipoles close to the top surface, the maximum intensity seems to originate from four points close to the centre of the field. There also seems to be an overall high-intensity emission surrounding these bright points, before the intensity decreases closer to the edge of the field. A careful study reveals that the bright area enclosing the four high-intensity points has a squared shape. Indicating that the emission could be exiting from the top surface. The intensity is lower than the four bright points, indicating that the emission is directed outwards (away from the surface normal). The low-intensity emission in the far-field enclosing the square is therefore likely to be light exiting from the sides of the cube.

The emission from the dipoles in the centre of the cube is slightly more concentrated in a square area in the centre of the field. The area surrounding this squared area has a lower intensity. It could be that the squared shape in the far-field originates from the shape of the cube and that the area surrounding the square in the field is the emission from the sidewalls of the cube. Compared to the particles situated close to the top surface, the emission herein has a longer path before exiting the structure. This could explain the different emission patterns of the two dipole orientations.

The plots in Figure 4.29 show the electromagnetic fields in the far-field from the **spherical** structure with different positioning of the 70 dipoles (blue dots) with randomized phases. In (a) the dipoles are spread randomly in the structure and (b) the dipoles are centred in the centre of the structure, while in (c) the dipoles are positioned closer to the edge at approximately (x = 0, y = 1.9 and z = 0) of the particle. Here the intensity from the fields ranges from $\sim 2.5 \times 10^{-14} - 16 \times 10^{-14}$ where the intensity from the concentrated dipoles is the lowest, both at $\sim 2.5 \times 10^{-14}$ and highest when

the dipoles are distributed evenly in the particle.

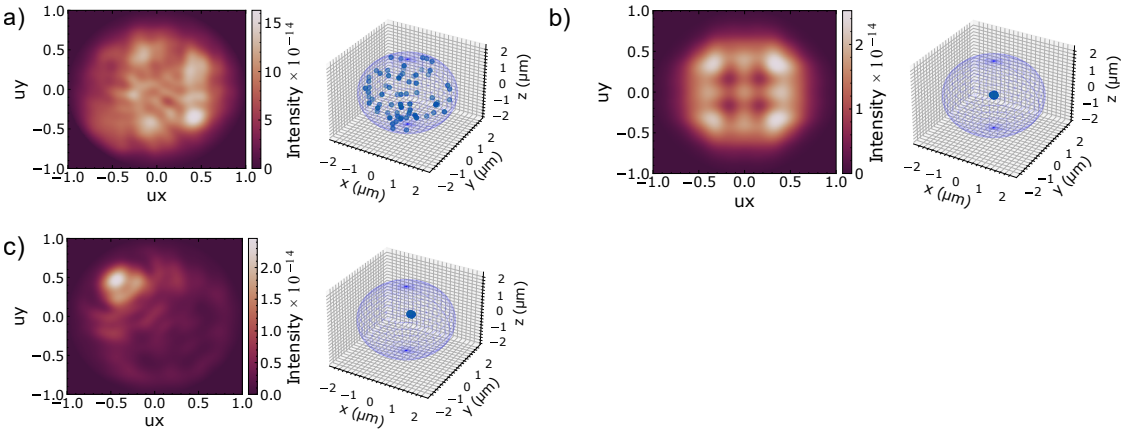

Figure 4.29: Far-field intensity from a sphere of 4 µm with 70 dipoles positioned randomly (a) throughout the whole structure, (b) the centre, (c) point outside of centre

When the dipoles are evenly distributed through the structure, the resulting electromagnetic field observed in the far-field is spherically shaped with certain higher intensity regions. The reason is not obvious, but it could be because of the internal scattering of the waves and interference. The relative size of the emitted wavelength and the particle may also have contributed to the result.

As observed in both the pyramidal and cubic structure, the field in Figure 4.29b has a four-fold symmetry when the dipoles are placed in symmetric positions. The symmetry is observed by four high-intensity points in the corners of a slightly rounded rectangle. There seems to be a lower intensity cross-like pattern between these four symmetry points. A careful study of the field in the same figure reveals a slightly higher intensity field in the two rightmost (ux $\approx$ 0.5) bright symmetry points which could be explained by an asymmetric distribution of the dipoles within the concentrated region.

Moving the dipoles out of the symmetric position, shown in Figure 4.29c, yields a higher intensity region in the top left corner of the field. Similar tendencies are observed in both the pyramidal and cubic particles (most evident in Figure 4.27b and 4.28c for the pyramid and cube, respectively). The observations from the simulations indicate that the geometry of the particle influences the emission to a higher extent than the positioning of the defects. This is especially observed in the pyramidal particle in Figure 4.27, where the strongest emission originated from the tip of the pyramid independently of the positioning of the defect. The highest intensity emission is observed when the particles are distributed evenly in all the structures, the pyramid, the cube and the sphere. Changing the position of the defects only alters the fields slightly, more so in the spherical particle compared to the pyramid and the cube.

The maximum intensity difference between the cube and pyramid is significant, where the only difference in the simulation is the geometry of the particle. The difference in maximum intensity between the pyramid and spherical is significantly less. Hence the shape of the particle could be directing light through internal reflections in a specific direction, here in the z-direction. This strengthens the observation of the position-dependent emission from the silicon-vacancy from the pyramidal particle studied with CL in section 4.3.3.

Emission from a flat surface is to a larger extent spread outwards (ux, uy directions), indicated by the simulated fields from the cubic particle. The emission intensity is observed to vary across the surface of the particle, which is the case in the rectangle-shaped particle studied with CL in section 4.3.3 Figure 5.11. Also here, there is a slight difference in the fields when changing the position of the dipoles. However, the emission from the cube is overall spread out.

It seems that the depth at which the defects are positioned influences the emission intensity, seen when comparing defects at the surface/tip of a structure compared to when placed in the centre. This could indicate that thin SiC particles would emit less light, which was also pointed out in section 4.3.3.

The absolute intensity will in this work not be compared to experimental results as the simulations are highly simplified.

4.4.3 Particle Size Dependence

The far-fields in Figure 4.30 show the result of running simulations with one dipole centred in the middle of each structure (sphere, pyramid, cube). Note that the wavelength of these simulations was set to 918 nm. This is also indicated in the caption of the figure. Herein we have also included particles of different sizes. The leftmost field is from a 2 µm sized particle, the middle and rightmost originate from 4 and 5 µm particles, respectively. This simulation essentially tries to mimic a simplified, ideal case of a quantum repeater, where flying qubits can be enhanced by careful positioning of the defect within a host without destroying the entanglement.

The far-fields from these simulations are highly symmetric, which is not a surprise as the simulation is set up symmetrically. The interference pattern could be explained by internal reflections. The intensity of the smaller particles (2 µm in the leftmost figures) is higher compared to the larger (4 and 5 µm) structures. The maximum field intensity from the cube ($\sim 6.5 \times 10^{-12}$) is significantly higher then from that of the sphere ($\sim 0.125 \times 10^{-12}$) and pyramid ($\sim 2 \times 10^{-12}$). Especially from the smallest structure (to the far left). Compared to the simulation, the intensity here is $\sim$ two orders of magnitude higher, likely because of the different wavelength used in the simulations or partly because of a larger degree of destructive interference in the many-dipole case. The field from the pyramid is certainly more concentrated around the centre of the hemisphere, compared to the sphere and cube. The pyramid to the largest extent directs the light in the upward direction, indicated by the smaller area from where emission is detected, which is desirable for quantum repeaters in optical fibres. However, the "hole" in the centre of the field indicates that the light is spread slightly, and hence optimization of the geometry or possibly careful positioning (orientation of the particle) is required to ensure that the light is directed in the z-direction.

The emission from the cubic and spherical structures seems to, to a greater extent, be spread in the ux, uy plane (outwards) with some higher intensity points or regions. Such properties might be useful in future applications, but further work will then be necessary.

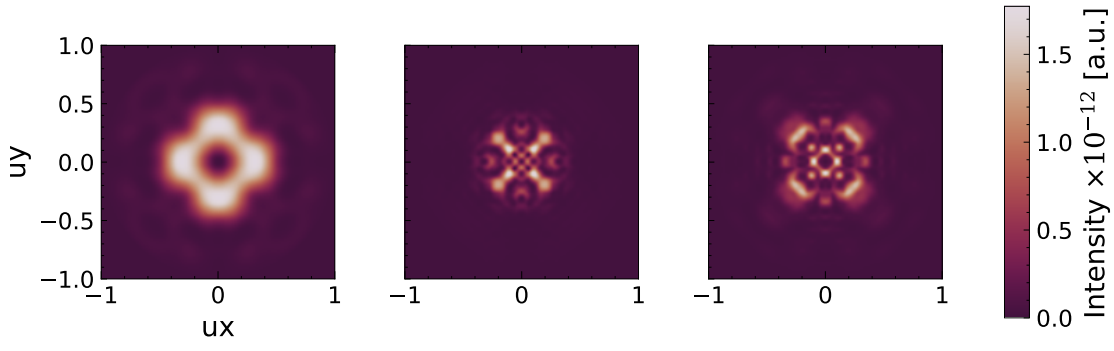

(a) Pyramid

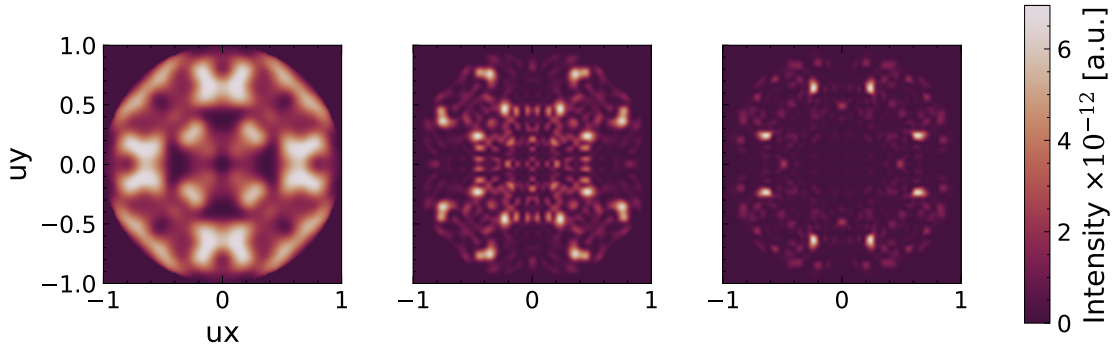

(b) Cube

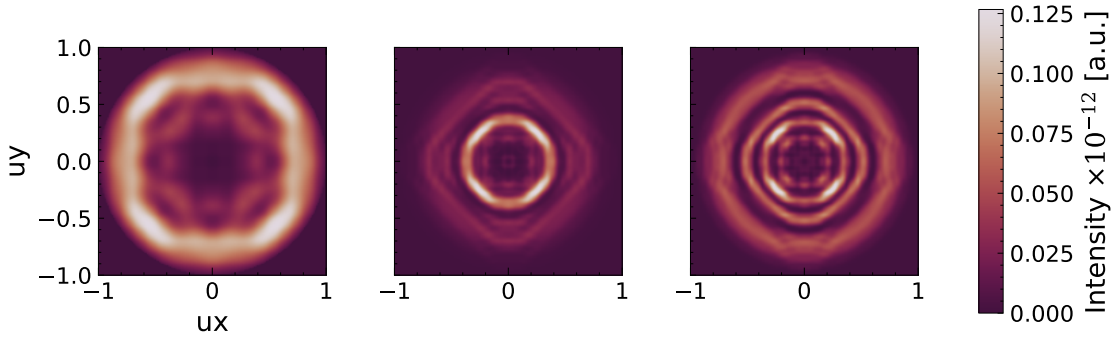

(c) Sphere

Figure 4.30: Far field projection intensity ($\times 10^{-12}$) from (a) pyramid (b) cube and (c) spherical structure of increasing size from left to right (2 , 4 and 5µm). Wavelength = 918 nm.

Chapter 5

Concluding Remarks

5.1 Conclusion

In this work, progress has been made in understanding the luminescence from defects introduced into SiC particles. Importantly, by combining optical spectroscopy with numerical simulations of electromagnetic fields, we find that the shape of the particle may influence the measured emission from the particles, as well as the distribution of the defects. Interestingly, defects positioned deep in the particle may sometimes promote higher intensity emission. Observed with both CL spectroscopy and FDTD simulations, triangled/pyramidal particles yield higher intensity and, to a greater extent, directional emission compared to the cubic, spherical and other arbitrary geometries.

PL and CL spectroscopy revealed a wide range of identified and unidentified emitters in the SiC powder. The silicon vacancy was present as both ZPLs and PSB in most particles, and after the 1000° anneal, a narrowing of the ZPLs occurred. More interesting is the yet unidentified feature located at ~ 970 nm observed in both PL and CL, most prominent in the former. The emission may originate from two separate defect centres with overlapping emission energies based on both intrinsic and extrinsic behaviour.

5.2 Future work

This work has focused on the optical characterization of colour centres in SiC and broadening the understanding of the emission from the SiC particles. The extent of emission centres limited the investigations to an overview of the present colour centres. Further work is necessary to identify SPEs and exclude features originating from PSBs. A summary of elements which can be of interest for further investigations include, but are not limited to:

- Optimization of particle geometries for enhanced directional emission for quantum communication applications.
- Pursue further analysis of PL and CL spectra, by for example Gaussian peak fitting, and identification of unknown emitters to identify potential qubit candidates.
- Full dose and annealing series studies of the SiC particles.
- Implement a more realistic simulation environment by. e.g. implementing rough surface

structures and use SEM images to make the shapes of the simulated and actual particles more alike.

- Eventually make a prototype of SiC particles embedded in an optical fibre.

Bibliography

[1] G. E. Moore, "Cramming more components onto integrated circuits," *IEEE Solid-State Circuits Society Newsletter*, vol. 11, pp. 33–35, Sept. 2006.

[2] IBM, "IBM unveils world's first 2 Nanometer Chip Technology, Opening a New Frontier for Semiconductors." `https://newsroom.ibm.com/2021-05-06-IBM-Unveils-Worlds-First-2-Nanometer-Chip-Technology,-Opening-a-New-Frontier-for-Semiconductors`, May 2021. (Accessed on 04/19/2022).

[3] G. E. Moore, "Quantum computing with defects," *MRS Bulletin*, vol. 38, pp. 802–808, 10 2013.

[4] D. P. DiVincenzo and IBM, "The Physical Implementation of Quantum Computation," *Protein Science*, vol. 48, pp. 771–783, 2000.

[5] T. D. Ladd, F. Jelezko, R. Laflamme, Y. Nakamura, C. Monroe, and J. L. O'Brien, "Quantum computers," *Nature*, vol. 464, pp. 45–53, Mar. 2010.

[6] IBM, "IBM's roadmap for scaling quantum technology — IBM Research Blog." `https://research.ibm.com/blog/ibm-quantum-roadmap`, Sep 2020. (Accessed on 04/19/2022).

[7] A. Acín, I. Bloch, H. Buhrman, T. Calarco, C. Eichler, J. Eisert, D. Esteve, N. Gisin, S. J. Glaser, F. Jelezko, S. Kuhr, M. Lewenstein, M. F. Riedel, P. O. Schmidt, R. Thew, A. Wallraff, I. Walmsley, and F. K. Wilhelm, "The quantum technologies roadmap: a European community view," *New Journal of Physics*, vol. 20, p. 080201, Aug. 2018.

[8] C. Degen, F. Reinhard, and P. Cappellaro, "Quantum sensing," *Reviews of Modern Physics*, vol. 89, pp. 2–3, jul 2017.

[9] Q. Flagship, "Quantum Technologies in a nutshell - Quantum Technology." `https://qt.eu/discover-quantum/quantum-technologies-in-a-nutshell/`. (Accessed on 04/20/2022).

[10] C. H. Bennett and G. Brassard, "Quantum cryptography: Public key distribution and coin tossing," *Theoretical Computer Science*, vol. 560, pp. 7–11, Dec. 2014.

[11] O. Golfreich, *Foundations of Cryptography: Volume 1, Basic Tools*. Cambridge: Cambridge University Press, 2001.

[12] M. E. Bathen and L. Vines, "Manipulating single-photon emission from point defects in diamond and silicon carbide," *Advanced Quantum Technologies*, vol. 4, p. 2100003, May 2021.

[13] B. G. Streetman, *Solid state electronic devices / Ben G. Streetman and Sanjay Banerjee*. Prentice Hall series in solid state physical electronics, Upper Saddle River, N.J: Prentice Hall, 5th ed. ed., 2000.

[14] I. Pelant and J. Valenta, *Luminescence Spectroscopy of Semiconductors*, ch. 4 and 6, pp. 112–116 and 451–452. Oxford University Press, Feb. 2012.

[15] I. Aharonovich, D. Englund, and M. Toth, "Solid-state single-photon emitters," *Nature Photonics*, vol. 10, pp. 631–641, 10 2016.

[16] S. E. Saddow and F. L. Via, eds., *Advanced Silicon Carbide Devices and Processing*. InTech, Sept. 2015.

[17] T. Kimoto and J. A. Cooper, *Fundamentals of Silicon Carbide Technology*. John Wiley & Sons Singapore Pte. Ltd, Sept. 2014.

[18] D. Y. Fedyanin, "Optoelectronics of color centers in diamond and silicon carbide: From single-photon luminescence to electrically controlled spin qubits," *Advanced Quantum Technologies*, vol. 4, p. 2100048, Aug. 2021.

[19] G. Harris and INSPEC (Information service), *Properties of Silicon Carbide*. EMIS datareviews series, INSPEC, Institution of Electrical Engineers, 1995.

[20] N. Iwamoto and B. G. Svensson, "Chapter Ten - Point Defects in Silicon Carbide," in *Defects in Semiconductors* (L. Romano, V. Privitera, and C. Jagadish, eds.), vol. 91 of *Semiconductors and Semimetals*, pp. 369–407, Elsevier, 2015.

[21] T. Kimoto, K. Kawahara, B. Zippelius, E. Saito, and J. Suda, "Control of carbon vacancy in SiC toward ultrahigh-voltage power devices," *Superlattices and Microstructures*, vol. 99, pp. 151–157, Nov. 2016.

[22] J. W. Steeds, "Photoluminescence study of the carbon antisite-vacancy pair in 4H - And 6H-SiC," *Physical Review B - Condensed Matter and Materials Physics*, vol. 80, 12 2009.

[23] S. Castelletto and A. Boretti, "Silicon carbide color centers for quantum applications," *Journal of Physics: Photonics*, vol. 2, p. 022001, mar 2020.

[24] N. T. Son, C. P. Anderson, A. Bourassa, K. C. Miao, C. Babin, M. Widmann, M. Niethammer, J. U. Hassan, N. Morioka, I. G. Ivanov, F. Kaiser, J. Wrachtrup, and D. D. Awschalom, "Developing silicon carbide for quantum spintronics," *Applied Physics Letters*, vol. 116, 5 2020.

[25] V. A. Soltamov and P. G. Baranov, "Radio spectroscopy of the optically aligned spin states of color centers in silicon carbide," *Uspekhi Fizicheskih Nauk*, vol. 186, pp. 678–684, 2016.

[26] A. Lohrmann, N. Iwamoto, Z. Bodrog, S. Castelletto, T. Ohshima, T. Karle, A. Gali, S. Prawer, J. McCallum, and B. Johnson, "Single-photon emitting diode in silicon carbide," *Nature Communications*, vol. 6, July 2015.

[27] M. Rühl, C. Ott, S. Götzinger, M. Krieger, and H. B. Weber, "Controlled generation of intrinsic near-infrared color centers in 4h-sic via proton irradiation and annealing," *Applied Physics Letters*, vol. 113, no. 12, p. 122102, 2018.

[28] M. Rühl, J. Lehmeyer, R. Nagy, M. Weisser, M. Bockstedte, M. Krieger, and H. B. Weber, "Removing the orientational degeneracy of the TS defect in 4H–SiC by electric fields and strain," *New Journal of Physics*, vol. 23, p. 073002, June 2021.

[29] W. F. Koehl, B. B. Buckley, F. J. Heremans, G. Calusine, and D. D. Awschalom, "Room temperature coherent control of defect spin qubits in silicon carbide," *Nature*, vol. 479, pp. 84–87, 11 2011.

[30] N. T. Son, E. Sörman, W. M. Chen, M. Singh, C. Hallin, O. Kordina, B. Monemar, E. Janzén, and J. L. Lindström, "Dominant recombination center in electron-irradiated 3C SiC," *Journal of Applied Physics*, vol. 79, pp. 3784–3786, 4 1996.

[31] G. Calusine, A. Politi, and D. D. Awschalom, "Cavity-Enhanced Measurements of Defect Spins in Silicon Carbide," *Physical Review Applied*, vol. 6, 7 2016.

[32] G. Calusine, A. Politi, and D. D. Awschalom, "Silicon carbide photonic crystal cavities with integrated color centers," *Applied Physics Letters*, vol. 105, 7 2014.

[33] A. H. Andreas Gällström, Björn Magnusson, "The Electronic Structure of the UD-4 Defect in 4H, 6H and 15R SiC," *Materials Science Forum*, vol. 600-603, pp. 397–400, 9 2008.

[34] K. Yee, "Numerical solution of initial boundary value problems involving maxwell's equations in isotropic media," *IEEE Transactions on Antennas and Propagation*, vol. 14, pp. 302–307, May 1966.

[35] A. Taflove and S. C. Hagness, *Computational Electrodynamics: The Finite-Differences Time-Domain Method*. Boston, London: Artech House, Inc., 3 ed., 2005.

[36] M. Radulaski, M. Widmann, M. Niethammer, J. L. Zhang, S.-Y. Lee, T. Rendler, K. G. Lagoudakis, N. T. Son, E. Janzén, T. Ohshima, J. Wrachtrup, and J. Vučković, "Scalable quantum photonics with single color centers in silicon carbide," *Nano Letters*, vol. 17, pp. 1782–1786, Feb. 2017.

[37] E. Sörman, N. Son, W. Chen, O. Kordina, C. Hallin, and E. Janzén, "Silicon vacancy related defect in 4H and 6H SiC," *Phys. Rev. B*, vol. 61, 01 2000.

[38] H. J. V. Bardeleben, J. L. Cantin, E. Rauls, and U. Gerstmann, "Identification and magneto-optical properties of the NV center in 4H-SiC," *Physical Review B - Condensed Matter and Materials Physics*, vol. 92, 8 2015.

[39] J. Mooney and P. Kambhampati, "Get the basics right: Jacobian conversion of wavelength and energy scales for quantitative analysis of emission spectra," *Journal of Physical Chemistry Letters*, vol. 4, pp. 3316–3318, 10 2013.

[40] J. Mooney and P. Kambhampati, "Correction to " Get the Basics Right: Jacobian Conversion of Wavelength and Energy Scales for Quantitative Analysis of Emission Spectra"," *The Journal of Physical Chemistry Letters*, vol. 5, pp. 3497–3497, Sept. 2014.

[41] T. H. Gfroerer, "Photoluminescence in Analysis of Surfaces and Interfaces," Sept. 2006.

[42] JEOL, "SEM : Scanning electron microscope A to Z." `https://www.jeol.co.jp/en/applications/pdf/sm/sem_atoz_all.pdf`.

[43] N. Erdman, D. C. Bell, and R. Reichelt, "Scanning Electron Microscopy," in *Springer Handbook of Microscopy*, pp. 229–318, Springer International Publishing, 2019.

[44] S. Wang, M. Zhan, G. Wang, H. Xuan, W. Zhang, C. Liu, C. Xu, Y. Liu, Z. Wei, and X. Chen, "4H-SiC: a new nonlinear material for midinfrared lasers," *Laser & Photonics Reviews*, vol. 7, pp. 831–838, July 2013.

[45] P. T. B. Shaffer, "Refractive Index, Dispersion, and Birefringence of Silicon Carbide Polytypes," *Applied Optics*, vol. 10, p. 1034, May 1971.

[46] G. C. Vásquez, M. E. Bathen, A. Galeckas, C. Bazioti, K. M. Johansen, D. Maestre, A. Cremades, Prytz, A. M. Moe, A. Y. Kuznetsov, and L. Vines, "Strain Modulation of Si Vacancy Emission from SiC Micro- And Nanoparticles," *Nano Letters*, vol. 20, pp. 8689–8695, 12 2020.

[47] Y. Wei, A. T. Tarekegne, and H. Ou, "Double D-centers related donor-acceptor-pairs emission in fluorescent silicon carbide," *Optical Materials Express*, vol. 9, p. 295, 1 2019.

[48] J. R. Dietz and E. L. Hu, "Optical and Strain Stabilization of Point Defects in Silicon Carbide," 2022.

[49] J. Schneider and K. Maier, "Point defects in silicon carbide," *Physica B: Condensed Matter*, vol. 185, pp. 199–206, Apr. 1993.

Appendix A

5.3 Lumerical script files

This is a semi-pseudo with a mix of python code and the Lumerical scripting language(starting with 'fdtd.'. Many variables are self-explanatory, but some description is given as python comments. However, more information is found at the Lumerical webpage, the provider of the software : Lumerical scripting language.

5.3.1 Simulation environment

This algorithm/psudocode shows the frame/basis for simulation region setups for the experiments.

```
#imports
import numpy as np
import matplotlib.pyplot as plt
import os, sys
import random
import pandas as pd

#imports for running lumerical through python scripts
spec_win = importlib.util.spec_from_file_location('lumapi',
'C:\\Program Files\\Lumerical\\v212\\api\\python\\lumapi.py')
lumapi = importlib.util.module_from_spec(spec_win)
spec_win.loader.exec_module(lumapi)

#Initilize the lumerical software
fdtd = lumapi.FDTD(hide = True)
fdtd.switchtolayout()

#add simulation region with boundary condition
fdtd.addfdtd()

#set position of the simulation region in origo
fdtd.set('x', x ); fdtd.set('y', y); fdtd.set('z', z)

#Set the size of the simulation region.
fdtd.set('x span', XSpan); fdtd.set('y span', YSpan); fdtd.set('z span', ZSpan)

#Add meshing based on structure to increase mesh
#around the edges of the structure
fdtd.addmesh()
fdtd.set('based on a structure', True)

#mesh position
fdtd.set('x', x ); fdtd.set('y', y); fdtd.set('z', z)

#Size of mesh region
```

```
fdtd.set('x span', XSpan); fdtd.set('y span', YSpan); fdtd.set('z span', ZSpan)

#Size of mesh cells
fdtd.set('dx', dx) ;fdtd.set('dy', dy); fdtd.set('dz', dz)

#Adding a Transmission monitor in the z plane above the structure
fdtd.addpower()
fdtd.set('name', 'Transmission')
fdtd.set('monitor type', '2D Z-normal')
fdtd.set('x', 0); fdtd.set('y', 0); fdtd.set('z', monitor_position)
fdtd.set('x span', monitor_size_x); fdtd.set('y span', monitor_size_y)

#Set the number of frequency/wavelength points to calculate
fdtd.setglobalmonitor("frequency points",11)

#add a dipole source (modelling a quantum dot/defect)
#source of emission
settings to imitate a quantum dot
fdtd.adddipole()
fdtd.set('name', 'QD')

fdtd.set('x', x); fdtd.set('y', y); fdtd.set('z', z)

#angle of the source
fdtd.set('theta', theta)

#choosing the simulation to be one WL.
#Can be chosen to be a span with some center, or a range between min and max.
fdtd.set('center wavelength', WL)
fdtd.set('wavelength span', 0)

#optimize for short pulse to be as similar as a dipole/QD source as possible
fdtd.set('optimize for short pulse', 0)

#add structures
fdtd.addsphere(); name = 'sphere'
fdtd.set("radius",R/2)

#or
fdtd.addrect(); name = 'rectangle'
fdtd.set("x span",XSpan); fdtd.set("y span",YSpan); fdtd.set("z span",ZSpan)

#or
fdtd.addpyramid(); name = 'pyramid'

#make the top very pointy, but not zero
fdtd.set("x span top", 1e-09) ; fdtd.set("y span top",1e-09)

fdtd.set("x span bottom",XSpanBottom); fdtd.set("y span bottom",YSpanBotom)
fdtd.set("z span", height)

fdtd.set("name", name)

#position, usually in origo
fdtd.set('x', x); fdtd.set('y', y); fdtd.set('z', z)

#Set the refractive index of the material.
#It is also possible to add a refractive index vs. wavelength
#file yielding electromagnetic fields as a function of wavelengths.

fdtd.set('index', 2.6)
```

```
97
98  #save the lumerical simulation file
99  fdtd.save(FILENAME_FDTD)
100
101 #Some looped simulation(e.g. particle size, polytype, number of dipoles etc)
102 for i in list_of_simulations:
103     #do some changes
104
105     #running the simulation
106     fdtd.run()
```

5.3.2 Random Positioning of emitter

As described in the method section/ method development for Lumerical section, dipole sources/QD/defects were randomly positioned within the structure one bye one. Hence having 100 dipoles means having 100 simulations with 1 dipole in each. The resulting fields were summed together and divided by the number of dipoles. This is how it was implemented in the code/simulation.

```
1   SEED = 2022
2   n = 1
3
4   #itering over e.g. particle size or polytypes listed in "iter_list"
5
6   for i in range(len(iter_list)):
7       if STRUCT == 'rectangle':
8           x,y,z  = PointsInsideRectangle(n, SIZE, SEED)
9       if STRUCT == 'sphere':
10          R = SIZE/2
11          x,y,z =  PointsInsideSphere(n, (0,0,0), R, SEED)
12      if STRUCT == 'pyramid':
13              x,y,z = PointsInsidePyramid(n, SIZE, SIZE, SEED)
14  SEED += 1
15      fdtd.select('QD')
16      fdtd.set('x',x); fdtd.set('y',y); fdtd.set('z', z)
17
18      #randomizing the angle of the dipole to
19      #replicate the situation in the particles
20      #(randomly oriented because the particles are randomly organized)
21      phase = np.random.uniform(0, 360);  fdtd.set('phase',phase)
22      phi = np.random.uniform(0, 180);    fdtd.set('phi', phi)
23      theta = np.random.uniform(0, 360);  fdtd.set('theta', theta
24
25  #functions for getting the points within the structures, using simple geometry
26  def PointsInsideSphere(center, radius:float, SEED:int, n = 1):
27
28      random.seed(SEED)
29      phi         = np.random.uniform(0, 2*np.pi, size = (n,))
30      theta_cos   = np.random.uniform(-1,1 , size = (n,))
31      u           = np.random.uniform(0,1, size = (n,))
32
33      theta_sin   = np.sqrt(1-theta_cos**2)
34      r = radius* np.cbrt(u)
35
36      points = np.array([
37          np.array([
38              center[0] + r[i] * theta_sin[i] * np.cos(phi[i]),
39              center[1] + r[i] * theta_sin[i] * np.sin(phi[i]),
40              center[2] + r[i] * theta_cos[i]
```

```
        ]) for i in range(n)
    ])

    x = points[:,0]; y = points[:,1]; z = points[:,2]
    return x, y, z


def PointsInsidePyramid(SIZE:float, height:float, SEED:int, n = 1):

    O = np.array([0,0,0])
    T = np.array([0, 0, height/2])
    A = np.array([SIZE/2, SIZE/2, -height/2])
    B = np.array([-SIZE/2, SIZE/2, -height/2])
    C = np.array([-SIZE/2,  -SIZE/2, -height/2])
    D = np.array([SIZE/2,  -SIZE/2, -height/2])

    points_pyr = np.array([A,B,C,D,T,O])
    x = points_pyr[:,0]; y = points_pyr[:,1]; z = points_pyr[:,2]

    #planes
    ABT = [A, B, T]; ACT = [A, D, T]; CBT = [C, B, T]
    CDT = [C, D, T]; ABCD = [A,B,C,D]

    planes = [ABT, ACT, CBT, CDT, ABCD]

    #plane normals
    NABT = np.cross(B - T, A - T)  ; NADT = np.cross(A - T, D - T)
    NCBT = np.cross(D - T, C - T)  ; NCDT = np.cross(C - T, B - T)
    NABC = np.cross(A - D, B - D)


    point_inside = False
    x_list, y_list, z_list = [], [], []
    random.seed(SEED)

    for i in range(n):
        while point_inside == False:

            x = np.random.uniform(-SIZE/2, SIZE/2, size = (n,))*0.95
            y = np.random.uniform(-SIZE/2, SIZE/2, size = (n,))*0.95
            z = np.random.uniform(-SIZE/2, SIZE/2, size = (n,))*0.95

            x = x[0]; y = y[0]; z= z[0]

            point = x,y,z

            dir_vec_1 = point - T
            dir_vec_2 = point - B

            r1 = np.dot(dir_vec_1, NABT); r2 = np.dot(dir_vec_1, NADT)
            r3 = np.dot(dir_vec_1, NCBT); r4 = np.dot(dir_vec_1, NCDT)
            r5 = np.dot(dir_vec_2, NABC)

            list = [r1, r2, r3, r4, r5]

            point_inside = all(j > 0 for j in list)

        x_list.append(x); y_list.append(y), z_list.append(z)

    return x_list, y_list, z_list

```

```
def PointsInsideRectangle(SIZE:float, SEED:int, n = 1):
    x, y, z = np.zeros(n), np.zeros(n), np.zeros(n)
    np.random.seed(SEED)
    for i in range(n):
        x[i] = np.random.uniform(-SIZE/2, SIZE/2, size = (1,))*0.95
        y[i] = np.random.uniform(-SIZE/2, SIZE/2, size = (1,))*0.95
        z[i] = np.random.uniform(-SIZE/2, SIZE/2, size = (1,))*0.95

    return x,y,z
```

5.3.3 Result Acquisition

```
T = fdtd.getresult('Transmission', 'T'); transm = T['T']
P = fdtd.getresult('QD','purcell'); purcell_fac = P['purcell']
E = fdtd.getresult('Transmission', 'E')
x =  fdtd.getresult('Transmission', 'x')
y = fdtd.getresult('Transmission', 'y')
FF = fdtd.farfield3d('Transmission');
ux = fdtd.farfieldux('Transmission');
uy = fdtd.farfielduy('Transmission')

#Save data to .npy files for fast reading/writing of files.
```

5.4 Lumerical Convergence Test Results

Herein, the results not included in the Simulation Result and discussion section (sec. 3.3.3) is included.

5.4.1 Sphere

Boundary condition

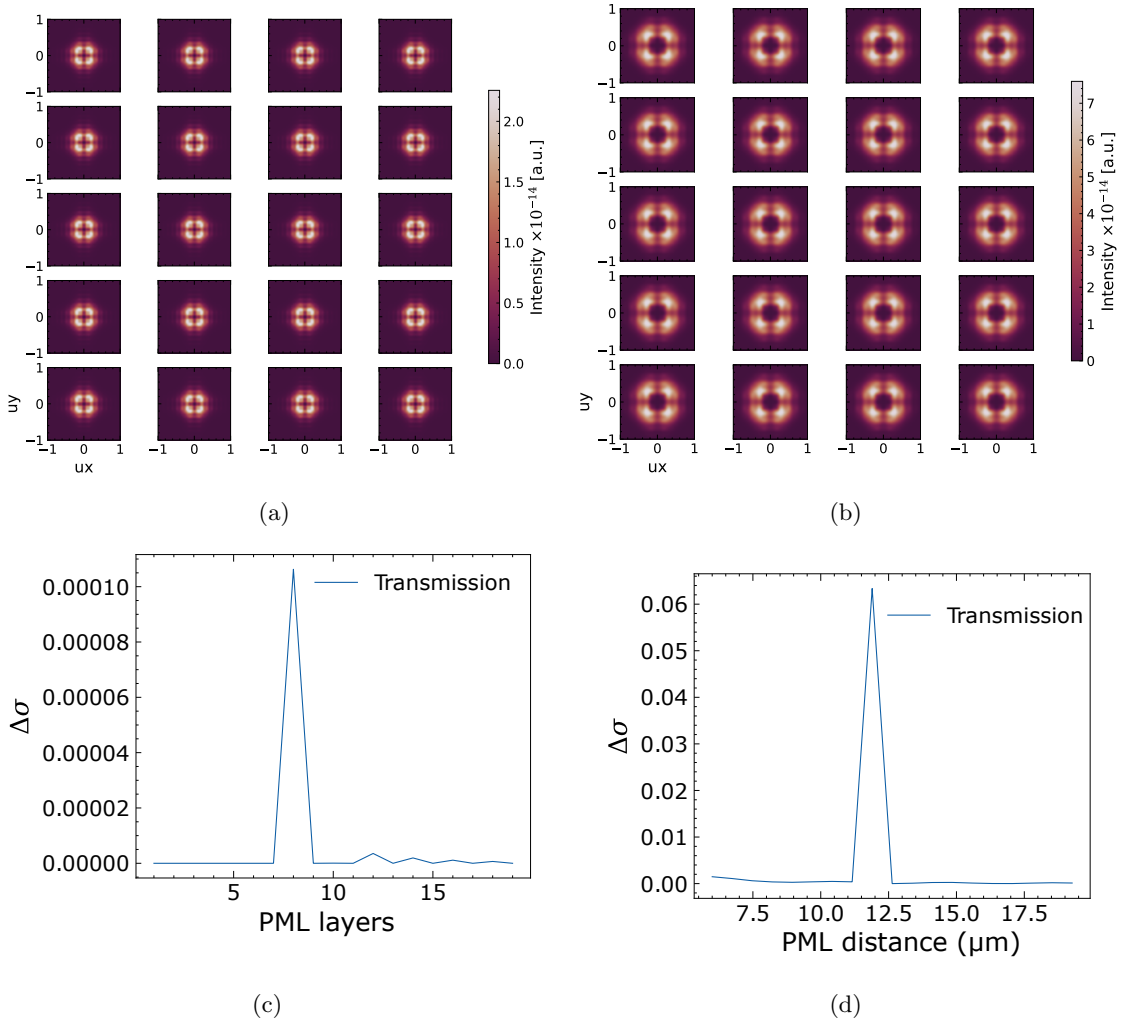

Figure 5.1: Convergence tests of a sphere with a diameter of 2 µm. Farfield intensity. Run with mesh accuracy 3. a) number of PML layers and b) The size of the PML. Herein, PML span (in positive and negative x,y,z directions) of 2.5 - 12 µm.

Monitors

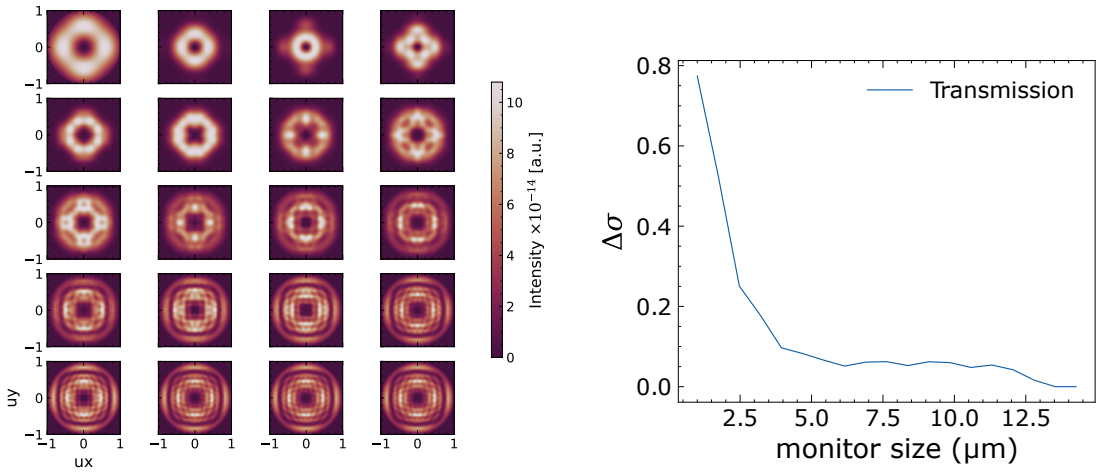

(a) (b)

Figure 5.2: Convergence tests of a 2 µm sphere. Mesh accuracy 3. 6 x 6 x 6 µm sized PML with 8 layers. a) Farfield intensity ($\times 10^{-14}$) and b) transmission of from monitor sizes from 1 - 6 µm

Mesh

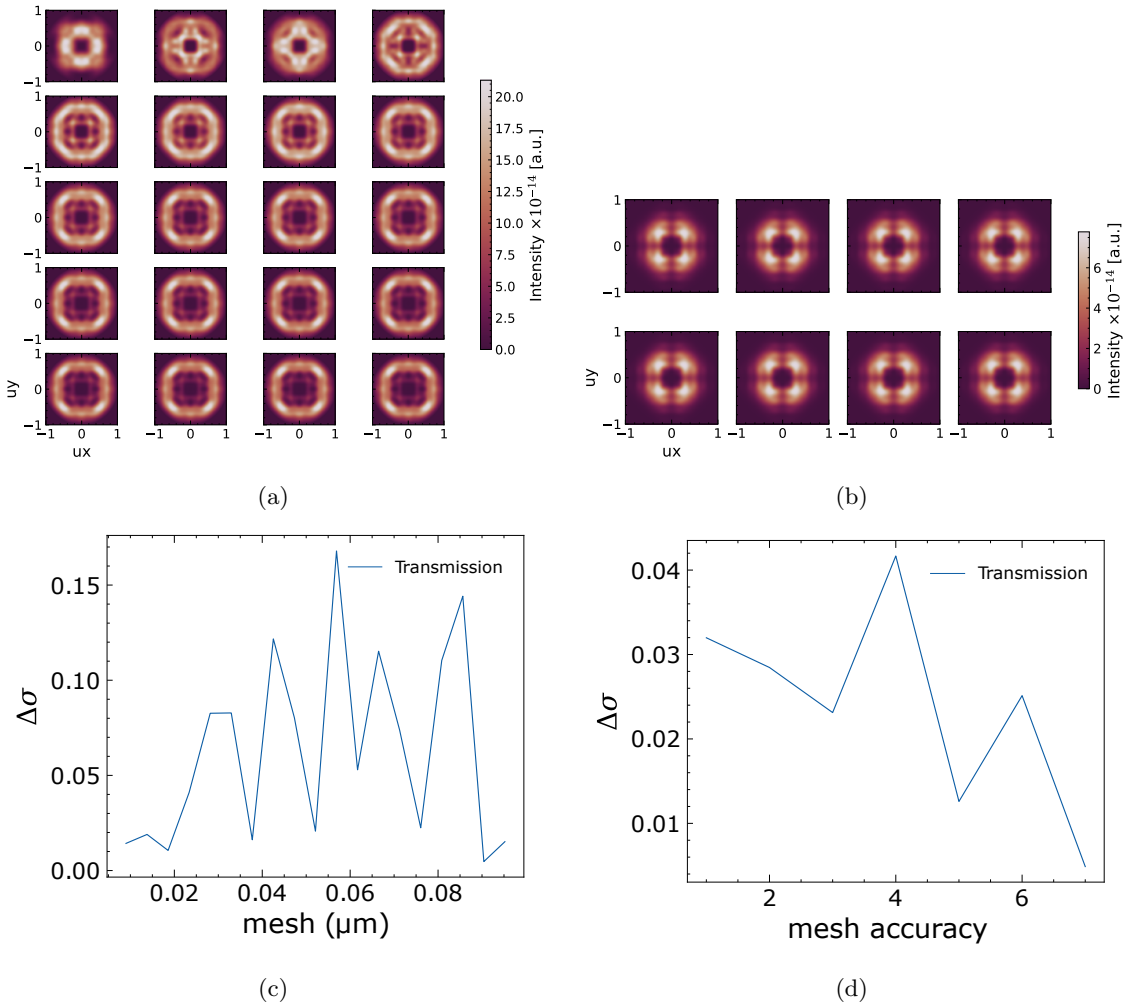

Figure 5.3: Convergence tests of a 2 µm sphere. Farfield intensity ($\times 10^{-14}$). a) mesh override region of mesh cells of size $0.1 - 0.009$ µm and b) mesh accuracy 1-8. Convergence test of transmission versus c) mesh override region and d) the mesh accuracy.

Dipoles

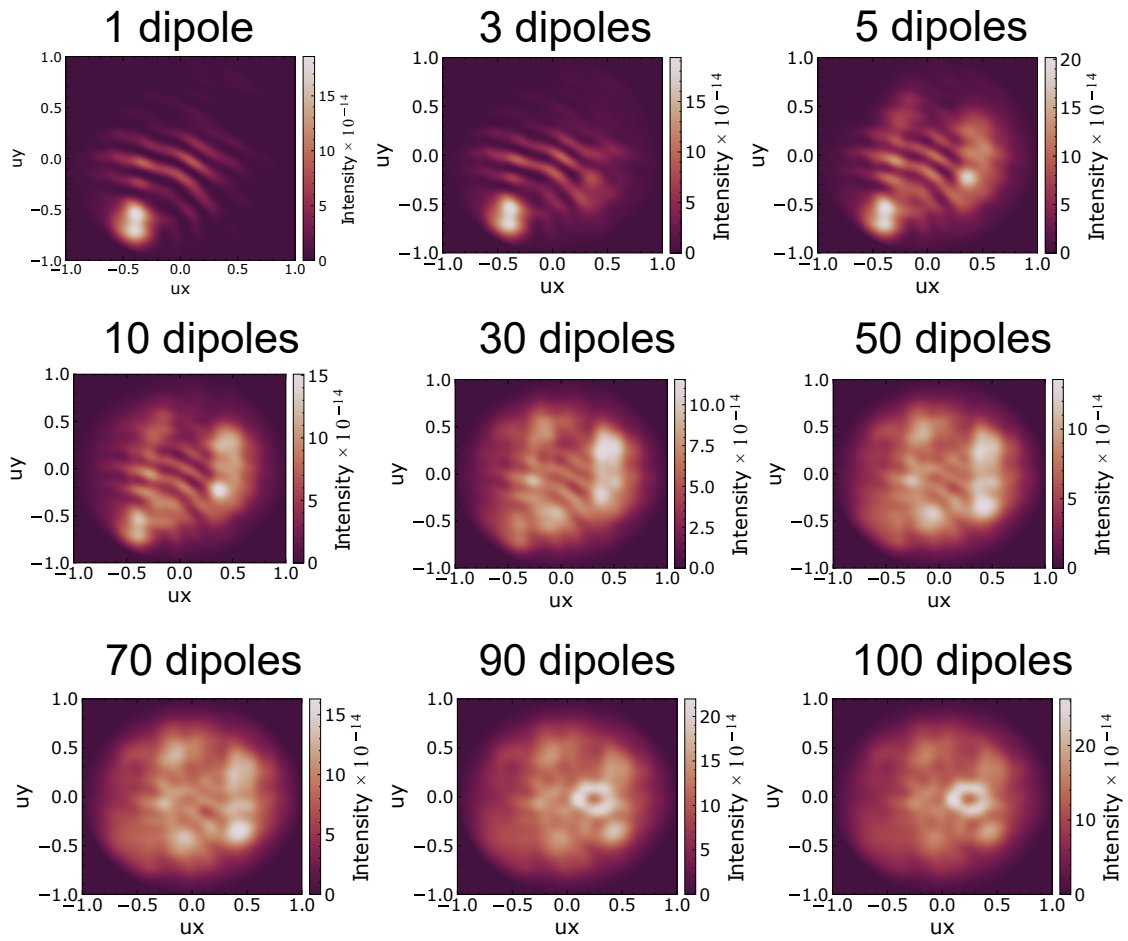

Figure 5.4: Convergence tests of the far-field intensity **number of dipoles** of a 2 µm sphere. Mesh accuracy 3. 6 x 6 x 6 µm sized PML with 8 layers.

5.4.2 Cube

Boundary condition

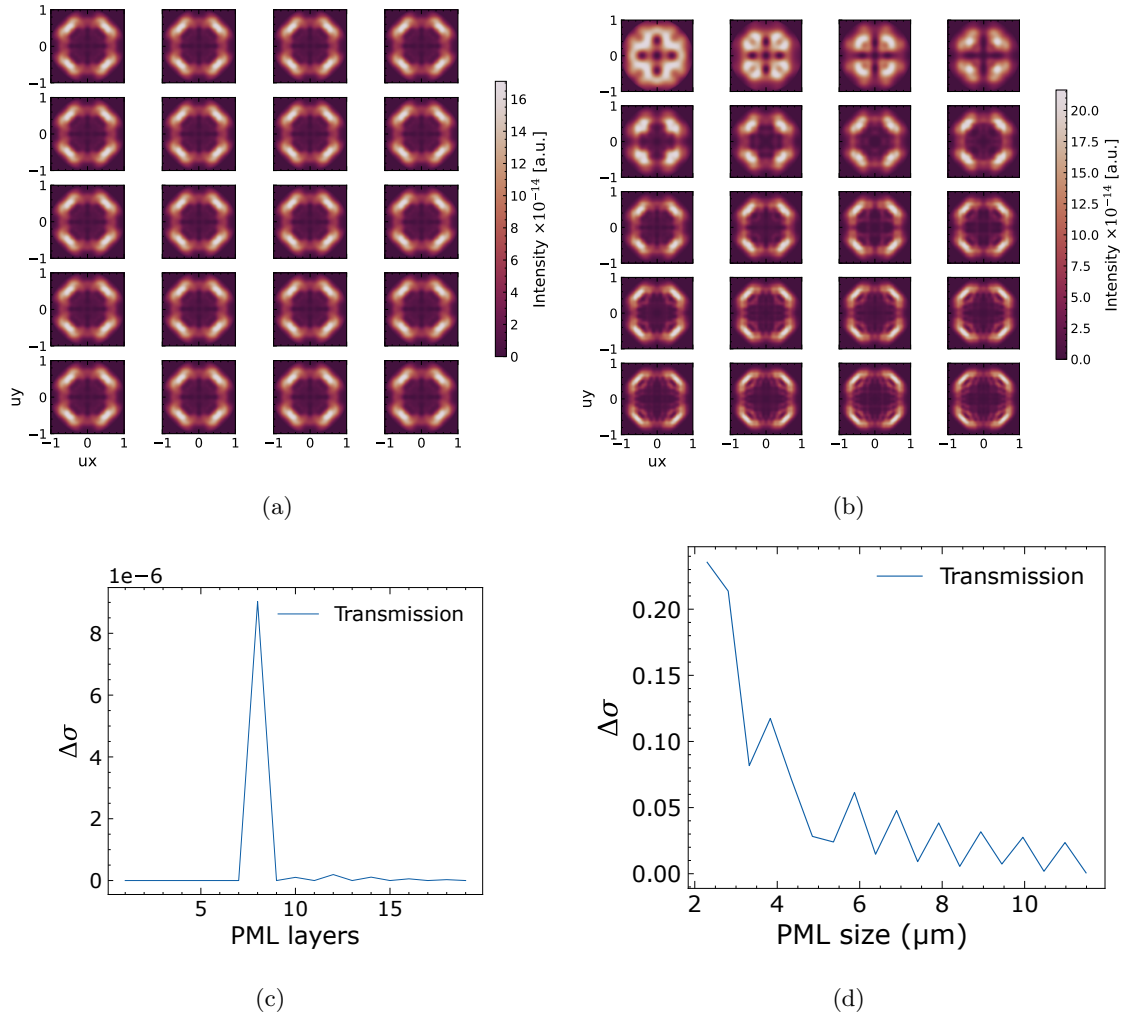

Figure 5.5: Convergence tests of a 2 µm cube. Farfield intensity. Run with mesh accuracy 3. a) number of PML layers and b) The size of the PML. Herein, PML span (in positive and negative x,y,z directions) for 2.5, 4.5, 5.0 and 6.0 µm (starting upper left) is presented as there is no difference of significance between PML size of 6.0 µm - 12 µm. For completeness a more comprehensive selection is shown in Appendix A section 5.4

Monitors

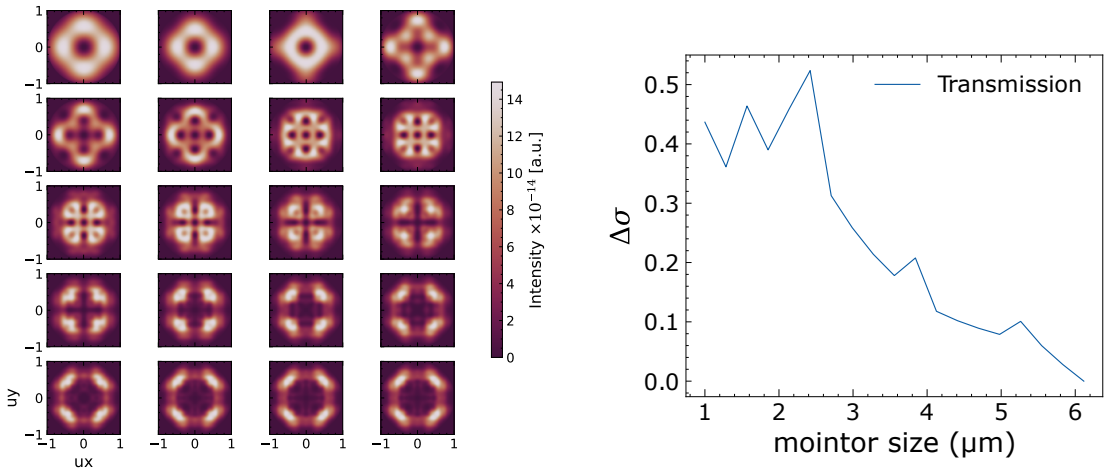

(a) (b)

Figure 5.6: Convergence tests of a 2 µm rectangle. Mesh accuracy 3. 6 x 6 x 6 µm sized PML with 8 layers. a) Farfield intensity ($\times 10^{-14}$) and b) transmission of from monitor sizes from 1 - 6 µm

Meshing

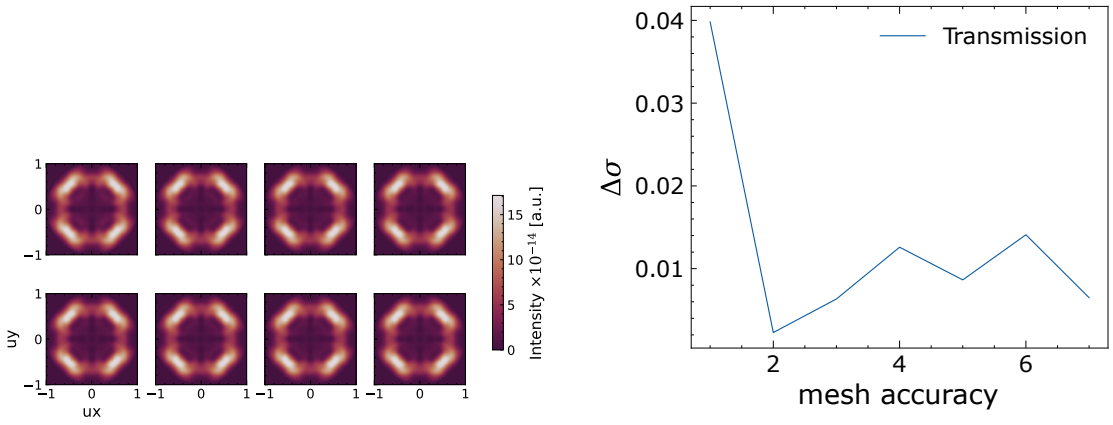

(a) (b)

Figure 5.7: Convergence tests of a 2 µm rectangle. Farfield intensity ($\times 10^{-14}$). a) mesh accuracy 1-8. Convergence test of transmission versus b) the mesh accuracy.

Dipoles

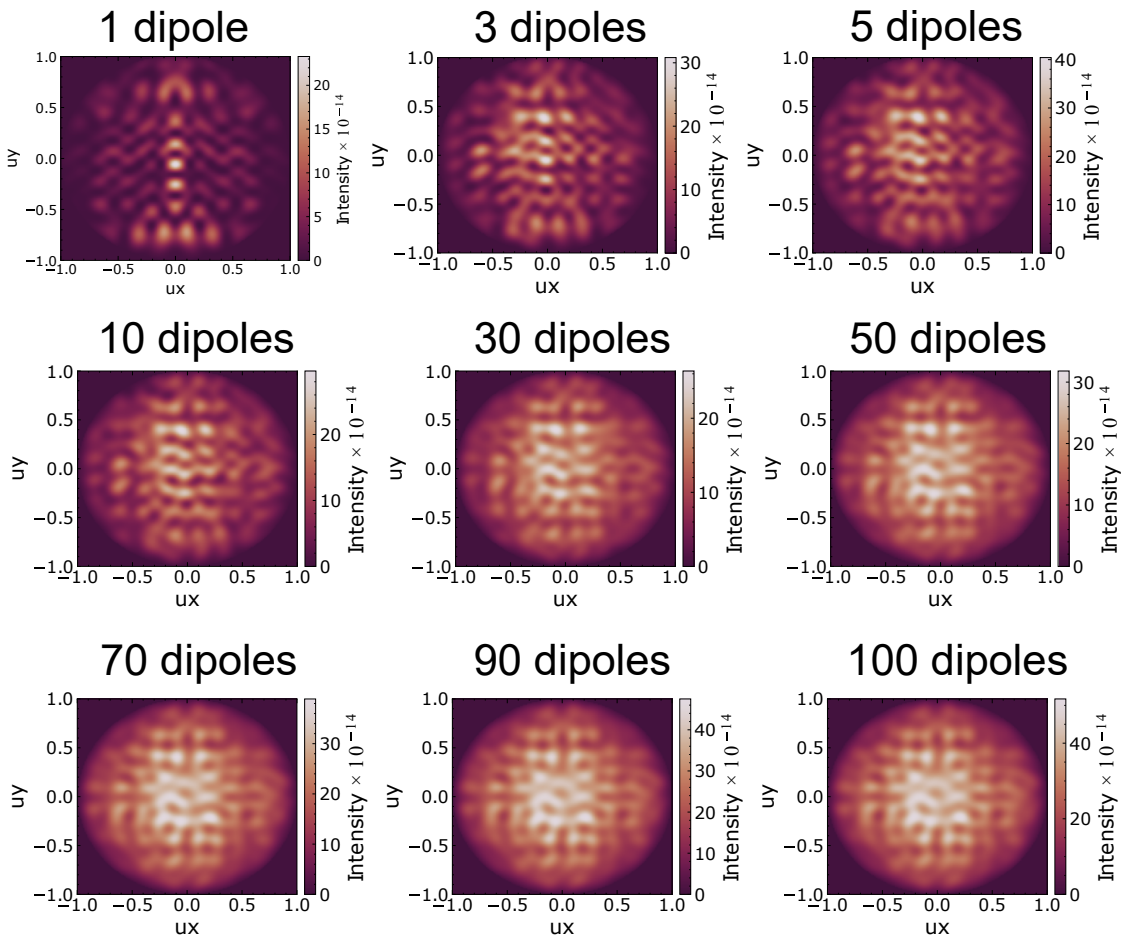

Figure 5.8: Convergence tests of the far-field intensity **number of dipoles** of a 2 µm cube. Mesh accuracy 3. 6 x 6 x 6 µm sized PML with 8 layers.

Appendix B

5.5 CL: Emission from individual particles

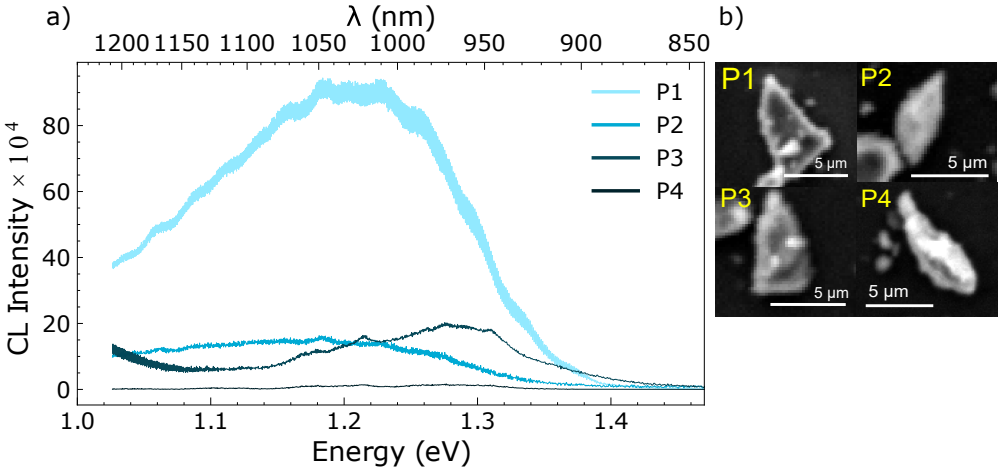

Figure 5.9: (a) Background subtracted CL spectra in the IR region from several particles marked in SEM micrographs in (b). The spectra are averaged spectra from the respective particle. All spectra and maps of the **1E14-300C** sample measured with 10 keV at 80 K.

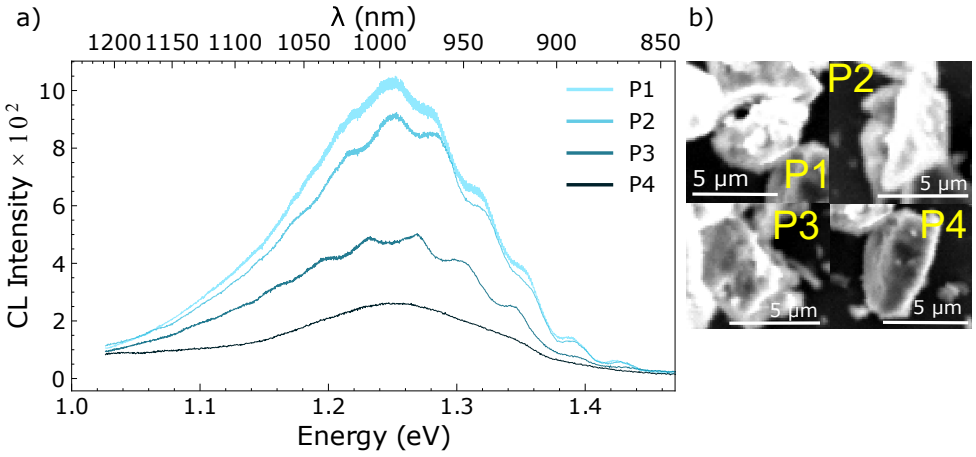

Figure 5.10: (a) Background subtracted CL spectra in the IR region from several particles marked in SEM micrographs in (b). The spectra are averaged spectra from the respective particle. All spectra and maps of the **1E14-1000C** sample measured with 10 keV at 80 K

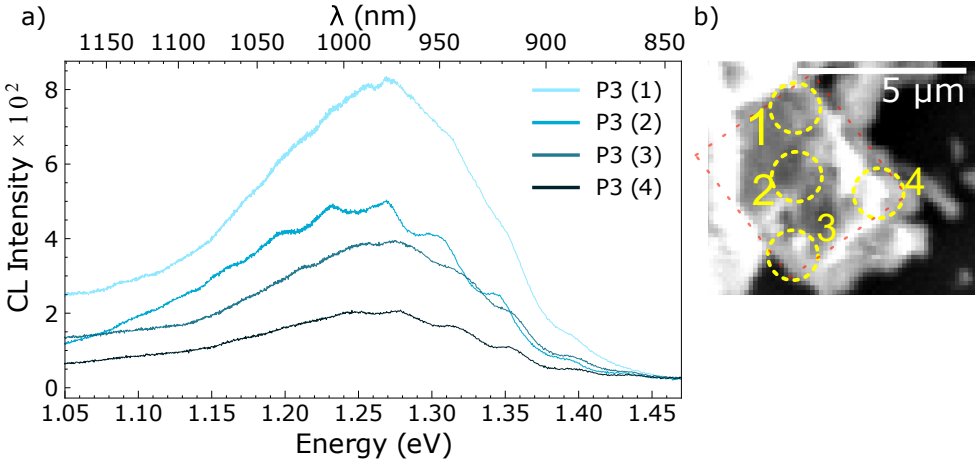

Figure 5.11: (a) Background subtracted CL spectra in the IR region from several particles marked in SEM micrographs in (b). The spectra are averaged spectra from the respective particle. All spectra and maps of the **1E14-1000C** sample measured with 10 keV at 80 K.

5.6 CL: Background Subtraction

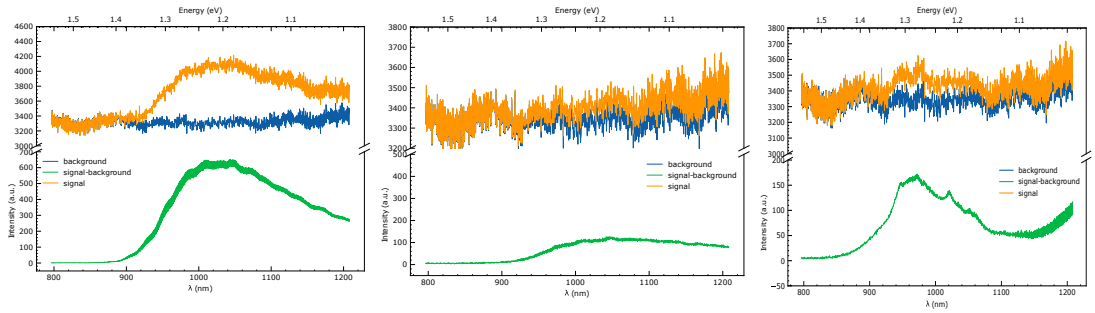

Figure 5.12: Example of bakcground subtracted (green) CL spectra. The orange and blue spectra are the signal and background signal, respectively. Note the wavelength on the bottom x-axis here.